Title

FLITECAM Development and Early Science on SOFIA and Investigating Ages of Late-Type Brown Dwarfs with Keck/NIRSPEC

Author

Logsdon, Sarah Elizabeth

Publication Date

2017

UNIVERSITY OF CALIFORNIA
Los Angeles

FLITECAM Development and Early Science on SOFIA and Investigating Ages of Late-Type Brown Dwarfs with Keck/NIRSPEC

A dissertation submitted in partial satisfaction
of the requirements for the degree
Doctor of Philosophy in Astronomy

by

Sarah Elizabeth Logsdon

2017

ABSTRACT OF THE DISSERTATION

FLITECAM Development and Early Science on SOFIA and Investigating Ages of Late-Type Brown Dwarfs with Keck/NIRSPEC

by

Sarah Elizabeth Logsdon
Doctor of Philosophy in Astronomy
University of California, Los Angeles, 2017
Professor Ian S. McLean, Chair

This dissertation combines the development of infrared instrumentation with the application of infrared imaging and spectroscopy to studies of the highest and lowest mass products of the star formation process. I supported the development and commissioning of FLITECAM, a ∼1-5 μm imager and spectrograph for SOFIA (Stratospheric Observatory for Infrared Astronomy), as the UCLA FLITECAM Instrument Scientist, and used FLITECAM to probe high-mass star formation. In parallel, I used the NIRSPEC spectrograph at the W.M. Keck Observatory to study the lowest mass products of star formation, brown dwarfs. Here, I present my FLITECAM development work and an overview of FLITECAM's in-flight performance in both imaging and spectroscopy modes. I also discuss early science with FLITECAM, including an imaging survey of the NGC 2024 and W3 star-forming regions using FLITECAM's Paschen-α (1.87 μm) and Polycyclic Aromatic Hydrocarbon (PAH; 3.3 μm) filters. Additionally, I present the results of a Keck/NIRSPEC spectroscopic follow-up survey of 13 late-type T dwarfs (T6-T9) with unusually red or blue *J*-*H* colors. Previous work suggests that *J*-*H* color outliers may represent the high-gravity, low-metallicity (old) and low-gravity, high-metallicity (young) extremes of the late-T dwarf population. I find that the T dwarf color outliers in this sample are more homogenous than expected, though three objects stand out as potentially old and a fourth object stands out as potentially young. To characterize the physical properties of the sample, I compare the target spectra to both spectral standards and publicly available atmospheric model grids.

The dissertation of Sarah Elizabeth Logsdon is approved.

Edward D. Young

Michael P. Fitzgerald

Eric E. Becklin

Ian S. McLean, Committee Chair

University of California, Los Angeles

2017

To my daddy, who inspires my dreams, and my mom, who supports each one

TABLE OF CONTENTS

LIST OF FIGURES

LIST OF TABLES

ACKNOWLEDGMENTS

Completing a PhD is not a solitary exercise. I am so thankful for the friends, family, colleagues, and mentors, who have helped me grow as a scientist and a human being both before and during my time in graduate school.

First, to my advisor, Ian McLean: From day one, you have challenged me to reach out of my comfort zone, and encouraged me to reach my own potential. Thank you for being a trusted mentor, colleague, and an incredible example of what it means to be an instrumentalist and a scientist. It has truly been a pleasure working with you and I look forward to our ongoing collaboration.

To my undergrad mentors– Adam Burgasser: You enabled me to attend my first conference, present my first poster, give my first research talk, and go on my first (snowed-out!) observing run. Working in the Cool Stars Lab prepared me for graduate school better than any of my undergraduate coursework possibly could. Thank you. Gillian Wilson and Alessandro Rettura: You generously responded to an unsolicited request from a student at a different university who wanted summer research experience. Not only did I walk away from my summer at UCR knowing how to use IRAF and what "high-redshift" meant, I also walked away knowing I wanted to continue pursuing the answers to astrophysical questions. Thank you.

To Eric Becklin: Always curious, enthusiastic, and supportive, with a keen scientific mind. It has been a pleasure learning from and working with you, and I look forward to continued collaboration. Thank you.

To Mike Fitzgerald and Ed Young: Thank you for rounding out my thesis committee, an important and appreciated role.

To the IR Lab Team: The IR Lab has been like a second home to me. It has been a privilege to work side-by-side with each one of you. You all mean more to me than you know and I hope we remain friends and colleagues for years to come. To Ian, James Larkin, and Mike– thank you for fostering an environment that allows graduate students to “learn by doing” surrounded by a team of technical experts. To the IR Lab staff– Thank you for your patience as I tried things I had never done before and for ultimately trusting me to lead as the FLITECAM Instrument Scientist. Thanks also for the many hours of fun, friendship, and laughter. A little extra thanks goes to Ken Magnone, who supported (almost) all of FLITECAM's needs with a smile and rarely hid when I entered the room, and to Chris Johnson, who really does perform computer miracles and who has graciously shared some of his FLITECAM photos for this manuscript. We have certainly had some wonderful adventures.

A special thanks to my collaborators on the SOFIA project, particularly the FLITECAM team (Maureen Savage, Ryan Hamilton, Bill Vacca, Sachin Shenoy, Jennifer Milburn), the HIPO team (especially Ted Dunham and Peter Collins), and all of the USRA and NASA support staff who made our SOFIA flights possible.

I have also received invaluable support from my academic siblings. To Erin Smith- From the day you pulled me out of the first-year bullpen to remount FLITECAM filters, you have inspired me. You remind me to believe in myself, and are always available with sound advice and encouragement. I am so grateful to have you as a role-model and a friend. To Greg Mace- Honest, patient, and kind. An inquisitive and thoughtful scientist and a generous mentor. Thank you for sharing your enthusiasm for brown dwarf science and for your unwavering support. To Emily Martin- My brown dwarf buddy! What can I say? It has been a privilege to share the grad school journey with you. Thank you for supporting me in the difficult moments and for sharing in the happy ones. Never forget that a) you are amazing and b) observing is always better with gummy bears and jelly beans.

The UCLA Astronomy grad student cohort is a special one. I am truly grateful for each Astro grad who I have shared the UCLA experience with, but there are a handful of grads that need special mention. To Laura Haney and Li-Wei Hung– thank you for keeping me sane, making me laugh, sharing your delicious recipes, and adventuring with me. I wouldn't have made it through grad school without you both. To Anna Boehle– we did it! I am so glad that we get to cross the PhD finish line together. Thank you for your friendship and for sharing a love of music (you too, Gunther Witzel!). To Kim Phifer– thank you for being a listening ear as we waded through tough waters together. It meant more than you know. To Breann Sitarski– The very first person I knew at UCLA! Thank you for your friendship and support. To Robin and Thomas Rehagen– thanks for sharing laughs, music, and an obsession with all things Harry Potter! To Jeff Chilcote, Ian Crossfield, Kathy Kornei, Kristin Kulas, and Betsy Mills, thank you for your support, advice, and friendship.

To the Beni/Hackwood family, thank you for adopting me as daughter #3 and showing me that a PhD was possible. To Sarah Chang (a.k.a. The Other Sarah), since middle school we have been each other's academic pacers and cheerleaders, pushing each other to pursue our dreams and supporting each other along the way. I am so, so proud of you! To Daniella Bardalez-Gagliuffi, thank you for being my "exit buddy" as we completed the last lap of grad school together. I am so excited to see where the next step in the journey takes us!

To my family: Words cannot express how important your support has been. Mom, you are my rock. Thank you for everything. Papa, thank you for your genuine interest in my science and for being the world's best handyman. To William, thank you for being you and for making me laugh. I hope I have convinced you that brown dwarfs are not mythical creatures. Thank you to "Team Sarah"– Aunt Polly, Chris, and Grandma– for cheering me on always. I wouldn't have made it to this point without each of you and I love you all.

The Introduction and Chapter 3 of this dissertation contain material from Logsdon et al., (2014) which is reproduced by permission of the SPIE. I would like to acknowledge my collaborators on this work: Ian McLean, Eric Becklin, Edward (Ted) Dunham, Ryan Hamilton, Christopher (Chris) Johnson, Jennifer Milburn, Maureen Savage, Sachindev Shenoy, Erin Smith, and William (Bill) Vacca.

Chapter 2 of this dissertation includes work completed in the UCLA IR Lab. I would like to acknowledge my colleagues on the IR Lab FLITECAM team: Ted Aliado, George Brims, Chris Johnson, Ken Magnone, and Eric Wang.

Unless otherwise noted, the photographs in Chapters 1-3 are from the private collections of Chris Johnson and myself. Chris Johnson's photos are reproduced by his permission.

Chapter 4 of this dissertation is a version of Logsdon et al., (2016) which is reproduced by permission of the SPIE. I would like to acknowledge my collaborators on this work: Ian McLean, Eric Becklin, Ryan Hamilton, William (Bill) Vacca, and Patrick Waddell.

Chapter 5 of this dissertation is a version of a paper to be submitted to the Astrophysical Journal. I would like to acknowledge my collaborators on this work: Gregory Mace, Ian McLean, and Emily Martin.

The FLITECAM science presented in this dissertation is based on observations made with the NASA/DLR Stratospheric Observatory for Infrared Astronomy (SOFIA). SOFIA is jointly operated by the Universities Space Research Association, Inc. (USRA), under NASA contract NAS2-97001, and the Deutsches SOFIA Institut (DSI) under DLR contract 50 OK 0901 to the University of Stuttgart. Financial support for this work was provided by NASA through award # 08500-05 issued by USRA.

This dissertation also includes data obtained at the W.M. Keck Observatories on Maunakea, Hawaii. I wish to recognize and acknowledge the very significant cultural role and reverence that the summit of Maunakea has always had within the indigenous Hawaiian community. I am most fortunate to have had the opportunity to conduct observations from this mountain.

This research has further benefited from (1) the Brown Dwarf Spectroscopic Survey (BDSS) Archive housed at bdssarchive.org, (2) the M, L, T, and Y dwarf compendium housed at DwarfArchives.org and curated by Chris Gelino, Davy Kirkpatrick, Mike Cushing, David Kinder, and Adam Burgasser, (3) the SpeX Prism Spectral Libraries, maintained by Adam Burgasser at http://pono.ucsd.edu/∼adam/browndwarfs/spexprism, (4) the NASA/ IPAC Infrared Science Archive, which is operated by the Jet Propulsion Laboratory, California Institute of Technology, under contract with the National Aeronautics and Space Administration, and (5) the tools developed and operated at CDS, Strasbourg, France (including the SIMBAD database and the Aladin sky atlas).

VITA

2011	B.S. Physics with a Specialization in Astrophysics Minor: Literatures in English University of California, San Diego
2013	M.S. Astronomy University of California, Los Angeles

PUBLICATIONS

S. E. Logsdon, G. N. Mace, I. S. McLean, E. C. Martin. *Probing Late-T dwarf J-H Color Outliers for Signs of Age*. To be submitted to ApJ.

D. Angerhausen, C. Dryer, B. Placek, Sz. Csizmadia, Ph. Eigmülcer, M. Godolt, D. Kitzmann, M. Mallonn, et al. including **S. E. Logsdon**. *Simultaneous multicolor optical and near-infrared transit photometry of GJ 1214b with SOFIA*. Submitted to A&A.

A. S. Bosh, M. J. Person, C. A. Zuluaga, A. A. Sickafoose, S. E. Levine, J. M. Pasachoff, et al. including **S. E. Logsdon**. *Haze in Pluto's atmosphere: Results from SOFIA and ground-based observations of the 2015 June 29 Pluto occultation.* Submitted to Icarus.

E. C. Martin, G. N. Mace, I. S. McLean, **S. E. Logsdon**, E. L. Rice, J. Davy Kirkpatrick, A. J. Burgasser, M. R. McGovern, L. Prato. *Surface Gravities for 228 M, L, and T Dwarfs in the NIRSPEC Brown Dwarf Spectroscopic Survey.* 2017. ApJ, 838, 73.

S. E. Logsdon, I. S. McLean, E. E. Becklin, R. T. Hamilton, W. D. Vacca, P. Waddell. *FLITECAM: delivery and performance on SOFIA*. 2016. Proc. SPIE, 9908, 99080B.

J. Davy Kirkpatrick, K. Kellogg, A. C. Schneider, et al. including **S. E. Logsdon**. *The AllWISE Motion Survey, Part 2.* 2016. ApJS, 224, 36.

A. J. Burgasser, **S. E. Logsdon**, J. Gagne, J. J. Bochanski, J. K. Faherty, A. A. West, E. E. Mamajek, S. J. Schmidt, K. L. Cruz. *The Brown Dwarf Kinematics Project (BDKP). IV. Radial Velocities of 85 Late-M and L dwarfs with MagE.* 2015. ApJS, 220, 18B.

D. Angerhausen, G. Mandushev, A. Mandell, E. Dunham, et al. including **S. Logsdon**. *First exoplanet transit observation with SOFIA: Confirmation of Rayleigh scattering in HD 189733 b with HIPO.* 2015. JATIS, 1, 034002.

W. D. Vacca, R. T. Hamilton, M. Savage, S. Shenoy, E. E. Becklin, I. S. McLean, **S. E. Logsdon**, G. H. Marion, et al.. *Observations of Type Ia Supernova 2014J with FLITECAM/SOFIA.* 2015. ApJ, 804, 66.

S. E. Logsdon, I. S. McLean, E. E. Becklin, E. W. Dunham, R. T. Hamilton, C. A. Johnson, J. W. Milburn, M. L. Savage, S. S. Shenoy, E. C. Smith, W. D. Vacca. *FLITECAM: early commissioning results.* 2014. Proc. SPIE, 9147, 91472Y.

E. C. Smith, J. W. Miles, L. A. Helton, R. Sankrit, et al. including **S. Logsdon**. *SOFIA science instruments: commissioning, upgrades, and future opportunities.* 2014. Proc. SPIE, 9147, 914706.

J. Davy Kirkpatrick, A. Schneider, S. Fajardo-Acosta, C. R. Gelino, G. N. Mace, et al. including **S. E. Logsdon**. *The AllWISE Motion Survey and the Quest for Cold Subdwarfs.* 2014. ApJ, 783, 122.

G. N. Mace, J. D. Kirkpatrick, M. C. Cushing, C. R. Gelino, I. S. McLean, **S. E. Logsdon**, E. L. Wright, M. F. Skrutskie, C. A. Beichmann, P. R. Eisenhardt, K. R. Kulas. *The Exemplar T8 Subdwarf Companion to Wolf 1130.* 2013. ApJ, 777, 36.

A. J. Burgasser, B. N. Sitarski, C. R. Gelino, **S. E. Logsdon**, M. D. Perrin. *The Hyperactive L Dwarf 2MASS J13153094-2649513: Continued Emission and a Brown Dwarf Companion.* 2011, ApJ, 739, 49.

CHAPTER 1

Introduction

Each new generation of telescopes, and the advanced cameras that accompany those telescopes, have enabled scientists to explore novel astronomical parameter space: reaching fainter astronomical signals, achieving finer spatial or spectral resolutions, and/or investigating new wavelength regimes. Historically, visible light (optical) astronomy saw the earliest growth, but modern astronomical studies are not limited to the light we can see. Using both ground-based and space-based platforms, we are now able to observe across the electromagnetic spectrum from high-energy gamma ray astronomy to long-wavelength radio astronomy. The last thirty years have seen tremendous advancement in the development and use of infrared technology in astronomical research. This dissertation includes both the development of infrared instrumentation and the application of infrared instrumentation to probe astrophysical questions. Specifically, I supported the later stages of development and the commissioning of FLITECAM, a $\sim$1-5 μm imager and grism spectrograph, on the Stratospheric Observatory for Infrared Astronomy (SOFIA) and used FLITECAM to probe the distribution of gas and dust in two nearby star-forming regions, NGC 2024 and W3. In parallel, I used the NIRSPEC spectrograph at the W. M. Keck Observatory to study and characterize the atmospheres of a sample of the coldest brown dwarfs to look for spectroscopic signatures of age.

1.1 Observing in the Infrared: Motivation, Challenges, and Platforms

Since the introduction of the first infrared array detectors in the mid-1980s, the development and use of dedicated infrared instruments and observatories has boomed. Infrared arrays are the equivalent of digital cameras for optical wavelengths. Infrared arrays have grown from a few thousand pixels in the mid-1980s, to several million pixels today. This critical advancement in technology allows modern astronomers to probe regions of the universe, both large and small, that are essentially invisible to the human eye and to traditional optical instruments. Studying the universe in the infrared is an essential component in the quest to understand the cosmos. Infrared observations allow us to peer back in time to study high-redshift galaxies whose rest-frame optical light has shifted into the infrared on the way to our cameras. Because of its longer wavelength, infrared light can also penetrate dense regions of gas and dust that scatter and absorb shorter-wavelength optical light, revealing stellar nurseries, studies of which are critical for our understanding of star formation and its early evolution. Furthermore, infrared observations probe colder temperatures than optical observations, revealing objects such as late-type brown dwarfs and extrasolar planets, which emit minimal light in the optical, but are observable in the infrared.

Observing in the infrared is not without its obstacles, however, and these challenges must be carefully considered when designing infrared observatories and instrumentation. Everything warm, from the telescope to the instrument itself, can be detectable to the sensitive infrared array at the heart of an infrared instrument. If these thermal 'background' signals are not removed, it can be difficult, or in some cases, impossible to detect the relatively faint signal from an astronomical object of interest. To address this problem, infrared cameras are typically maintained at very cold temperatures (< 100 K) using liquid cryogens or closed-cycle refrigerator technology. Whenever possible, infrared telescopes are also temperature controlled. In addition to thermal backgrounds from warm telescopes and instruments, ground based infrared observations are hampered by absorption from molecules such as water and carbon dioxide in the Earth's atmosphere. These molecules absorb the light from a large fraction of the infrared spectrum, making extended wavelength ranges unobservable from the ground. This absorption of astronomical light in Earth's atmosphere is known as telluric absorption. The solution to combating telluric absorption is to get above it. The best ground-based observing sites are located in dry climates and at high altitudes, such as the summit of Maunakea in Hawaii (e.g. Keck Observatory elevation: ∼13,500 ft/4.1 km) and the Atacama Desert region of Chile (e.g. Las Campanas Observatory elevation: ∼7,800 ft/2.4 km). Space-based observatories eliminate any telluric absorption concerns. The first space telescope to conduct an all-sky survey in the infrared was the Infrared Astronomical Satellite (IRAS; Neugebauer et al. 1984). Since the pioneering results from IRAS, infrared observatories such as the Spitzer Space Telescope (Spitzer; Werner et al. 2004), the Wide-field Infrared Survey Explorer (WISE; Wright et al. 2010), and the Herschel Space Observatory (Herschel; Pilbratt et al. 2010) have been highly successful in advancing our knowledge of the infrared universe.

If the solution to avoiding telluric absorption is to go to space, you may ask: Why aren't all infrared observatories in space? Determining whether to build a space-based or ground-based observatory is a study in trade-offs. While infrared space missions eliminate atmospheric concerns, they have their own unique challenges, beyond the obvious challenge of cost. Unlike ground-based observatories, which have the flexibility to change instruments to suit different science cases and to replace obsolete instruments as technology improves, the instruments accompanying a space based observatory are typically fixed. With the exception of the Hubble Space Telescope, which is in a low-Earth orbit and could be reached by the Space Shuttle fleet before they were retired, space observatories are also unserviceable after launch. While space-based observatories are subject to much less thermal background than ground based observatories (see e.g. Figure 1 in Beckwith 2013), observatories in space still experience a non-zero heat load. Infrared observatories typically launch with liquid cryogens aboard to cool the observatory. These cryogens eventually boil-off and thus limit the usable lifetime of any long-wavelength ($\geq 5\ \mu$m) sensitive instruments or instrument modes on the observatory. Therefore, while infrared space observatories certainly have tremendous value, it is not feasible to put all observatories in space.

An alternative to ground- and space- based observing platforms is the airborne observatory. In practice, airborne observatories have taken three forms: sounding rockets, balloons, and airplanes. All three airborne platforms benefit observationally from the reduced water-vapor overburden at high-altitudes. Both balloon and sounding rocket observations have the advantage that they are typically made at higher altitudes than a traditional airplane can fly. Balloons can fly up to ∼31,000 ft/40 km and sounding rockets typically observe anywhere from ∼160,000 ft/50 km to ∼4,900,000 ft/1500 km (e.g. Eberspeaker & Pierce 2011). However, an airplane-based platform is more maneuverable than a balloon or a rocket, carries fewer weight restrictions, and is easier to recover and reuse. An airplane observatory also shares many of the advantages of a ground-based platform – serviceability, instrument flexibility, and observatory longevity. In the next section I discuss SOFIA, currently the only active astronomical observatory in an airplane.

1.2 SOFIA: The Flying Observatory

The Stratospheric Observatory for Infrared Astronomy (SOFIA) is an airborne observatory featuring a 2.5 meter bent Cassegrain telescope installed in a Boeing 747-SP aircraft[1]. SOFIA is a joint project between NASA and the German Aerospace Center (DLR). It observes from 39,000-45,000 ft (11.9-13.7 km), placing the telescope above over 99% of the water vapor in the Earth's atmosphere. By flying above most of that water vapor, SOFIA opens up much of the infrared spectrum to observation, particularly beyond 10 μm (see e.g. Figure 1 in Becklin et al. 2006).

The telescope itself is mounted at the rear of the aircraft and is separated from a temperature and pressure controlled cabin by a pressure bulkhead. A custom door in the fuselage opens to expose the telescope to the stratosphere for observing (see Figure 1.1). The SOFIA telescope is mounted on a large, spherical bearing that floats freely on a thin layer of oil to

---

[1] SOFIA is the successor to the Kuiper Airborne Observatory (KAO), a 0.9 meter telescope installed in a Lockheed C-141 Starlifter, that flew from 1974-1995. A comprehensive review of the KAO was written by Edwin F. Erickson and Allan W. Meyer as part of NASA's History Series publications (NASA SP-2013-216025).

Figure 1.1 A series of photos taken by Chris Johnson showing the SOFIA door opening for ground operations (line ops).

keep the telescope stable, even during turbulence. This bearing mount acts like an altitude-azimuth mount with a 6° azimuthal range and an unvignetted altitude range of 23°-58° (Young et al., 2012a). Line-of-sight rewinds are required to keep each target field in the observable field of the telescope. Instruments are mounted to SOFIA on the cabin side of the pressure bulkhead with the installed instrument and its electronics rack acting as counterbalances for the telescope. A tube passes through the bearing from the telescope to the science instrument, reflecting light from SOFIA's tertiary mirror to a focus (the Nasmyth focus) at the science instrument (see Figure 3 in Young et al. 2012b).

As of 2017, SOFIA's instrument suite covers 0.3-240 μm with eight instruments: HIPO, FPI+, FLITECAM, FORCAST, EXES, FIFI-LS, HAWC+, and GREAT. These instruments provide a combination of imaging, spectroscopic, and polarimetric capabilities, which are detailed on the SOFIA website[2].

---

[2] http://www.sofia.usra.edu

1.3 FLITECAM Instrument Development, Commissioning, and Delivery

FLITECAM (First Light Infrared Test Experiment CAMera; McLean et al. 2006) is a near-infrared (∼1 to 5.5 μm) camera and spectrograph developed in the Infrared Laboratory (IR Lab) at UCLA for use on SOFIA (see Figures 1.2 and 1.3). FLITECAM captures the entire circular 8′ diameter field of view (FOV) of the SOFIA telescope onto a 1024 x 1024 pixel InSb ALADDIN III detector with a plate scale of 0.47″/pixel. Image quality is best within the central 5.6′ diameter field. The two primary observing modes are imaging and grism spectroscopy. FLITECAM is cryogenically cooled by both a liquid nitrogen dewar (LN2; T∼77K) and a liquid helium dewar (LHe; T ∼4K). The optical system is cooled by the LN2 dewar and operates at ∼85K. The detector is maintained at 30K by a Lakeshore temperature controller that regulates a thermal bridge between the LN2 and LHe dewars.

Figure 1.2 The FLITECAM instrument system in the lab. From left to right: The FLITECAM cryostat on its handling cart, the Counterweight Rack (CWR), the Principal Investigator Rack (PI rack).

The FLITECAM instrument system is comprised of three components (see Figure 1.2): the FLITECAM cryostat or the science instrument (SI), the Counterweight Rack (CWR), and the Principal Investigator Rack (PI Rack). The CWR houses FLITECAM's detector and motor power supplies, motor controllers, and Lakeshore temperature and helium level monitors. As its name suggests, the CWR also serves as a counterweight for the SOFIA telescope and is mounted alongside the SI during flight (see Figure 1.3). Communication to the CWR is achieved through a set of optical fibers connected to a serial multiplexer in the rack. The PI rack houses the instrument control computers (named FARSCAPE, STARGATE, and MKIR) and is where the instrument operator(s) sits during flight. FARSCAPE, a Dell PowerEdge 2600, performs hardware connections to the CWR through serial ports and tracks and stores instrument housekeeping such as helium percentage and instrument temperatures. STARGATE, an Apple Mac Mini, is FLITECAM's instrument control and integration software (FICIS) computer. All standard FLITECAM observations are executed from STARGATE. MKIR (Mauna Kea InfraRed Labs computer) is the interface to the electronics readout for the detector. Its front end is connected to STARGATE through a File Transfer Protocol (FTP) socket. In typical operation, the only direct interface an instrument operator has with MKIR is for array initialization and detector performance verification.

FLITECAM was originally designed as an observatory test camera for SOFIA. In order to characterize the instrument before delivery to SOFIA, FLITECAM was first commissioned on the 3-meter Shane Telescope at Lick Observatory. Eight observing runs at Lick Observatory from 2002-2007 not only helped characterize FLITECAM's ∼1-3.5 μm performance, but also produced science results that lead to three refereed publications (Mainzer and McLean 2003, Mainzer et al. 2004, Smith and McLean 2008) and two PhD theses (Mainzer 2003; Smith 2008). FLITECAM's first flights on SOFIA were executed in Fall 2011. These first flights were SOFIA Characterization and Integration flights (SCAI) designed to exercise the telescope systems and were not instrument commissioning flights. I joined the UCLA IR Lab FLITECAM team just prior to my second year of graduate school in June 2012 and served as the UCLA Instrument Scientist from 2012 until FLITECAM was officially delivered to SOFIA in August 2015. As the UCLA Instrument Scientist, I conducted research and development work in the UCLA IR Lab, and supported the full instrument commissioning and early science on SOFIA, including FLITECAM's first international deployment to New Zealand. After FLITECAM's formal delivery, I supported FLITECAM flights in September/October 2015 and October 2016.

FLITECAM can be mounted to the SOFIA telescope in two configurations (see Figure 1.3): 1) the "solo" mode, in which FLITECAM is mounted to SOFIA by itself and 2) the "FLIPO" mode, in which FLITECAM is co-mounted with the optical instrument HIPO (High-speed Imaging Photometer for Occultations; PI Edward Dunham, Lowell Observatory). FLITECAM in the FLIPO mode was commissioned in 2014, and the solo mode was commissioned in 2015-2016. In September 2014, FLITECAM was accepted by NASA as a facility-class science instrument (FSI) for SOFIA. As a FSI, FLITECAM is operated and maintained by the SOFIA Observatory. However, HIPO is classified as a special purpose, principal investigator-class instrument (known as a SSI), thus the FLIPO configuration is also considered a SSI. For more information on the different classes of SOFIA instrument, visit the instrument page of the SOFIA website (www.sofia.usra.edu/science/instruments).

Because FLITECAM observes in the stratosphere, it is sensitive in several interesting regions of the near-infrared that are difficult or impossible to observe from the ground. Using a combination of FLITECAM's specialized narrow band imaging filters and grism spectroscopy, my FLITECAM science goals take advantage of FLITECAM's wide field of view and focus on observations of high-mass star forming regions. The early results of these observations are promising and, with newly acquired science funding from SOFIA, a full scientific analysis is underway and will continue into the summer.

1.4 Probing High Mass Star Formation with SOFIA/FLITECAM

Stars form via gravitational collapse within dense, dusty clouds of molecular hydrogen. In the most massive regions of star formation the newly-formed hot, massive stars ionize the nearby hydrogen, but gas and dust in their natal clouds can render these newborn stars invisible at optical wavelengths. Fortunately, longer wavelength infrared light can penetrate

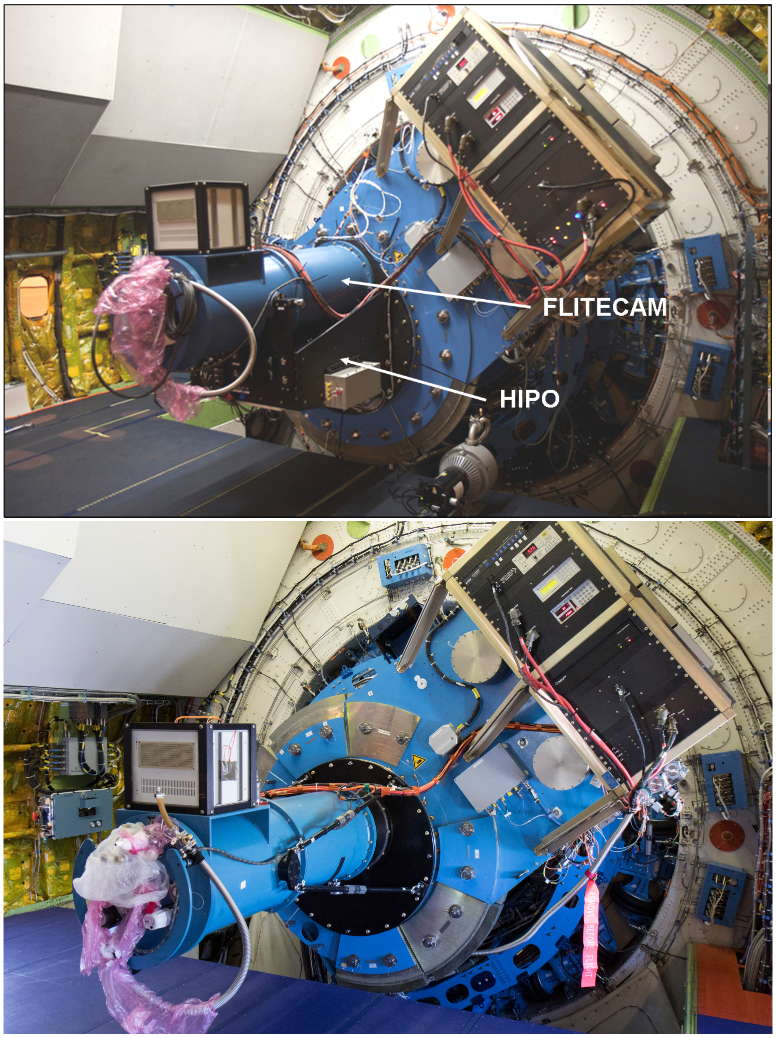

Figure 1.3 Top: FLITECAM (blue cylinder) co-mounted on the SOFIA telescope with HIPO (black instrument directly beneath FLITECAM) in the FLIPO configuration. Both instruments are mounted at the end of SOFIA's Nasmyth tube. A dichroic beamsplitter and a fold mirror (not pictured) reflect the infrared light from the telescope to FLITECAM. Bottom: FLITECAM installed on SOFIA in the solo configuration. The suspended black rectangle in the upper right of each photo is the FLITECAM electronics housing (i.e. CWR).

these regions, revealing the hidden stellar nurseries. If we assume Case B[3] line intensities (Baker & Menzel, 1938), the Paschen-α line at 1.875 μm is over twelve times stronger than the

---

[3] Case B assumes that a star-forming region is optically thick to high energy photons such that Lyman transition (n=1) photons are reabsorbed by the gas in the nebula and do not significantly contribute to the measured ionization fraction.

Brackett-γ line at 2.166 μm (Hummer & Storey, 1987). This makes Paschen-α the ideal near-infrared line for tracing ionized hydrogen in star-forming regions, even though the difference in reddening between Paschen-α and Brackett-γ favors Brackett-γ[4]. However, Paschen-α is virtually unobservable from the ground due to water vapor in the Earth's atmosphere. Fortunately, Paschen-α is easily attainable from the stratosphere with FLITECAM on SOFIA, providing a unique and powerful opportunity to observe this critically important diagnostic of dusty star-forming regions. The only other way to gain access to the Paschen-α region is with infrared instruments in space. On the Hubble Space Telescope, NICMOS provided a survey of the galactic center region in Paschen-α using narrow-band filters, but this instrument is no longer operational (Wang et al., 2010). Spitzer did not provide narrow-band images or spectroscopy at such short wavelengths. Fortunately, FLITECAM is equipped with two narrow-band filters centered on Paschen-α at 1.875 μm and the nearby continuum at 1.90 μm. These filters are only 1% wide (R$\sim$100), making them ideal for mapping the hydrogen emission strength relative to the continuum (see Figure 3.1).

Another tracer of star formation is the dust that makes star formation invisible in the optical. The dust re-emits the absorbed UV-optical star light at infrared wavelengths. One component of this dust emission is from tiny grains of polycyclic hydrocarbons (PAHs) at 3.3 μm. FLITECAM has a narrow filter (4-5 % wide) centered at 3.3 μm designed specifically to measure the strength of the broad emission from polycyclic aromatic hydrocarbons (PAHs) at 3.3 μm. The FLITECAM filter wheel also includes a useful continuum filter of the same width at 3.08 μm. Since this spectral region is also contaminated by water vapor in the atmosphere, SOFIA/FLITECAM enables much better measurements of PAH emission at 3.3 μm than are possible from the ground. Most importantly, the unique combination of Paschen-α and 3.3 μm PAH filters in FLITECAM allows heavily reddened star-forming

---

[4] For example, Haisch et al. (2000) find that the average extinction to the background stars in the Orion Flame Nebula (NGC 2024) is Av = 10.5 mag. The ratio of extinction from V band (0.55 micron) to K band (2.2 micron) is $A_K/A_V = 0.1$ (e.g. He et al. 1995). Therefore, for NGC 2024, $A_K = 1.05$ mag. In the near-infrared, $A_\lambda \propto \lambda^{-\alpha}$ where $\alpha \sim 1.7$ (see Draine 2003 and the references therein). This implies that $A_{Pa\alpha}/A_{Br\gamma} = 1.28$. Setting $A_{Br\gamma}=A_K$, implies $A_{Pa\alpha} = 1.48$, and $A_{Pa\alpha}$-$A_{Br\gamma}$ $\sim$0.4 mag. In other words, Paschen-α sees 0.4 magnitudes of extinction towards NGC 2024 when compared to Brackett-γ. However, this small loss is far outweighed by the fact that Paschen-α is 12x stronger ($\sim$2.7 mag) than Brackett-γ.

regions to be mapped for the relative distribution of ionized gas and small heated grains, which in turn gives insight into the evolution of the star-forming region. Using these two filters and their adjacent continuum filters, I have obtained observations of the Orion Flame Nebula (NGC 2024) and the W3 star-forming region.

1.5 Investigating the Atmospheres of the Coldest Brown Dwarfs with Keck/NIRSPEC

The newborn stars detected by FLITECAM in NGC 2024 and W3 are typically more massive than the Sun, but the star formation process produces objects that span an incredibly large range of masses. First predicted to exist in 1963 (Kumar 1963, Hayashi and Nakano 1963), brown dwarfs are objects that are not massive enough to ignite hydrogen fusion in their cores ($\lesssim$75 M_{Jup}), and are thus fundamentally not stars. Though brown dwarfs cannot be classified as stars, theory suggests that most, if not all, brown dwarfs form as stars do, through the gravitational collapse of molecular clouds. The theory that brown dwarfs predominantly form like stars automatically implies that these objects are distinct from giant planets, which predominantly form in disks around young stars (see e.g. Chabrier et al. 2014). Therefore brown dwarfs occupy a unique parameter space between stars and planets, sharing physical properties with both. The first methane-bearing brown dwarf was discovered in 1995 (GJ 229B; Nakajima et al. 1995), over thirty years after the original theory papers predicted their existence. Since the mid-1990's, the number of known brown dwarfs, classified into "spectral types" (M, L, T, or Y) by predominantly temperature-driven changes in their spectral morphology, has grown tremendously. Warmer M and L dwarfs were identified in large numbers in the early 2000s, mostly by surveys such as the Sloan Digital Sky Survey (SDSS; York et al. 2000) and the Two-Micron All Sky Survey (2MASS; Skrutskie et al. 2006). With temperatures $\leq$ 1400 K, T dwarfs, particularly late-type T dwarfs, were more elusive (e.g. Kirkpatrick 2005). Dwarfs with spectral types greater than $\sim$T5 have only been discovered in large numbers with a second generation of infrared surveys, including the Wide-Field Infrared Survey Explorer (WISE; Wright et al. 2010) and the UKIRT Infrared

Deep Sky Survey (UKIDSS; Lawrence et al. 2007). With temperatures as cool and colder than room temperature, the Y dwarf class, though predicted to exist for many years, was only discovered recently by WISE (Cushing et al. 2011; Kirkpatrick et al. 2011, 2012).

Late-type T and early Y dwarfs play a powerful role in answering several fundamental astrophysical questions. Field T and Y dwarfs represent the coldest and therefore either lowest mass or oldest products of star formation, making them a great asset to evolutionary models, which are degenerate at the lowest masses (Kirkpatrick et al., 2012). Because they are so faint, the discovered objects are necessarily nearby. A volume-limited sample of these brown dwarfs provides a powerful probe of the substellar mass function in the Solar Neighborhood. With temperatures similar to giant planets, T and Y dwarfs also serve as valuable test beds for atmospheric models as we begin to probe the atmospheres of the giant exoplanet population.

This dissertation uses medium-resolution Keck/NIRSPEC[5] spectroscopy to characterize late-T dwarfs with unusual $J-H$ colors. Installed on the 10 m Keck telescope, NIRSPEC is apt for spectroscopic studies of late-type T dwarfs, whose J-band magnitudes are typically > 15 (see e.g. the brown dwarf compendium at DwarfArchives.org). Such faint observations would be incredibly difficult to observe with FLITECAM on a 2.5 m telescope like SOFIA.

With my T dwarf observations from Keck/NIRSPEC, I tested the hypothesis set forth in Mace et al. 2013b that T dwarfs with unusual $J-H$ colors may be extremely young or old compared to the typical field population. To do so, I looked for spectroscopic tracers of age such as non-solar metallicity or extreme gravity. Other factors such as clouds and/or non-equilibrium processes in their atmospheres complicate the analysis of their spectra. Nevertheless, these outliers are an interesting probe of the physical processes occurring in the late-type brown dwarf population and provide a valuable test of the current atmospheric models in preparation for using such models on brown dwarf and exoplanet atmospheres in the era of the James Webb Space Telescope.

---

[5] Like FLITECAM, NIRSPEC was also developed in the UCLA Infrared Lab. It is a 0.95-5.5 μm spectrometer. In non-echelle mode, NIRSPEC achieves medium-resoultion ($\lambda/\Delta\lambda \sim$2000) spectroscopy. In echelle mode, $\lambda/\Delta\lambda \sim$25000. See McLean et al. (1998) for details.

This project is part of my work as a member of the NIRSPEC Brown Dwarf Spectroscopic Survey (BDSS) team (PI: Ian McLean, Co-I: J. Davy Kirkpatrick). The BDSS is a long-term science program designed to characterize the low-mass star and brown dwarf population using both NIRSPEC's medium and high-resolution modes. Since the first BDSS observations in 1999, the team has included both graduate students and postdoctoral scholars, contributing data to five PhD dissertations (McGovern 2005; Rice 2009; Mace 2014; this work; Martin *expected 2018*). In addition to my own research, I have collaborated with several other BDSS team members observing and reducing NIRSPEC spectroscopic follow-up data of subdwarf candidates in support of the AllWISE Motion Survey (Kirkpatrick et al., 2014, 2016), of L and T dwarfs in the Brown Dwarf Spectroscopic Survey (Martin et al., 2017), and of unusually red and blue L dwarfs (Rice et al., in prep; Alam et al., in prep). I also observed and reduced Keck/MOSFIRE imaging data in support of Mace et al. (2013b).

Chapter 2 of this work describes my FLITECAM research and development work in the UCLA Infrared Lab. Chapters 3 and 4 describe FLITECAM commissioning on SOFIA in the FLIPO and solo configurations as well as FLITECAM science. Chapter 5 describes my T dwarf studies with NIRSPEC.

CHAPTER 2

FLITECAM in the UCLA Infrared Laboratory

I joined the UCLA Infrared Laboratory (IR Lab) in June 2012. At the time, FLITECAM was gearing up for commissioning on SOFIA, but two light leaks in the instrument needed attention. My initial project was to find and eliminate the source(s) of the light leaks. As I worked with the IR Lab team to address the light leaks, my role on the FLITECAM team expanded beyond the original scope of my project. By the time we had eliminated the FLITECAM light leaks in August 2013, my instrumentation work included support for the broader FLITECAM team goals: commissioning preparation, commissioning execution, and post-commissioning acceptance and science. In other words, I assumed the role of UCLA Instrument Scientist for FLITECAM. I maintained that role until FLITECAM was formally delivered to SOFIA in the summer of 2015. This chapter summarizes my FLITECAM research and development work in the UCLA IR Lab, including FLITECAM commissioning preparation and post-commissioning acceptance work. FLITECAM commissioning on SOFIA in the 'FLIPO' configuration and FLIPO's first international deployment to observe a Pluto Occultation in summer 2015 are described in chapter 3. FLITECAM commissioning in the 'solo' configuration is described in Chapter 4.

2.1 Light Leak Investigation and Solution

An initial discussion of the two FLITECAM light leaks including their discovery, the elimination of the first light leaks, and several methodical tests to diagnose the second light leak can be found in my Master's thesis "Medium and Narrowband Filter Characterization and Their Application to Faint Brown Dwarf Detection." Here I provide a summary of that work

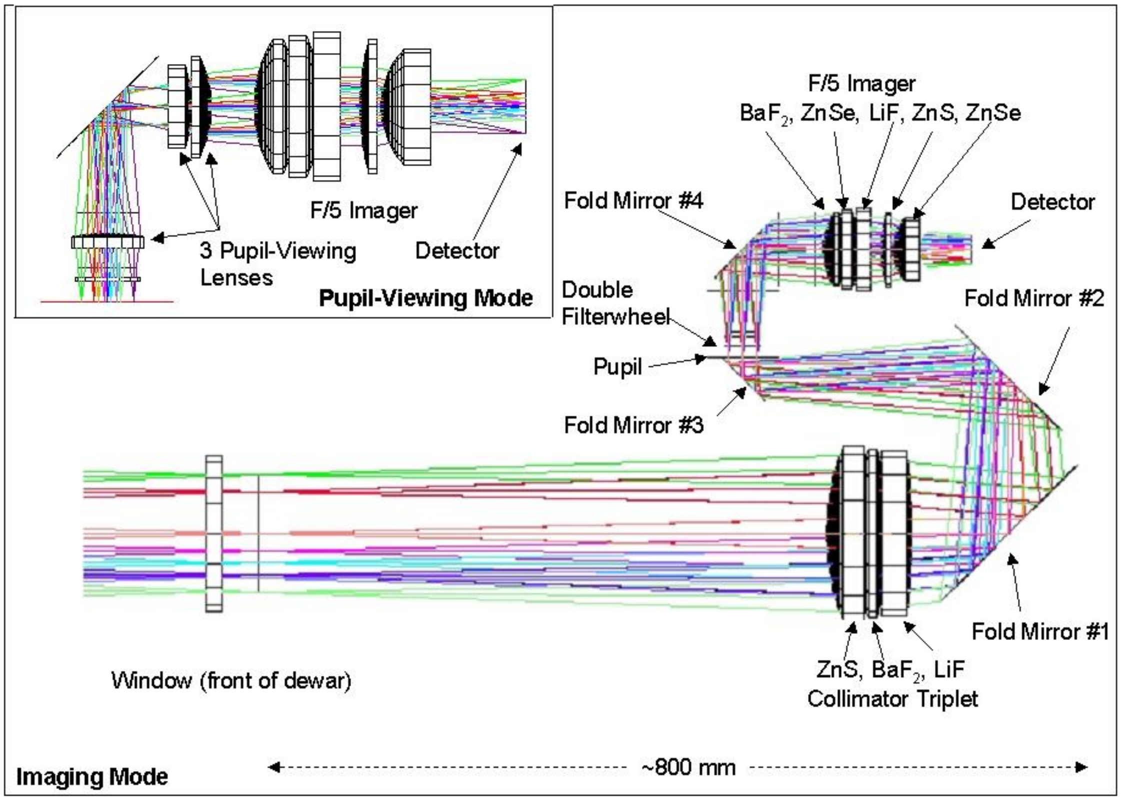

Figure 2.1 A ray trace diagram of the FLITECAM optical path from Mainzer et al. (2003). Inset: The pupil viewing (PV) mode in its original three lens configuration. In 2012, the first lens was removed from the instrument. The removed lens acted as a simple magnifier and its removal did not impact the functionality of the PV mode.

and then describe the successful elimination of the second light leak.

2.1.1 Instrument Design Background

FLITECAM's basic light path is as follows: Light from the 2.5-m SOFIA telescope enters FLITECAM through a calcium fluoride (CaF2) entrance window and comes to a focus. The diverging beam is then collimated by a triplet lens system (ZnS, BaF2, LiF), and reaches FLITECAM's dual filter wheel module after reflecting off of a series of three fold mirrors and passing through a pupil. A fourth fold mirror at the exit of the filter wheel box reflects light through FLITECAM's five lens (BaF2, ZnSe, LiF, ZnS, ZnSe), f/5 camera located in front of the InSb Aladdin III detector. There are also three additional lenses that can be moved in and out of the beam to enable a pupil-viewing mode (PV mode, described below). The optical path is illustrated in Figure 2.1.

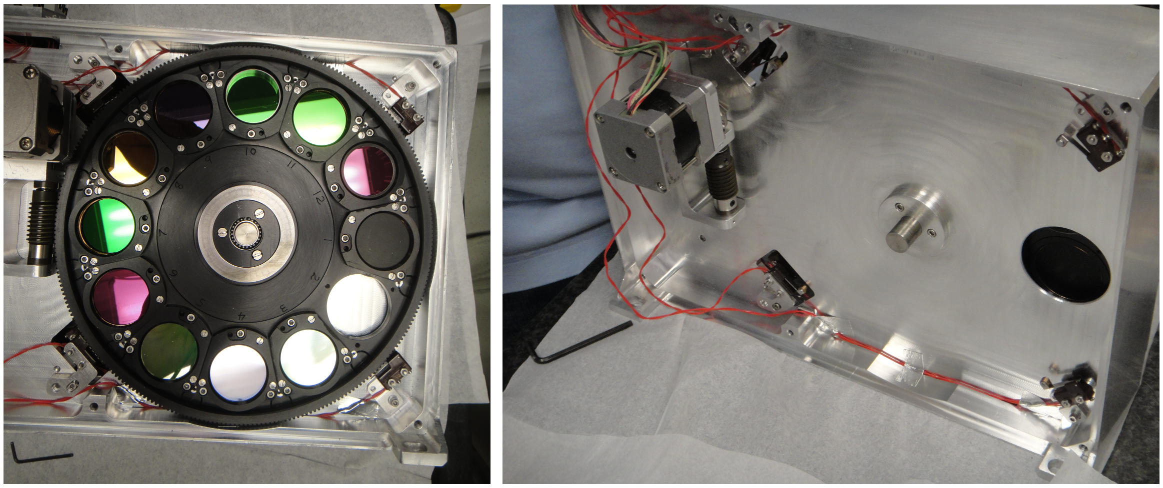

Figure 2.2 Two views of FLITECAM's dual filter wheel module. Both images are looking at filter wheel 1 (FW1) with the filter wheel box entrance lid removed. Left: FW1 enclosure with the filter wheel installed. This wheel has eleven identically sized filter positions featuring broad band imaging filters and order sorting filters. Right: FW1 enclosure with the filter wheel removed. Notice the circular aperture that allows light to pass from FW1 to FW2.

FLITECAM's dual filter wheel module was milled from a single block of aluminum. Each filter wheel enclosure was milled from the outside of the block inward such that each filter wheel is separated from the other by a central wall of un-anodized aluminum (see Figure 2.2). A circular through hole in the center wall allows light to pass from filter wheel 1 (FW1) to filter wheel 2 (FW2). FLITECAM's two filter wheels have a total of twenty-three filter positions (see Table 2.1.1 for current filter position information). Twelve filter positions are designed to accommodate a suite of narrow and broad band imaging filters. Three of the positions in the second wheel are square apertures, specially sized to accommodate three direct-ruled grisms of KRS-5 (Thallium Bromoiodide). These grisms, when paired with a set of four customized order sorting filters in the first wheel, give FLITECAM spectroscopic coverage across most of the 1-5.5 μm wavelength region with $R=\lambda/\Delta\lambda \sim 1300$ for a $\sim 2''$ slit (which was designed to match the expected seeing for SOFIA). A $\sim 1''$ slit is also available

Table 2.1. FLITECAM Filter Positions as of July 2014

Position	Filter Wheel 1 (FW1)	Filter Wheel 2 (FW2)
1	blank [a]	blank [b]
2	open	open
3	*J*	Paschen α
4	*H*	KRS-5 grism ‘A’
5	*K*	Paschen α Continuum
6	*L*	3.6 μm nbL
7	*L’*	KRS-5 grism ‘B’
8	*M*	3.08 μm Ice
9	H_{wide}	3.3 μm PAH
10	K_{wide}	KRS-5 grism ‘C’
11	K_{long}	4.5 μm nbM
12	L&M	N/A

[a] In this work, the term ‘blank’ implies an opaque disk mounted in a standard FLITECAM filter wheel mount.

[b] Prior to October 2012 FW2, Position 1 contained a singlet lens for FLITECAM’s pupil viewing mode.

with R∼1800. A fourth oversized filter position is located in the second wheel and was designed to accommodate a singlet lens that was part of the original design of FLITECAM's PV mode. The other two lenses that comprise the pupil-viewing mode are attached to a slide mechanism that can be moved in and out of the beam directly in front of the f/5 camera. The PV mode allows for observation of the primary mirror itself and is part of the observatory test camera aspect of FLITECAM's design. The original goal of the PV mode was to characterize the SOFIA telescope's primary mirror emissivity. The reader is referred to Smith (2008) and Smith & McLean (2008) for a more detailed description of the design of the PV mode.

2.1.2 Two Light Leaks Discovered – One Eliminated

In March 2011, FLITECAM was cooled in the IR Lab at UCLA in order to test a new set of narrow band filters installed in the second filter wheel. Erin Smith and Ian McLean performed the tests. These tests revealed an arc-like "glint" feature in the upper left corner of each frame taken when imaging with any of the newly installed narrow band filters in filter wheel 2 (FW2) and an open position in filter wheel 1 (FW1). However, the glint disappeared when any of the narrow band filters was paired with an order sorting filter in FW1 that passed through the light that should be seen by the narrow band filter in question but blocked out longer wavelength light (see Figure 2.3). This result indicated that there was either 1) a red leak in the narrow band filters themselves or 2) that long wavelength light passing through the first wheel had somehow bypassed the second filter and scattered, re-entering the beam before it reached the camera lenses and was imaged onto the detector. The distinct and repeatable nature of the "glint" (its location and shape were consistent in all of the filter configurations in which it was present in both the May 2011 and further May 2012 tests), led us to favor the second hypothesis.

Visual analysis of the Paschen-α (henceforth Pa α) images revealed what appeared to be two glints superimposed: 1) the "arc" glint seen in images taken with the other narrow band filters, and 2) a second, more diffuse glint along the left side of the images (see Figure 2.3).

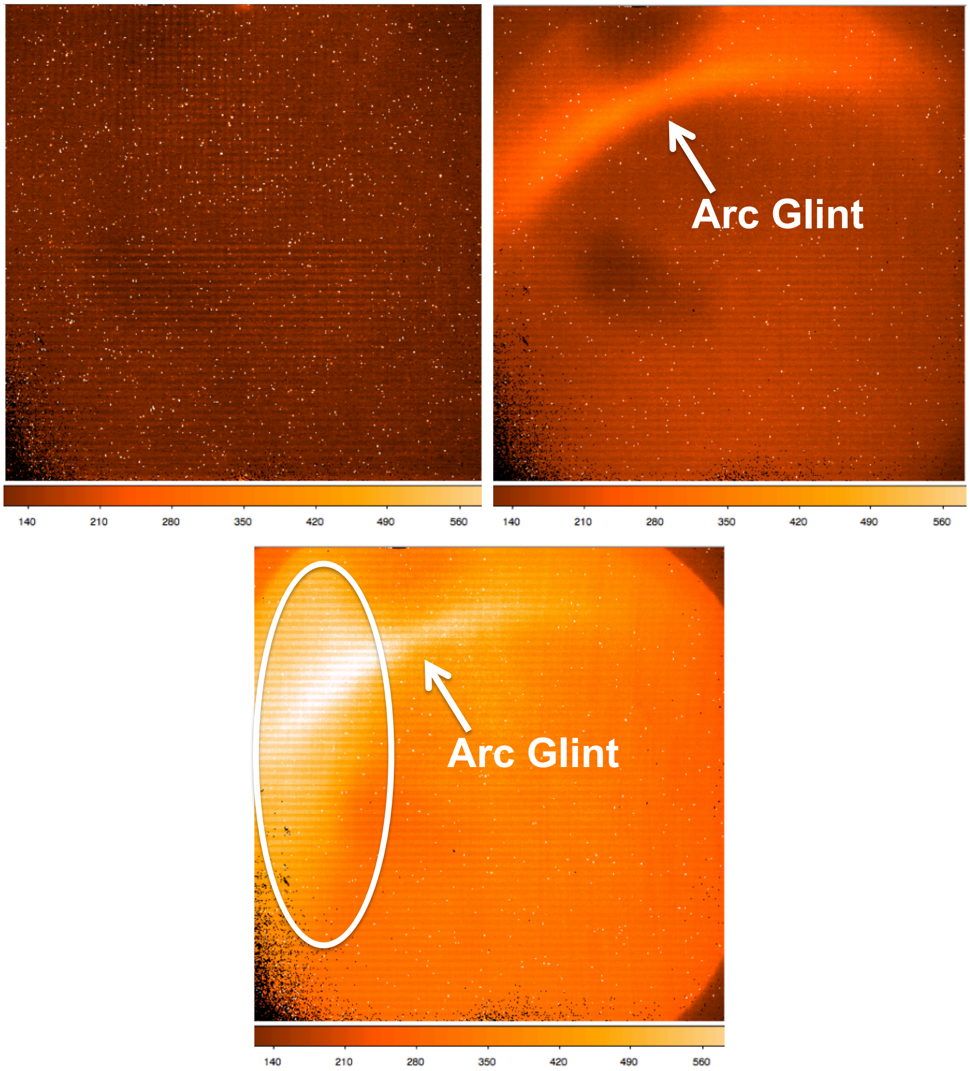

Figure 2.3 May 2012 Cool Down Results– All three of these images are 300s exposures and they have all been scaled to the same count range. They should all be dark. Top Left: An image of the FLITECAM dust cover taken with FLITECAM's J-band filter in FW1 and Pa α Cont. in FW2. This combination should and does produce a dark image. Top Right: Another image of FLITECAM's dust cover taken with the M band filter in FW1 and the Pa α Cont. filter in FW2. The arc shaped glint in the upper left hand side of the frame is labeled and clearly noticeable. Bottom: An image taken with the M band filter in FW1 and the Pa α filter in FW2. An second diffuse glint in addition to the arc glint is circled on the left side of the image.

The Pa α filter is adjacent to a grism on one side and to an open filter slot on the other side. At the time of the March 2011 and May 2012 tests, the open position was also adjacent to the pupil viewing (PV) singlet lens. The other narrow band filters in the second wheel are not anywhere near the open position or the PV lens, but are instead surrounded by grisms and other narrow band filters. Thus we suspected that the extra glint may be due to the Pa α filter's unique neighbors – either the open position or the PV lens.

An inspection of FLITECAM's second filter wheel showed that, although the outer surfaces of the wheel are black anodized, the inner rim of the open position next to the Pa α filter was un-anodized, shiny aluminum. This shiny surface was eliminated by inserting an empty, black-anodized filter holder into the open position. Adding the filter holder not only eliminated a potential reflective surface, it also reduced the aperture size of the "open" position to match the aperture size of the filters in the second wheel. We also removed the PV lens from the second filter wheel. This lens only serves to magnify the pupil viewing image, so removing the lens does not prevent FLITECAM from meeting the requirement of having a pupil viewing mode. In place of the lens, we inserted a aluminum "blank" (a black anodized disk inside a filter mount) into the second wheel, which would allow us to test whether a blank+blank or open+blank filter configuration showed any evidence of a glint. In both blank+blank and open+blank configuration, no light should reach the detector. Finally, we extended a baffle above the back end of the Pa α Continuum (henceforth Pa α Cont.) filter by mounting an anodized FW2 filter mount on top of the now-defunct PV lens collar (which held the singlet lens in place) and attaching both to the standard Pa α Cont. filter mount (see Figure 2.5).

After making these changes, FLITECAM was cooled and tested in the UCLA IR Lab during October 2012. Key results included (also see Figure 2.4):

1. Inserting a blank into the second filter wheel confirmed that a blank + blank configuration was indeed dark.
2. Covering the shiny rim in the open position in the second filter wheel and/or removing the singlet PV lens eliminated the diffuse 'extra' glint originally seen in the Pa α images.
3. The baffle tube around the Pa α Cont. filter did not eliminate the arc glint.

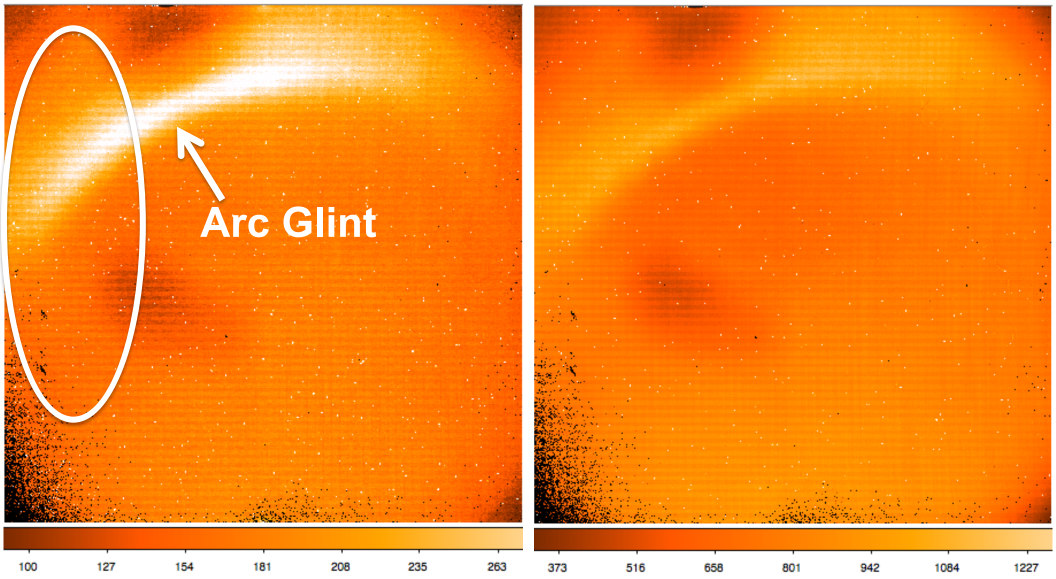

Figure 2.4 Left: An image taken in the M + Pa α configuration. While the arc glint (labeled) is still present, the diffuse glint caused by either the shiny open adjacent to the Pa α filter or the nearby PV lens (previously enclosed in the circled region of the detector) is now gone. Right: A open + blank image confirming that the arc glint is not due to a light leak in the narrow band filters. Both images are 300s exposures and should be dark.

4. The new open+blank configuration showed the same arc glint seen in the narrow band filter images.

The fourth result is significant because it confirmed our hypothesis that the arc glint was not caused by a red leak in the narrow band filters themselves. Even with a blank filter in the second wheel, as long as long-wavelength, M band light was allowed to pass through the first wheel, the result was an arc glint. Thus, the next task was to determine how thermal light was bypassing the filter in the second wheel and re-entering the beam. By eliminating that path, we would eliminate the arc glint.

2.1.3 Diagnosing and Eliminating the “Arc” Glint

After the elimination of the diffuse glint in the Pa α images in October 2012, I undertook a series of methodical on-axis modifications– altering the space seen by the beam both in front of and behind the two filter wheels– to better characterize the arc glint. In December 2012, I stopped down each filter position in FW1 that allowed long wavelength light through to the second wheel: the *M* filter, the *L&M* filter, and the open position. The purpose of this change was to decrease the amount of long wavelength light reaching the second filter wheel and thus the amount of long-wavelength light allowed to flood the backend of the instrument. Cold tests showed that the stops in the first filter wheel slightly decreased the overall amount of light incident on the detector, as expected, but did not eliminate the glint.

In February 2013, we switched our focus to the back-end of the instrument, in the space between the fold mirror at the exit of the filter wheel module (fold mirror #4 in Figure 2.1) and the camera barrel. The addition of the PV slide after the first commissioning runs at Lick Observatory had greatly opened up this area. Prior to the addition of the slide, a cylindrical, IR black baffle enclosed the distance between FLITECAM's fourth fold mirror and the camera lens mount. The baffle not only served to block out stray, off-axis light from entering the beam, but also slightly stopped down the entrance to the camera. Without this extra stop, the edges of the first lens and its mount in the camera lens barrel were visible to the naked eye. Stopping down the camera barrel entrance to its Lick specifications would help prevent stray light that could be hitting these edges and entering the beam. Thus, we shortened the original Lick baffle tube so that it would come as close as possible to the PV slide support wall without impacting the movement of the PV slide. We also had a groove machined into the backside of the baffle into which we could place interchangeable IR black stops that stop down the beam in front of the camera barrel to 93%, 88%, and 83% of the camera barrel lid diameter. Each of these stops block off the camera lens mount and stop potential stray light from reflecting off the mount, and re-entering the beam. The results of our light-leak cool down tests showed that the baffling behind the PV lens slide and in front of the camera barrel were not effective in eliminating the glint, indicating that the back end of FLITECAM's optical path was not contributing to the glint problem.

All of our tests seemed to be pointing us back to the filter wheel module. Though we had made several modifications to individual filters in the box, we had by no means eliminated all of the shiny aluminum surfaces in the box or even on the outer sides of the box. FLITECAM

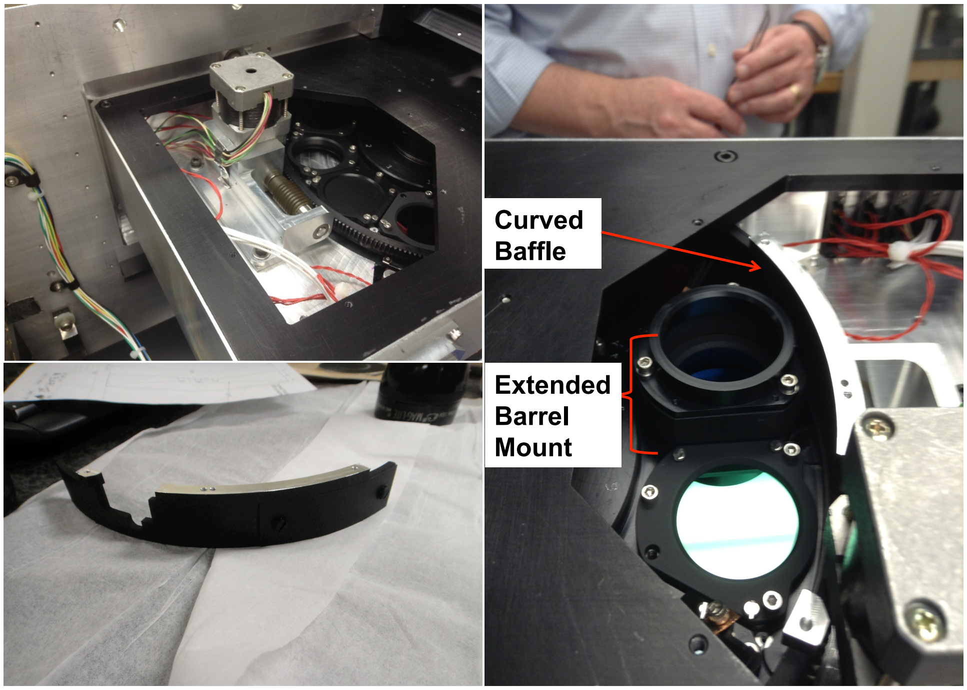

Figure 2.5 Top Left: A view of FW2 from the open FW2 hatch with no baffles installed. Note the shiny, un-anodized aluminum in the filter wheel module. The additional baffles installed in March 2013 were designed to eliminate potential reflections off of these un-anodized surfaces. Right: The ‘barrel’ mount and curved baffle installed. Bottom Left: The curved, IR black baffle before installation.

was scheduled to begin commissioning in the “FLIPO” configuration in April/May 2013, so an invasive examination of the filter wheel module was not possible at this point. Because all the narrow band filters in FW2 could be paired with order-sorting filters to eliminate the glint, we were not concerned about FLITECAM’s ability to meet its commissioning and early science goals during “FLIPO” commissioning, even if the root cause of the glint was not eliminated prior to delivery. However, we would naturally prefer to deliver a system without a light leak, so we made one more set of modifications for FLITECAM in March 2013 before delivery to SOFIA. These modifications focused on making the filter wheel module as IR black as possible without dismantling the entire box and losing alignment of the Lyot stop. Changes included: temporarily installing an IR black baffle (painted with Aeroglaze® Z306 black paint) on the front side of the filter wheel box facing the camera to cover unpainted aluminum, and adding a new curved, IR black baffle on the back side of the FW2 (see Figure 2.5). The curved baffle is attached to the FW2 access hatch by two long screws that just lift the baffle off of the second filter wheel, allowing the wheel to rotate freely. The curved baffle was designed to stop any potential, off-axis scattered light incident from the back end of the FW2 enclosure from re-entering the beam. Instrument testing in the lab immediately prior to shipping to SOFIA verified that the new baffles did not eliminate the arc glint, so a thorough investigation of the filter wheel box was planned upon FLITECAM's return to UCLA in Summer 2013.

Despite the outstanding glint, FLITECAM was successfully delivered to the Dryden Aircraft Operations Facility (DAOF) for "FLIPO" commissioning on April 9, 2013. Before installation on SOFIA, FLITECAM was first co-mounted to HIPO on the TAAS (Telescope Assembly Alignment Simulator) to verify the alignment of both instruments. After successful TAAS testing, FLIPO was installed on SOFIA and electromagnetic interference testing (EMI) was performed. FLIPO then had three successful nights of line operations (line ops). Line ops are nighttime ground operations that test system functionality. SOFIA is towed out of the hangar and the SOFIA team (including science instrument teams, telescope operators, mission directors, and safety technicians) carry out observations as they would in flight. The only differences between line ops and in-flight observations is that the Observatory is not airborne during line ops and the telescope can only point near Polaris. During FLIPO's April 2013 line ops we tested crucial instrument software communication with the telescope, verified instrument bore sight positions, and exercised all of our standard observing modes. Unfortunately, a problem with the telescope power system immediately prior to our first flight led to the cancellation of the May 2013 FLIPO flight series. FLITECAM was subsequently returned to UCLA, where we recommenced our investigation of the arc glint.

On June 26, 2013, we removed the filter wheel module from the FLITECAM instrument, taking special care to measure the exact position of the filter wheel box on the optical bench before removal to ensure that we would achieve the same alignment when the filter wheel module was re-installed. Once the filter wheel was removed, it was placed on a lab bench in one of the Lab's clean rooms. With the lights off, we performed a series of optical flashlight tests to see if we could recreate a glint phenomenon. Starting with the open filter position in FW1 and a blank filter in FW2, we positioned the flashlight in front of the Lyot stop at the entrance to the filter wheel module and held a piece of paper at the exit of the filter wheel module. Though a blank filter in second wheel should stop all light from exiting the filter wheel box, we were immediately able to confirm that this filter combination was not light tight, even to optical light. When pointing the flashlight directly through the Lyot stop (i.e. on-axis), we imaged a crescent shape on the paper at the exit of the filter wheel module. Closer examination of the filter wheel box revealed that the circular through hole between the two filter wheel enclosures (see Figures 2.2 and 2.6) was large enough to be partially visible from the filter adjacent to the filter in the beam. For context, the SOFIA beam reaches a pupil at the entrance to the filter wheel box, so the beam is expanding as it approaches the two filter wheels. By the time incident light reaches the second filter wheel, the beam diameter is 1.3 inches. However, the circular aperture between the two wheels, which the beam encounters before reaching the second filter wheel, had an oversized diameter of 1.753 inches.

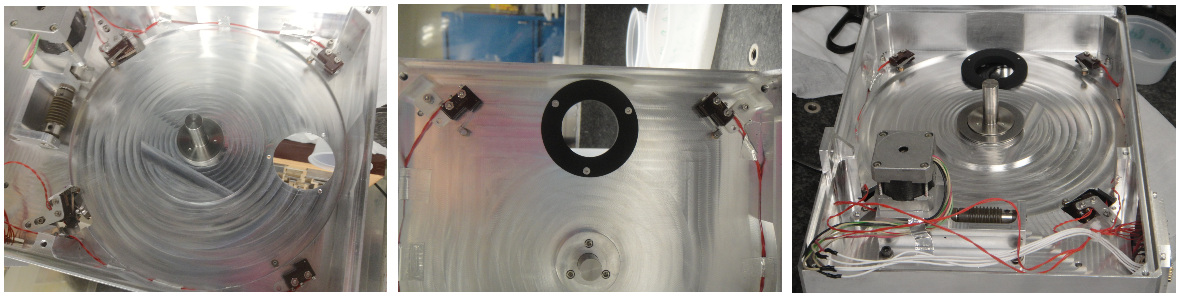

Figure 2.6 Left: The FW2 side of the FLITECAM filter wheel module with the filter wheel removed. Three holes were drilled adjacent to the circular aperture in July 2013 to accept a new nested baffle. Middle: A face-on view of the FW1 side of the filter wheel module. The IR black, nested baffle is clearly visible. Right: An edge-on view of the FW2 side of the filter wheel module. The nested baffle on the far side of the image extends from the center wall in the filter wheel box and is almost flush with FW2 when the filter wheel is re-installed.

This oversized aperture is particularly problematic for FLITECAM's longest wavelengths, where the thermal backgrounds are higher. With a significantly oversized (and shiny) aperture to pass through, thermal photons can scatter and flood the second wheel, partially bypassing the second on-axis filter and finding scattering surfaces (such as the rounded, un-anodized aluminum side of the box immediately adjacent to the filter wheel on the side closest to the beam) to bounce off of and re-enter the beam behind the second filter wheel. The long wavelength light is further abetted by the fact that, while the first filter wheel has minimal clearance from the central aluminum wall, the second wheel is offset from the center wall to accommodate the central wheel shaft. This extra space between the central wall and the second wheel leaves the light more room to scatter before entering the second filter. In order to prevent long wavelength light from bypassing the second on-axis filter, we designed an IR black (painted with Aeroglaze® Z306 black paint) two-piece, nested baffle that can be inserted into the circular aperture and secured by three countersunk socket head fasteners. On the FW2 side of the filter wheel enclosure, this baffle extends from the center wall ∼0.165 inch to to prevent light from bypassing the second filter wheel. We matched the open diameter of the baffle to the FW2 mount lids (1.35 inches), which is significantly smaller than the original 1.753 inch aperture. Once this baffle was in place, we re-assembled the filter wheel module, performed warm filter wheel functionality tests, and re-installed the filter wheel module onto the FLITECAM optical bench.

In August 2013, FLITECAM was cooled down and tested following the same standard tests used in previous glint investigation cold tests. As illustrated in Figure 2.7, the filter wheel baffle successfully eliminated the arc glint.

2.2 Filter Wheel Logic and Look-Up Table Development

During cold testing in the lab and at SOFIA, I noticed that certain filter moves would lead to unexpected charge persistence on the FLITECAM detector. Charge persistence, as the name suggests, is latent charge left on the detector after a light source has been removed. While the detector is continuously read out when it is idle, FLITECAM does not have a shutter. Thus, moving the filter wheels through any filter that allows ∼3-5 μm light through to the detector can lead to charge persistence. Eliminating charge persistence is doable, but

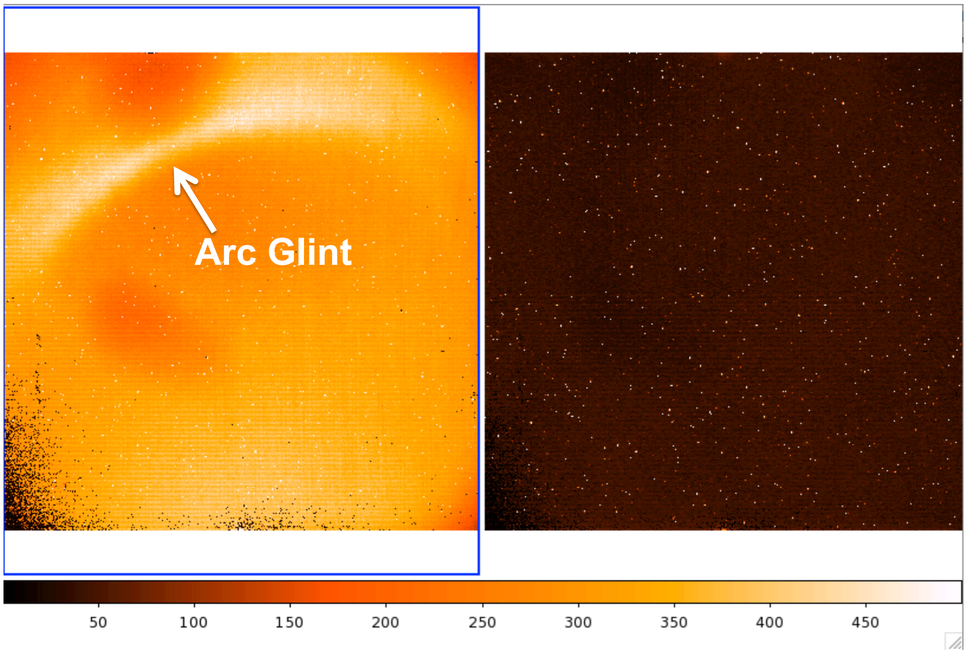

Figure 2.7 Two 300s images taken with FLITECAM's M band filter in FW1 and a blank filter in FW2. Both images are scaled to the same count range and should be dark. The first image (left) taken in February 2013 shows one of FLITECAM's two light leaks as an arc shaped glint (labeled) across the top left of the image. The second image (right), taken in August 2013 after a new baffle was installed in the filter wheel module, is dark as it should be with the light leak removed.

requires the instrument operator to take either several long dark exposures or several short dark exposures with many co-adds to clear the latent charge, both of which lose precious observing time. Moreover, because both of FLITECAM's filter wheels feature an 'open' position, care has to be taken to move each filter individually. Moving both filters through an open position simultaneously, can allow short-wavelength, visible light from, for example, a bright star in FLITECAM's field of view, onto the InSb detector. When these short-wavelength photons strike a pixel, they can cause partial ionization that desensitizes the pixel until the next time the detector is cryocycled. Since an entire cryocyle process takes a minimum of two weeks, opening both of FLITECAM's filter wheel simultaneously should be avoided. With these two scenarios in mind, it became clear that a thorough understanding of FLITECAM's Filter Wheel Logic would be crucial for operating the instrument and for informing the observing software, which is capable of semi-automated observing through the use of Automated Observing Requests (AORs).

2.2.1 Investigating Filter Wheel Motion

After FLITECAM's filter wheel module was removed from the optical bench, but before it was disassembled to install the nested baffle described in Section 2.1.3, we carried out a series of warm drive tests to determine the movement of the two wheels. In order for the FLITECAM mechanism software to track wheel movement, the wheels themselves are 'keyed' with a set of four half circle discs protruding from the wheels themselves. These four half circle discs are spaced around the wheel and, when the wheel rotates, the discs trigger a combination of four micro-switches. Different trigger combinations denote different positions along the wheel. The filter wheel movement logic is summarized below:

- Homing, as the name suggests, sets the 'home' position for each wheel. In both wheels, the home position, also denoted as position 1, is a 'blank' filter.
- When homing a wheel, the wheel moves counterclockwise. The first 360° rotation of the wheel moves quickly. If the home position is found in this first rotation, the wheel will be put the home position in the beam path and the homing process will be complete. If the home position is not found in the first 360° rotation of the wheel, the wheel then slows down and finely steps through each gear tooth until the home position is found.
- Once the home position is set, the wheel will NOT pass through the home position to reach a target filter position (i.e. it will AVOID passing through the blank when moving to a new filter).
- In general, the wheels take the shortest path between the current filter and the requested filter, moving clockwise or counterclockwise.
- Avoiding the home position means that the wheel will take the shortest path between the current filter/grism and the selected filter/grism UNLESS the shortest path in-

cludes passing through home. In the second case, the wheel will take the longer path between the two.

- The wheel always rotates clockwise when returning to the ‘home’ (blank) position.

2.3 Resolution Measurements

SOFIA does not have a facility flat field or arc lamp source for spectral calibration. Therefore, during the August 2013 cold tests, we obtained arc lamp data for calibrating FLITECAM’s grism observations. FLITECAM arc lamp spectra are attained by attaching an integrating sphere to FLITECAM’s SOFIA mounting flange and attaching the flange to FLITECAM (see Figure 2.9). Resolution measurements ($R = \lambda/\Delta\lambda$) were obtained using the $\sim 2''$ slit for all of FLITECAM’s spectral bandpasses with the exception of ∼4.4-5.5 μm (the “LMA” grism combination) which immediately saturates in the lab and is only observable on SOFIA in the ‘solo’ configuration. I measured the $\sim 2''$ slit values using Xe and/or Ar arc lamp data and applying the standard formula:

$$R = \frac{\lambda}{FWHM * LD}$$

where λ is the location of each arc line (in μm) measured in vacuum, FWHM is the full width at half maximum of the line in pixels, and LD is the linear dispersion in μm/pixel. The results of these measurements are shown in Figure 2.8. The average resolution of FLITECAM’s $\sim 2''$ slit is ∼1300.

It is instructive to compare the measured resolution to the expected resolution set by the instrument design. In general, the slit-limited resolving power of a grism is given by:

$$R = 206265\,\frac{(n-1)\,D_{pupil}\,tan(A)}{D_{tel}\,s}$$

where n is the index of refraction, D_{pupil} is the diameter of the pupil, A is the grism angle, D_{tel} is the diameter of the telescope, and s is the width of the slit in seconds of arc (see McLean 2008). For KRS-5 grisms, the value of n is slightly wavelength dependent and varies from ~2.45 at 1 μm to ~2.38 at 5.5 μm. For FLITECAM, D_{pupil} = 28 mm, A = 34.4°, and D_{tel} = 2.5 m. Plugging in the values for FLITECAM's ~2″ slit (s = 2″) yields an average resolution of ~1100. In practice, however, the so-called 2″ slit is closer to a 1.833″ slit. The FWHM of the illuminated ~2″ slit covers 3.9 pixels on the FLITECAM detector. With a plate scale of ~0.47″per pixel, this leads to an actual slit width of s=1.833″. A narrower slit implies a higher average resolution (~1200). Given the large uncertainties on the arc lamp measurements, this is roughly consistent with the R~1300 value I measured empirically.

At Lick Observatory, where the seeing was close to 1″, FLITECAM spectroscopy was typically observed using the ~1″ slit. As is true for the ~2″ slit, the ~1″ slit is slightly narrower than 1″ in practice, covering 2.1 pixels on the FLITECAM detector. This implies that s = 0.99″ and R ~2230. However, arc lamp measurements of the 1″ slit made by Erin Smith and presented in Smith & McLean (2006) yield an average resolution of R ~1700. As a check on Erin's resolution measurements, a second resolution estimate was made using OH sky lines in a single grism combination. The sky line measurement suggested that the resolution of the ~1″ slit is actually closer to ~1800-1900. However, both the arc lamp and sky line resolution measurements are well below the predicted value of R ~2230. We originally suspected that the physical size of the ~1″ slit width was wider than the design specification, but a check of both slits using a feeler gauge in the lab verified that both slits were machined to the proper specification. We now suspect that the cause of the lower spectral resolution in the narrow slit is post-dispersion aberrations in FLITECAM's optics.

2.4 Thermoacoustic Oscillations Mitigation

As FLITECAM was prepared for its first flights on SOFIA in 2011, it was noted that the hold time for liquid helium in the cryostat had deteriorated from the ~15 hours that had been achieved when FLITECAM was used at Lick Observatory to ~10 hours. Several changes had been made to the cryogenic venting system to meet flight safety standards, including the addition of a cluster of burst disks and pressure relief devices (PRDs) at the end of the helium vent line. Although disappointing, 10 hours was still acceptable for flights. However,

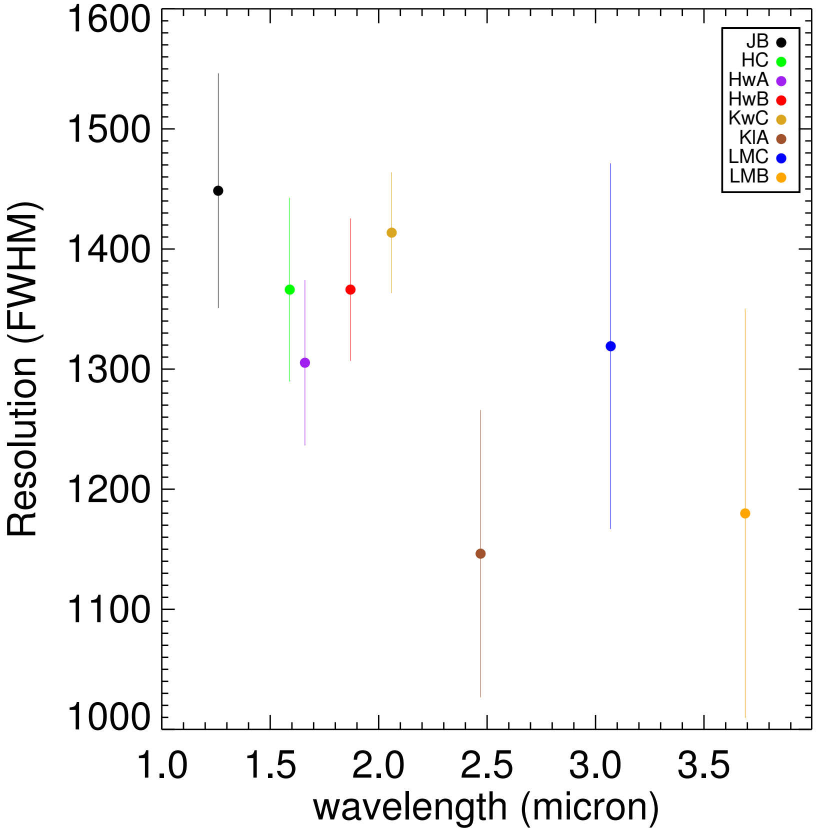

Figure 2.8 The 2″ slit resolution measurements for the individual spectral bandpasses observable with FLITECAM in the FLIPO mode. The error bars indicate the standard deviation of the individual line measurements within a single grism configuration. The larger errors at long wavelengths are due to the high backgrounds and paucity of arc lines at these wavelengths.

in September 2013 the hold time dropped unexpectedly to ∼6 hours, which is less than the normal SOFIA flight time of 9-10 hours. This reduced hold time manifested after several PRDs were removed, sent to NASA Dryden (now NASA Armstrong) for certification, and reinstalled. FLITECAM was scheduled to return to SOFIA in mid-September for a second attempt at FLIPO commissioning, so we were not immediately able to investigate the hold time issue. Shortened flights were designed to accommodate FLITECAM's reduced hold time, but after just one of these flights, the October 2013 USA government shut down led

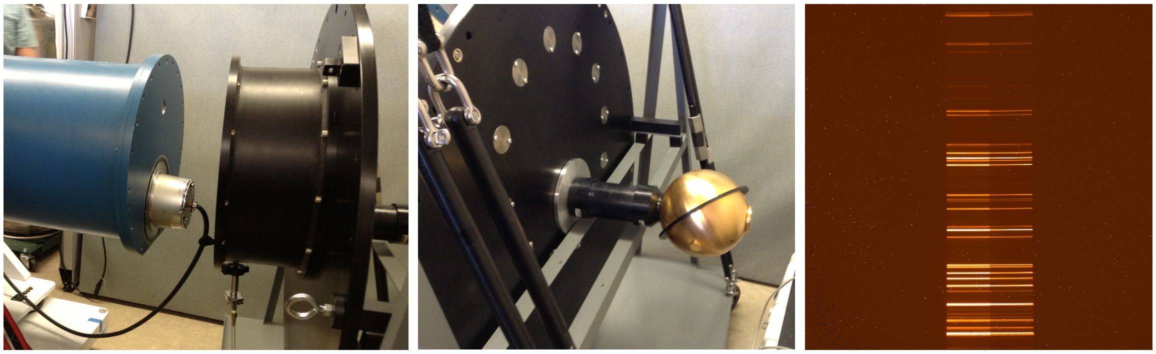

Figure 2.9 Left: Preparing to attach FLITECAM's mounting flange (black) to the cryostat (blue). The silver cap is FLITECAM's window cover and is removed just prior to bolting the flange to the cryostat. Middle: The integrating sphere mounted to the back end of FLITECAM's mounting flange. Right: An argon arc lamp spectrum in FLITECAM's JB grism combination (1.140-1.385 μm).

to the cancellation of the FLIPO flight series.

In January 2014, a series of cold tests in the IR Lab ultimately traced the reduced hold time to thermoacoustic oscillations in FLITECAM's helium vent structure. Thermoacoustic oscillations are essentially sound waves that can be driven by a pressure build-up in a system with a large temperature gradient[1]. When dealing with very cold cryogenic liquids, like liquid helium (~4K), it is not uncommon to encounter thermoacoustic oscillations. The basic problem is as follows: Consider a closed system with a liquid helium reservoir at one end and a warm closed tube at the other end. As the liquid helium begins to boil off, cold helium gas moves from the liquid helium reservoir to the warm, low-pressure end of the tube. If the gas is not allowed to vent from the tube, warm gas builds up at the end of the tube. Eventually, seeking a lower-pressure environment, that warm gas will drive back to the liquid helium reservoir. This movement of warm gas causes the liquid helium to boil off more quickly, creating a new store of cold gas that is moved toward the warm end of the tube, and the oscillations continue. If the gas is allowed to vent from the warm end of the tube, however, these oscillations can be damped.

---

[1] A nice introduction to thermoacoustic oscillations can be found on the Meyer Tool and Manufacturing, Inc. website: http://www.mtm-inc.com/ac-20110117-thermoacoustic-oscillations.html

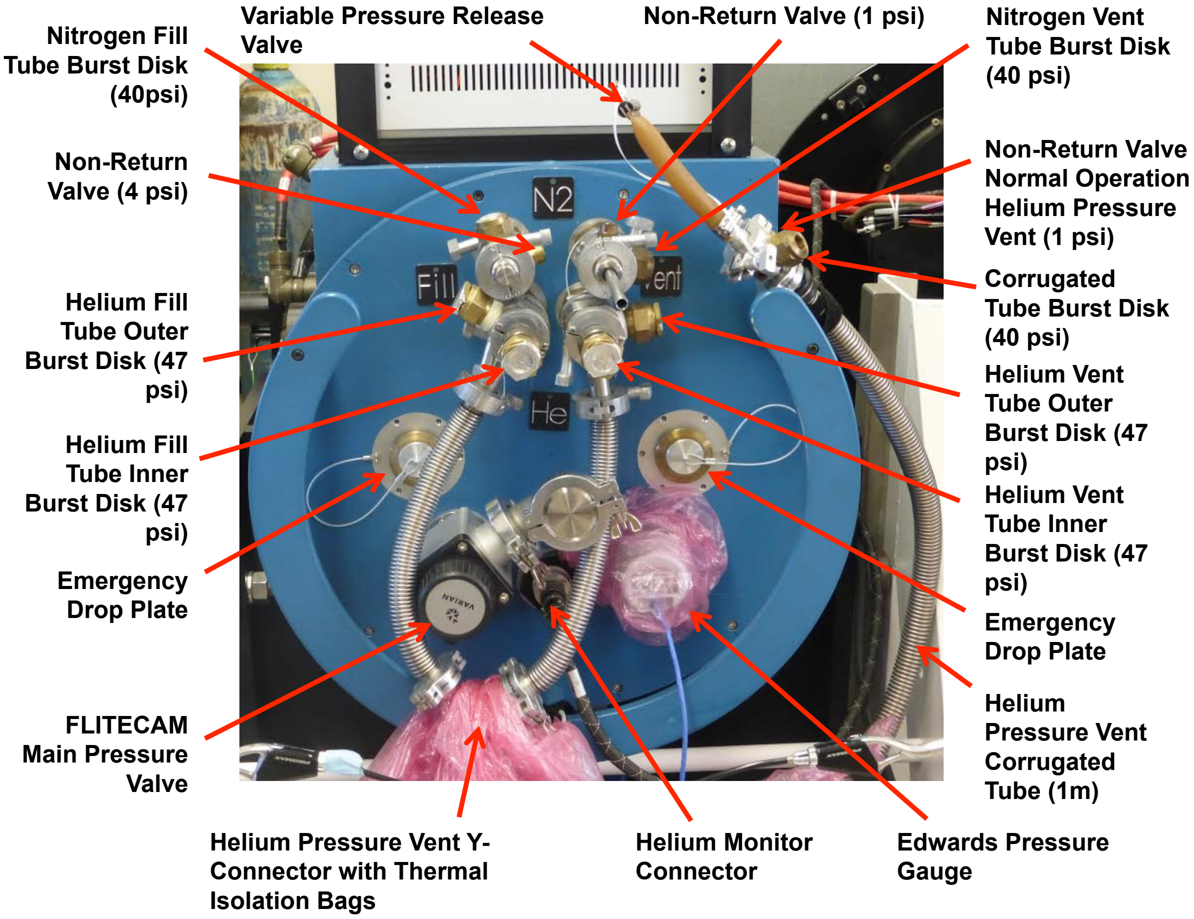

Figure 2.10 A modified version of Figure 6.2.4-3 in FLITECAM's System Safety Assessment document showing the backend of the FLITECAM cryostat in 2015, including the Nitrogen and Helium vent systems. Notice the variable pressure relief device (i.e. rubber hose assembly) at the end of the helium vent line. The addition of this hose significantly improved FLITECAM's liquid helium hold time.

The FLITECAM helium vent system (see Figure 2.10) vents He gas from the liquid helium dewar through a system of steel bellows capped with a spring-loaded PRD and burst disk. The bellows are designed to be sufficiently long (1 meter) that the spring-loaded PRD at the end of the bellows does not freeze over and can safely vent the Helium gas from the system[2]. The spring-loaded PRD is a non-return valve designed to vent at 1 PSI without

---

[2] As illustrated in 2.10, both the Nitrogen and Helium lines include spring-loaded PRDs for standard venting and a series of ~40-50 PSI burst disks for emergency venting (i.e. in the event of a vacuum failure and the resulting rapid boil-off of the liquid cryogens).

sucking air into the vent system, which could lead to an ice plug. We ultimately determined that FLITECAM's thermoacoustic oscillations were driven by the opening and closing of this PRD. Our series of cold tests included a successful test that added a variable PRD to the end of the helium vent line. This variable PRD, essentially a classical rubber hose closed at one end and with a narrow slit cut into its side, permits continuous venting of helium gas without building up pressure. Immediately after the variable PRD's installation, the oscillations in the helium vent line were significantly reduced, and the hold time returned to Lick Observatory times (∼12-15 hours; see Figure 2.11), adequate to keep the detector cold for an entire flight. This variable PRD was added to a blank port at the end of the He vent line and does not bypass any of the previously existing PRDs in the vent system.

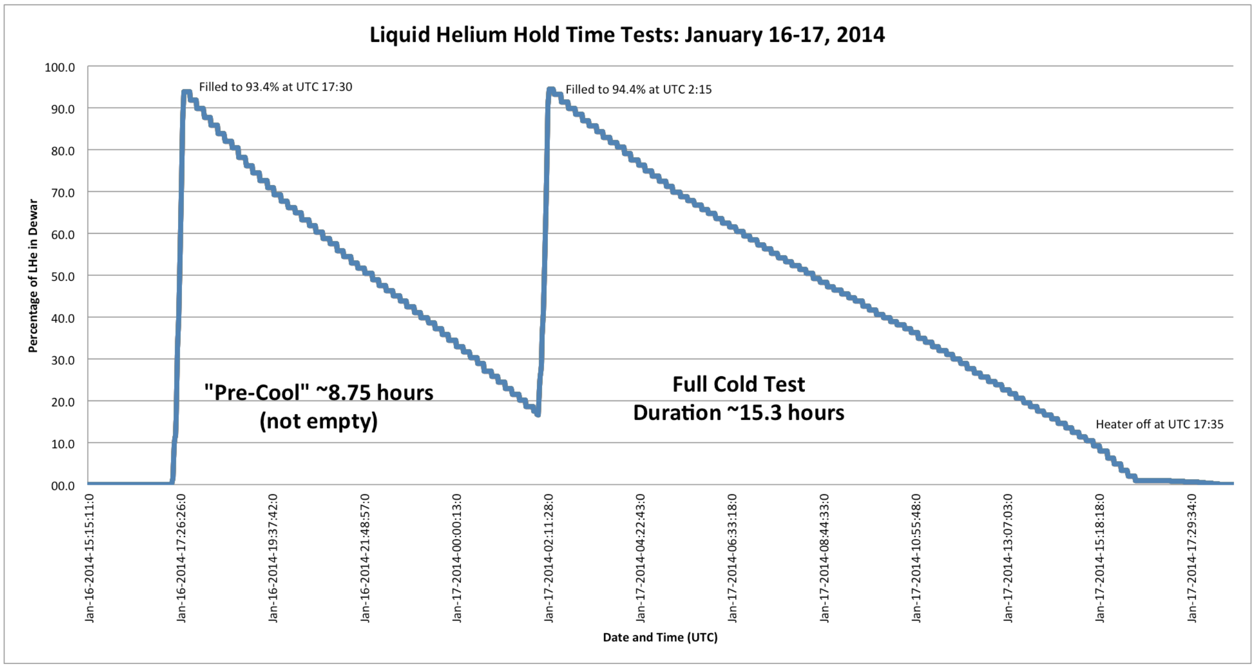

Figure 2.11 Liquid Helium (LHe) level as a function of time after a variable PRD had been added to FLITECAM's Helium vent line during the January 2014 thermoacoustic oscillation investigation. FLITECAM's LHe reservoir was 'pre-cooled' to remove heat. Then we filled the reservoir to 'full' (∼95%) and let the LHe boil off. The detector heater, which keeps the detector stable at 30 K, shut-off 15.3 hours after the fill completed, implying a better than 15 hour hold time for this cool down.

The question remained, however, as to what caused the noticeable drop in hold time in September 2013. Just prior to the Physical Configuration Audit (discussed below), we discovered that the original 1 PSI PRD had been accidentally swapped out for a 4 PSI PRD when the PRDs returned from certification. This swap explains the sudden change in helium hold time in September 2013. By requiring a large build-up of pressure to activate the PRD, we were driving oscillations in the vent line. The addition of the variable PRD allowed the He gas to vent at a lower pressure and significantly improved the hold time.

2.5 Cryostat Emergency Vent Modification: Drop Plates

As a precaution following the sudden decrease in helium hold time, the NASA Engineering and Safety Center (NESC) conducted an independent safety assessment of the FLITECAM cryostat. Particular attention was paid to FLITECAM's cryogen venting pathways; each pathway was independently modeled and examined. As part of this review, the NESC requested a modification to the housing for two pop-off valves that are located on the exterior of the cryostat. FLITECAM's liquid nitrogen and liquid helium dewars are both contained in a larger cryostat that is under vacuum when in operation. The pop-off valves are designed to be emergency pressure-relief conduits in case the cryostat over-pressurizes. These valves 'pop off' the cryostat, allowing the system to vent to the air. It is necessary to contain the valves (two blank flanges) after they have released, which is the purpose of the valve housing. The original design of the pop-off valve housing was a spring-loaded, 'top hat' design (see Figure 2.12). In this design, when a pop-off valve releases it encounters a spring that retards its forward motion. Both the spring and the valve are enclosed in a aluminum 'top hat' that is affixed to the cryostat with six screws. The NESC was concerned that, in the 'top hat' design, the pop-off valves would not clear the opening to the cryostat and thus would impede the flow of gas out of the cryostat. We proposed a new valve containment design developed by the IR Lab's machinist, Ted Aliado. The new design features an aluminum plate bonded directly to the valve using aircraft grade epoxy (Metalset A4 Aluminum filled epoxy). This plate is in turn attached to a coated stainless-steel tether affixed to one of the previously existing tapped holes in the cryostat. In the new design, the valve is allowed to

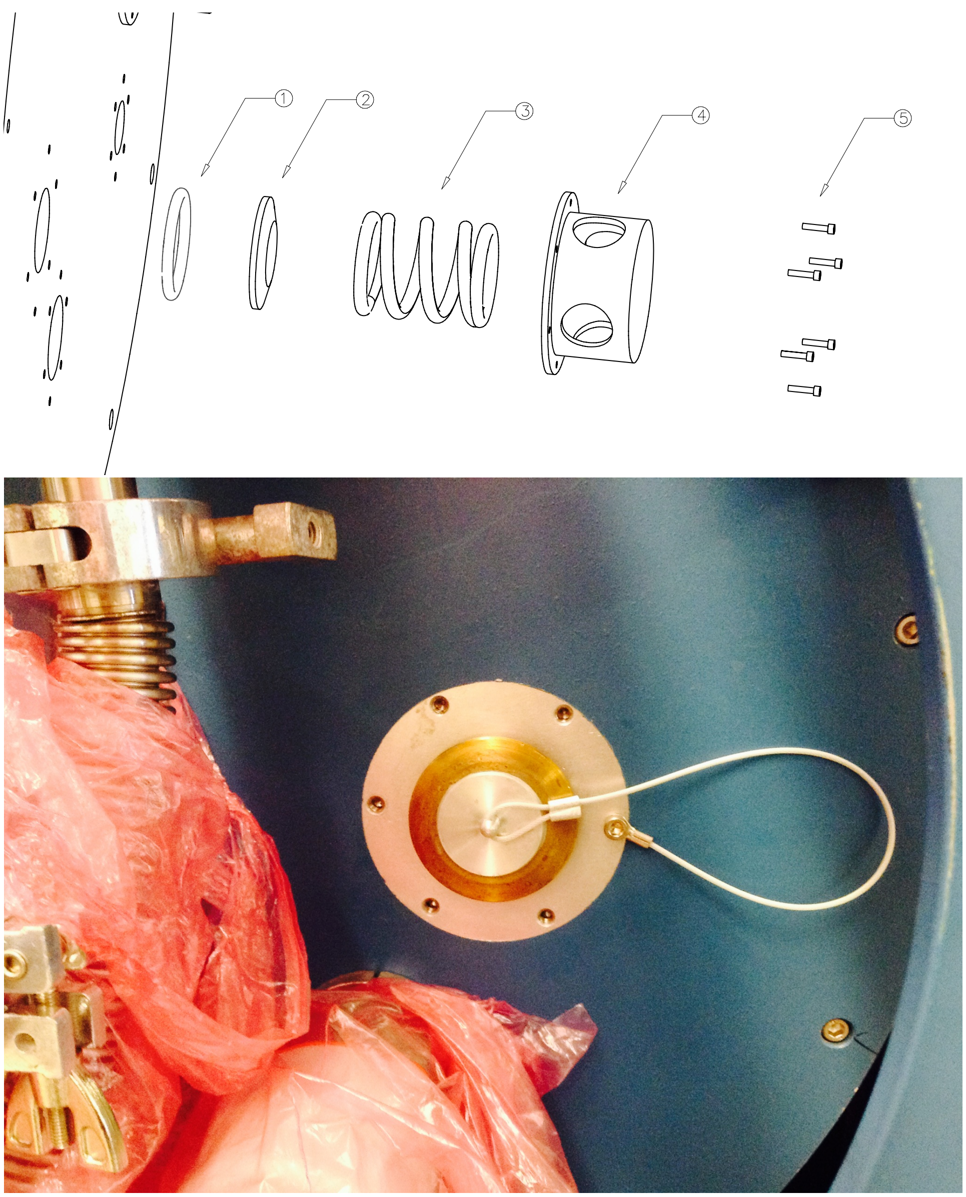

Figure 2.12 Top: An assembly drawing created by IR Lab Engineer, George Brims, illustrating the original ‘top hat’ housing for FLITECAM’s emergency cryostat vent valves. The component labels on the drawing refer to 1) o-ring, 2) blank flange, 3) spring, 4) ‘top hat’ housing, 5) six fasteners. Bottom: The new drop plate housing for FLITECAM’s emergency cryostat vent valves. This configuration includes an o-ring, blank flange, aluminum tether-attachment plate, coated stainless-steel tether, and one fastener.

clear the cryostat opening, but is still contained by the tether. This design was approved and implemented in 2014.

2.6 C Grism Investigation

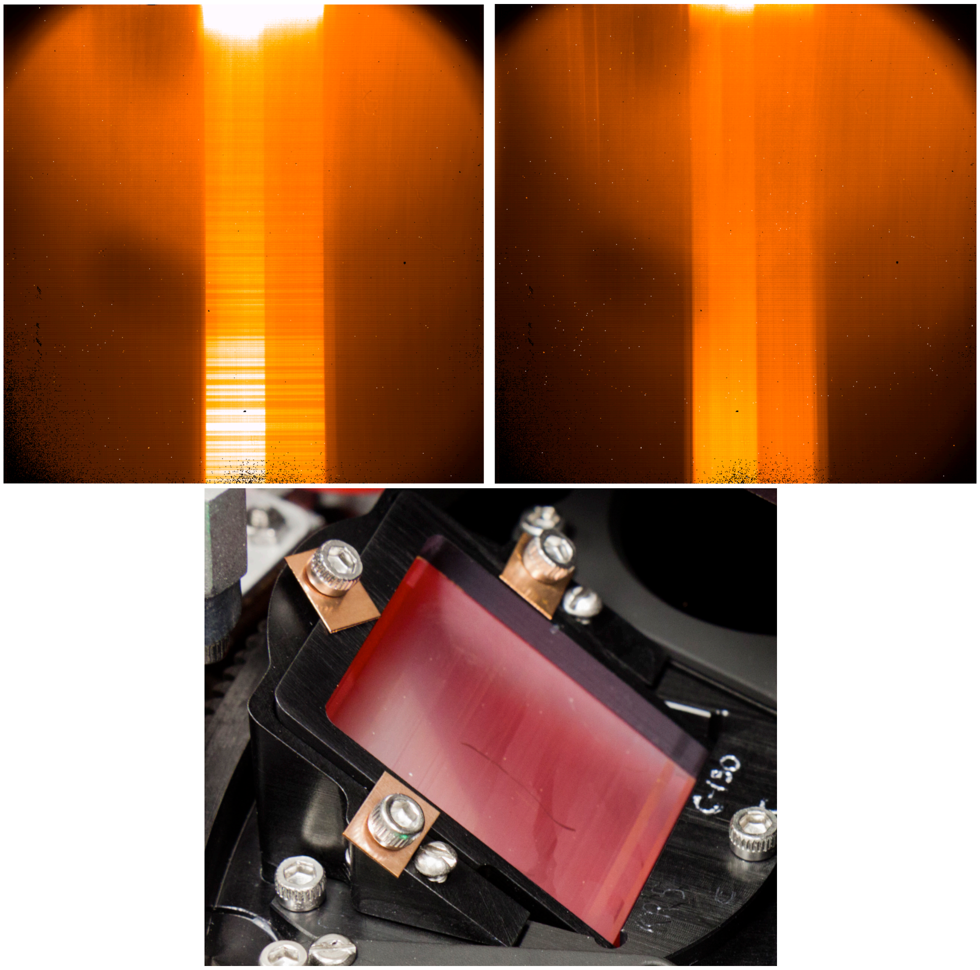

Figure 2.13 Top Left: A spectroscopic image taken with the LMC grism combination at Lick Observatory. Top Right: A spectroscopic image taken with the LMC grism combination on SOFIA. The only illuminated part of each frame should be the spectrum in the center of the image, but a semicircle-like excess background is apparent in both images. Bottom: An image of the C grism in its mount. Note the hairline ‘worm’ defect in the anti-reflective coating.

Analysis of the FLITECAM data from FLIPO commissioning in 2014 showed excess light in all spectroscopic images taken with FLITECAM’s C grism in the beam (see Figure 2.13). In spectroscopic mode, the only flux incident on the detector should be within the boundaries of the slit image. However, an examination of the C grism images shows almost a semicircle of light on the top half of the detector. An investigation of historical grism commissioning data from Lick Observatory showed the same pattern, implying that the excess light was a long-term issue and not a sudden degradation of the filter. We suspected that the excess light was either caused by an issue with the grisms mounting, such that undispersed light was being allowed to bypass the grism, or a long-term defect in the filter itself was letting undispersed light through. The C grism is the most coarsely-ruled of FLITECAM's grisms (130.2 lines/mm), so it is possible that a fabrication mistake could have occurred.

In January 2015, while FLITECAM was open for other work, we carefully inspected all three grisms. We concluded that the three grisms were mounted identically with no suggestion that the C grism was mounted poorly. The C grism does have a narrow, hairline ('worm') defect in the anti-reflective coating at the exit of the grism. However, it was not immediately clear whether this defect could cause the excess light. We recommended to USRA/SOFIA that the IR Lab team remove the grism from the optical bench for more thorough inspection and consider ordering a new grism. However, as the grism is usable as is, the SOFIA project decided to forgo further investigation. We took no further action on this item.

2.7 Acceptance Review and Physical Configuration Audit

After the successful completion of FLIPO commissiong in February 2014 (see Chapter 3 for details), the SOFIA project began preparations to accept FLITECAM as a delivered Facility Class Science Instrument (FSI). Once formally accepted and delivered, FSIs are maintained and operated by the Observatory. Two significant steps in the acceptance process are to pass a NASA Acceptance Review (henceforth AR) and to subsequently pass a Physical Configuration Audit (henceforth PCA). During the AR all major aspects of the FLITECAM system are presented to and evaluated by the Review Committee as is the readiness of the USRA team (who are contracted by NASA to manage the SOFIA instruments) to maintain and operate FLITECAM. In the UCLA IR Lab, preparation for the AR included preliminary updates to numerous documents, such as the FLITECAM Maintenance manual, the creation of new documents, such as the FLITECAM Operations Handbook, the development of AR presentations, and observing software testing due to changes to SOFIA's Data Cycle System (DCS) requirements. FLITECAM successfully passed its AR on September 4, 2014. Following the AR, FLITECAM was then required to pass a PCA. A PCA includes a review of all final FLITECAM documentation, a detailed comparison of the FLITECAM documentation to the actual physical components of the instrument and computer/electronics racks, and a review of airworthiness/safety compliance, particularly in regards to the liquid cryogen venting structure. Preparing for FLITECAM's PCA included preparing the final FLITECAM drawing package, updating outdated FLITECAM documentation identified at the AR, and providing new documentation per updated SOFIA deliverable requirements. FLITECAM's PCA occurred in the IR Lab on February 26, 2015. A representative from SOFIA/USRA performed the audit. A few lingering actions resulting from the audit were completed in the following months.

2.7.1 New Documentation

New documentation required for the AR and PCA included the FLITECAM Operations Handbook (SCI-US-HBK-OP02-2149) and the FLITECAM Assembly Manual. The FLITECAM Operations Handbook is the premier reference for FLITECAM instrument operators and instrument scientists. It covers all of the relevant information for operating and observing with FLITECAM. The Assembly Manual gives detailed instructions for opening the instrument to provide routine maintenance, such as recharging the charcoal and zeolite getters, accessing the filter wheels, replacing faulty motors/temperature sensors, and replacing the calcium fluoride entrance window. The Assembly Manual is most useful for the engineers in the Mission Operations unit of SOFIA, who are responsible for maintaining the instrument.

2.7.2 Documentation Updates

Several documents developed by the IR Lab team, most notably Erin Smith and Ian McLean, prior to 2008 were updated to reflect the upgrades made to the instrument since that time. Documents requiring updates included the FLITECAM Maintenance Manual, the PI and CW rack documents, and the Electronics document. FLITECAM's Maintenance Manual provides instructions for maintaining and handling FLITECAM in the lab and on the aircraft including instructions for safely cabling up, cryocycling, and testing system functionality. The principal investigator (PI) rack, counterweight rack (CWR), and Electronics documents, give detailed information about these individual components of the FLITECAM system. Other documentation requiring updates included: the final FLITECAM component drawing package, the System Safety Assessment, the list of FLITECAM deliverables (including in-use components and spare equipment), and the FLITECAM fastener list, which accounts for all accessible FLITECAM fasteners. The fastener list is required because FLITECAM is a airborne instrument and all accessible fasteners on the FLITECAM cryostat, CWR, and PI rack must be FAA-certified.

2.8 Conclusion

As the UCLA FLITECAM Instrument Scientists I supported a myriad of FLITECAM research and development activities in the UCLA IR Lab. Major activities included: 1) the investigation and elimination of a set of two light leaks in the FLITECAM filter wheel module, 2) the determination of FLITECAM's filter wheel logic and the development of a filter wheel look-up table in the FLITECAM observing software, 3) the mitigation of thermoacoustic oscillations in the LHe vent line, and 4) a large documentation effort, including both creating new documents and updating outdated documents, as part of FLITECAM's acceptance as a Facility Class Science Instrument for SOFIA. In the next two chapters I discuss FLITECAM's in-flight performance on SOFIA.

CHAPTER 3

FLIPO Commissioning and New Zealand Deployment

3.1 Introduction

During the summer and fall of 2011, FLITECAM was delivered to SOFIA and co-mounted with HIPO, the High-speed Imaging Photometer for Occultations (PI Edward Dunham, Lowell Observatory; Dunham et al. 2004, 2012). HIPO is mounted on-axis and FLITECAM mounts above it. A periscope composed of a dichroic beam-splitter and a silver-coated fold-mirror installed in front of HIPO and FLITECAM reflects infrared light to FLITECAM and transmits optical light to HIPO. This co-mounting of HIPO and FLITECAM (known as FLIPO) was used during line operations and four observatory verification flights in October 2011 (see McLean et al. 2012). Commissioning of FLITECAM in the FLIPO configuration was not performed on those 2011 flights because the Observatory itself was still under development. There were two attempts to begin FLIPO commissioning in the spring and fall of 2013, but these flights were postponed or curtailed as discussed in Chapter 2 of this work. Finally, six very successful commissioning flights were undertaken in February 2014. FLIPO's next flights were in Summer 2015 when FLIPO deployed with SOFIA to New Zealand. On deployment, FLIPO and SOFIA's primary tracking camera, the FPI+ (PI Jürgen Wolf, DSI), observed an occultation of a background star by Pluto fifteen days before the New Horizons mission flew by Pluto. In this chapter I present a brief update on FLITECAM's properties since the 2011 SOFIA Characterization and Integration (SCAI) flights, discuss the results from the 2014 commissioning flights in FLIPO configuration, and highlight FLITECAM's role in SOFIA's 2015 New Zealand Deployment.

3.2 Instrument and Software Upgrades from 2011 to 2014

In addition to the FLITECAM improvements discussed in Chapter 2, namely the extended liquid Helium hold time and the eliminated light leaks, several other modifications were made following the 2011 observatory verification flights. For example, overheating of the FLITECAM electronics system just prior to the verification flights in 2011 resulted in a missing detector quadrant during the flight series. After the flight series was completed, the problem of the missing detector quadrant was traced to a faulty board in the digital signal processing electronics. The problem was corrected with a spare board, and all four quadrants of the detector became fully functional again.

In early 2014, the instrument control computer which runs all of the observing control software was upgraded from a Dell PowerEdge 750 Server to an Apple Mac Mini, which was co-mounted in FLITECAM's PI rack with another Mac Mini cold spare[1]. Several improvements were also made to the instrument control software itself, including updates to the Astronomical Observing Request (AOR) software. One important change to the AOR software is the ability to accept a dither-nod-dither pattern sequence. This change allows the observer to execute a dither sequence on a target, nod to a second field, and execute another dither sequence, all while maintaining guiding on either one or two guide stars (depending on the size of the nod). The dither-nod-dither sequence is ideal for extended objects because the second dither pattern can be chosen some distance away in order to produce a clean sky frame for flat fielding.

Another notable software update was the development of a continuous data-taking mode. With one click of a button, the observer can execute as many repetitions of a single exposure as necessary. This feature is particularly useful for high cadence data observed over long observing legs, such as transits. Other more minor software changes included things such as header keyword updates for Data Cycle System (DCS) ingestion.

---

[1] A 'cold' spare computer, in this case, is an identical spare computer with all necessary FLITECAM observing software installed, but is not powered or connected to the SOFIA network. If the original instrument control computer were to fail, this spare can be quickly configured for use.

For the commissioning flights in February 2014, FLITECAM was once again co-mounted with HIPO in the FLIPO configuration (as shown in Figure 1.3). Since the time of the FLIPO flights in 2011, the dichroic beamsplitter discussed in the introduction has received a new and improved coating, with higher IR reflectivity (see Dunham et al. 2014). The IR reflection now rises rapidly from ∼80% at 1.25 m to over 95% beyond 3 μm. However the beamsplitter components remain relatively warm during flight, and therefore FLITECAM is exposed to an increased background, which limits the useful wavelength range to about 1-4 μm in the FLIPO configuration. In principle, it may be possible in the future to operate a cooling fan that will enable the FLIPO fore-optics to cool down to the temperature of the telescope.

3.3 Results from FLIPO Commissioning

The FLIPO commissioning flights in 2014, SOFIA flights #144-149, had multiple goals. Of highest priority was the commissioning of the FLITECAM instrument. Several flight legs were dedicated to boresight tests, shear-layer tests, guiding/tracking tests, dither pattern tests, nodding and offsetting tests, and image quality tests. The goal of boresight testing is to map the offset between the telescope's pointing and the instrument's pointing so that the desired sky coordinates are observed at the expected pixel position on FLITECAM's detector. A detailed discussion of SOFIA boresight calibration (with the DLR's FIFI-LS instrument) can be found in Colditz et al. (2014). The "shear layer" is the flow of turbulent air across the open SOFIA cavity. This turbulent air impacts the point spread function (PSF) of FLIPO's images, particularly for HIPO's two optical channels, and is dependent on both SOFIA's Mach number and the air density (see Dunham et al. 2014). In addition to FLIPO characterization tests, several guest investigator science programs were carried out under shared risk conditions, and Director's discretionary time was invoked to observe a Target of Opportunity – the Type Ia supernova, SN2014J, in M82. In this section, I present the results of commissioning tests and highlight some of the exciting scientific capabilities of FLIPO.

3.3.1 Image quality, zeropoints, and filter profiles

The SOFIA telescope does not have a pre-flight cooling system, so the telescope cools rapidly during the early part of the flight. An algorithm has been developed to estimate the focus position of the secondary mirror as a function of temperature, and the focus is updated by the telescope operator throughout the flight. As discussed in Dunham et al. (2014), shear layer, cavity seeing, telescope jitter, and defocus all contribute to the measured image quality on SOFIA. The measured FWHM of point sources observed on SOFIA is given by:

$$FWHM_{measured} = \sqrt{FWHM^2_{Jitter} + FWHM^2_{ShearLayer} + FWHM^2_{CavitySeeing} + FWHM^2_{Defocus}}.$$

If we assume that the telescope is in focus, this reduces to:

$$FWHM_{measured} = \sqrt{FWHM^2_{Jitter} + FWHM^2_{ShearLayer} + FWHM^2_{CavitySeeing}}.$$

Cavity seeing, like dome seeing at ground based observatories, is created by temperature differentials in the telescope cavity and is assumed to be largest early in the flight when the telescope system is warm. Both shear layer and cavity seeing are wavelength dependent, so HIPO measures larger PSFs than FLITECAM (e.g. Dunham et al. 2014). The best FLITECAM images in the FLIPO configuration had a FWHM of about 6 pixels ($\sim$2.85″), but $\sim$3″was more typical, and there was often a slight elongation in the cross-elevation axis. We can estimate the impact of shear layer and cavity seeing on FLITECAM's PSF size with measurements of the average point source FWHM in FLITECAM images and measurements of the SOFIA telescope jitter. With a measured FWHM of 3.3″ at 3.08 μm (FLITECAM's Ice filter) and a contemporaneous average jitter FWHM[2] of 2.2″ (Eric Becklin, *private communication*), the combined contribution to FLITECAM's 3.08 μm PSF FWHM from shear layer and cavity seeing is 2.4″. It is noteworthy that FLITECAM produced seeing-limited images ($\sim$1.2″) during observations at Lick Observatory, where the PSF size is dominated by atmospheric seeing.

Zeropoint (ZP) magnitudes, defined as the magnitude corresponding to a measured signal of 1 DN/s, were obtained for most of FLITECAM's filters in the 1-4 μm range. Two standard

---

[2] $FWHM_{Jitter} = 2.355 * \sigma$ where sigma is 0.95″ rms.

Table 3.1. FLITECAM 1-2.5 μm Zeropoints

Band	ZP (mag)	Calibration Factor (DN/s/mJy)
J	21.24 ±0.04	183.074
H	20.91 ±0.05	212.974
K	19.96 ±0.06	130.563
Paschen-α	17.50 ±0.09	10.311
Paschen-α cont.	17.46 ±0.08	10.301

stars that have been fully modeled in the near infrared (Cohen et al., 2003) were used for the determination of the zeropoints. The final zeropoint for each band is the weighted mean of the individual measurements, typically five frames per star, using the 2MASS magnitude as a reference. Table 3.1 shows the results for the J, H, and K filters. Also tabulated are zeropoints for the pair of 1% wide ($\Delta\lambda/\lambda$) filters associated with Paschen-α (1.875 μm) and its adjacent continuum at 1.90 μm. An average of the 2MASS H and Ks magnitudes was used as a reference for these special filters. The third column of Table 3.1 gives the conversion factor from measured counts per second (DN/s) to flux density in milli-Jansky.

Combining the zeropoints with background measurements, we can estimate the minimum detectable continuum fluxes (for S/N = 4 in 900 s) for the various filters. The results are sensitive to the image size, and only apply to the FLIPO configuration. For the J, H, and K bands, the limiting fluxes are 20.17, 25.21, and 39.64 μJy. For the Paschen-α filters the value is ~135 μJy. Zeropoints were harder to obtain for the thermal infrared filters. Brighter stars were needed, and detector sub-arrays had to be used to read out the array faster in order to avoid saturation. Nevertheless, our preliminary results for Ice, PAH, and nbL yield the following detection limits in FLIPO configuration: 0.77, 1.5, and 1.4 mJy.

Figure 3.1 shows the transmission profiles for all of the filters commissioned in the FLIPO configuration, including the three 4% wide filters centered at 3.08 μm (Ice), 3.3 μm (PAH),

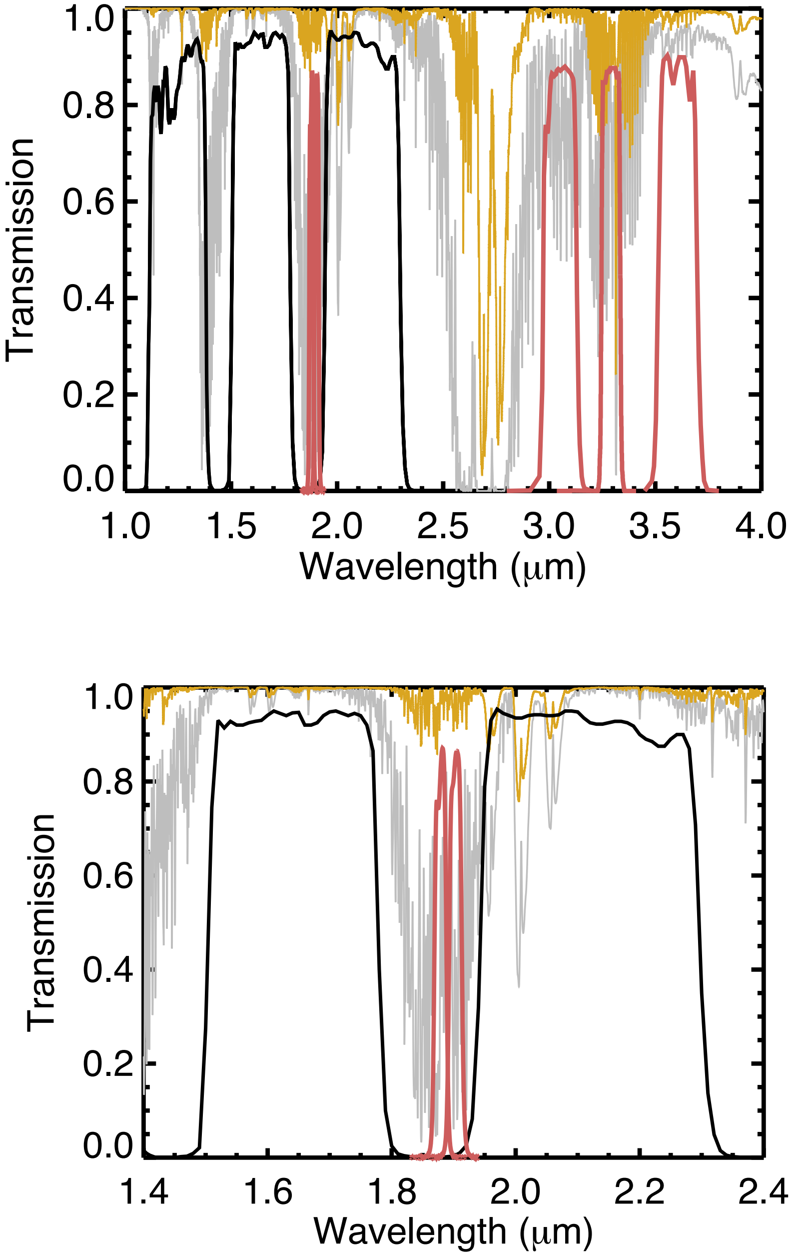

Figure 3.1 Shows the transmission profiles of FLITECAM filters in the 1-4 μm range compared to ATRAN models of atmospheric transmission for Maunakea (14,000 ft; grey) and SOFIA (41,000 ft; yellow). The upper plot includes three broad band filters (JHK; black) and five narrow band filters (in red from L to R: Paschen-α, Paschen-α continuum, 3.08 μm Ice, PAH, and nbL). The lower plot is a close-up of the Paschen-α region clearly showing the advantage of observing Paschen-α from the stratosphere.

and 3.6 μm (nbL). The filter profiles are over-plotted on ATRAN atmospheric models (Lord 1992) to illustrate the difference in water vapor overburden between Maunakea (14,000 ft) and SOFIA (41,000 ft). From the close-up of the region containing Paschen-α, it is clear that this emission line is heavily attenuated by the lower atmosphere for ground-based sites, giving FLITECAM an advantage for studying this otherwise unattainable parameter space. During commissioning, the Paschen-α, and the Paschen-α continuum filters were used for two quite diverse science projects, the study of a star-forming region and the transit of an exoplanet (see below).

3.3.2 Paschen-α and PAH imaging of NGC 2024

To demonstrate FLITECAM's ability to observe wavelengths typically obscured by water vapor at lower altitudes, as well as its ability to perform imaging of extended objects, the FLITECAM team observed NGC 2024, the Flame Nebula, in Orion. NGC 2024 is a well-known nebula with a dense dust lane that obscures many infrared sources. Figure 3.2 shows FLITECAM images of the region around the ionizing source (Bik et al., 2003) IRS 2b, which is partially blended with the brighter IRS 2 source about 5″ away.

The images presented in Figure 3.2 use three narrow filters; the Paschen-α continuum filter at 1.90 μm, the Paschen-α filter at 1.875 μm, and a sub-array field in the 3.3 μm PAH filter. A comparison of the Paschen-α continuum and Paschen-α images clearly illustrates the dramatic distribution of emission from ionized hydrogen. Moreover, a careful examination of the images reveals that the emission from polycyclic aromatic hydrocarbon (PAH) grains is mainly located on the outer edge of the Paschen-α emission region, and is not coincident with the Paschen-α emission (see Figure 3.3). The PAH image is observed in a 512 x 512 sub-array to enable the detector to be read out fast enough to prevent saturation on the background. FLITECAM can be further sub-arrayed to achieve even faster readouts, an advantage of the Aladdin III detector. All sub arrays are fixed around the center of the detector. This initial successful demonstration encouraged us to return to NGC2024 when FLITECAM was commissioned in solo mode. Due to the lower backgrounds at 3 μm in the

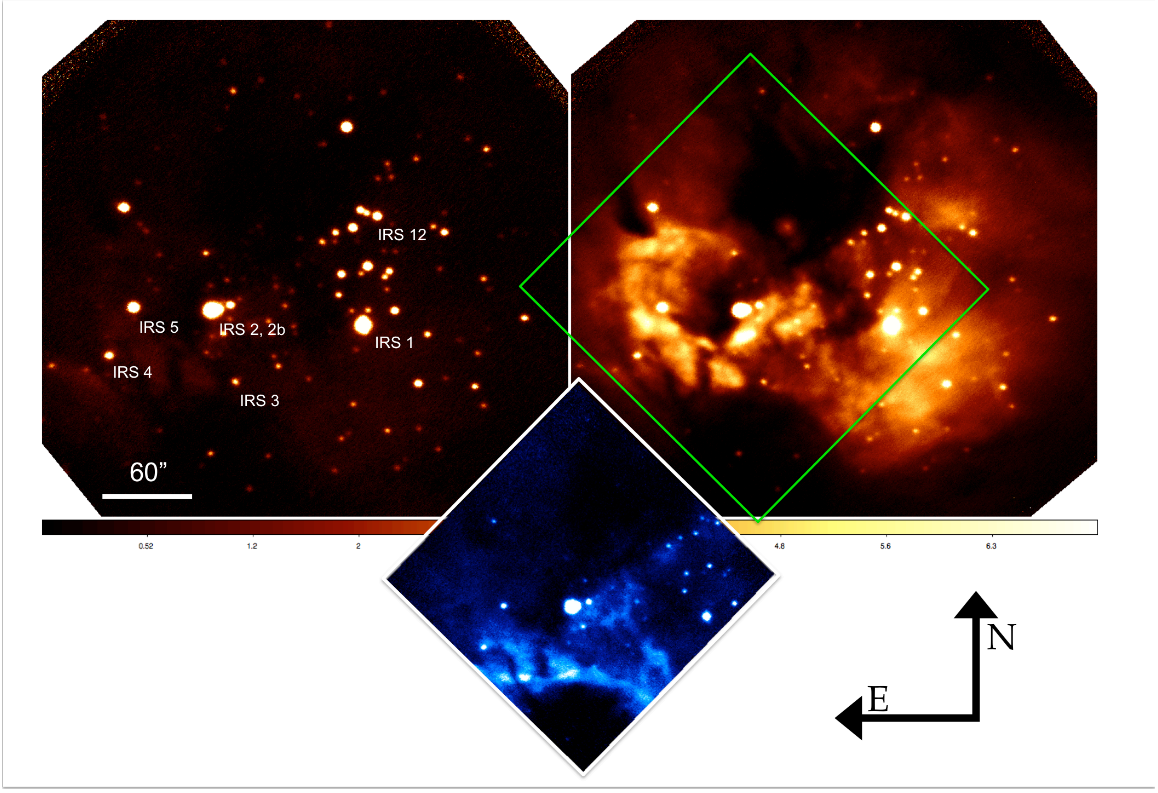

Figure 3.2 Three FLITECAM images of NGC 2024. Upper left: Paschen-α continuum at 1.90 μm; Upper right: Paschen-α emission at 1.875 μm; Below: a 512x512 pixel sub-array field in the 3.3 μm PAH filter. The approximate location of the PAH sub-array field is shown on the Paschen-α image by a green box. Each image was reduced using the FLITECAM imaging pipeline (FDRP).

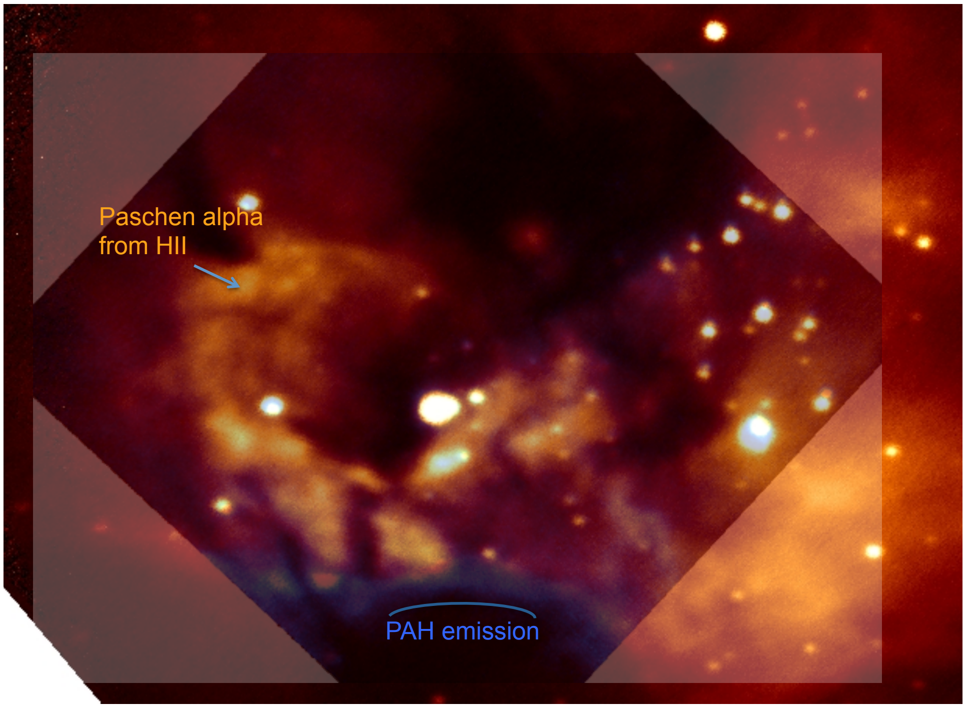

Figure 3.3 An overlay of the FLITECAM Paschen-α (red) and PAH (blue) images for NGC 2024. The PAH emission is physically distinct from the ionized hydrogen gas. All images in this section are displayed with North up and East left.

solo mode, we were able to obtain full frame PAH images. See Chapter 4 for more details on FLITECAM science in the solo configuration.

A note on data reduction: All FLITECAM imaging data presented in this dissertation are reduced using the FLITECAM data reduction pipeline (FDRP). The IDL-based FDRP was originally developed by Ralph Shuping (USRA) in collaboration with Ian McLean for use with FLITECAM data at Lick Observatory, and was significantly updated by Sachindev Shenoy (USRA) and William Vacca (USRA) for use with SOFIA data. FDRP performs the typical bad pixel masking, flat fielding, and background subtraction. Because SOFIA does not have facilities for taking dome flats, a flat field is created from sky frames. For point source observations, the science frames are used to create the sky flat. For extended source, dither-nod-dither observations such as the NGC 2024 observations, off-source sky images are observed for this purpose. Each science image in a dither set is reduced separately and then stacked to create the final science image.

3.3.3 FLITECAM spectral coverage in the FLIPO mode

A major activity for the 2014 commissioning flights was calibration of FLITECAM's nine spectroscopic modes, each of which can be observed with two different resolving powers. Figure 3.4 shows the approximate wavelength ranges of the three KRS-5 grisms, labeled A, B, and C, each of which can be used in three different orders with a matching blocking filter in the first filter wheel. FLITECAM has nearly continuous spectral coverage from 1-5.5 μm.

Though most commissioning spectra were taken using the lower resolution slit, R$\sim$1300, boresight reference points on both slits were established. We demonstrated successfully that we could both nod the star back and forth along the slit (in the typical 'AB' nod pattern) and 'on/off' the slit in instrument coordinates. Because of the increased thermal background in the FLIPO configuration, the longest wavelength regime of Grism A (4.395-5.533 μm) was not commissioned until FLITECAM solo flights (see Chapter 4). Wavelength calibrations are available for all of the other combinations.

3.3.4 Spectroscopy of SN 2014J

During the February 2014 flights, the most significant application of the spectroscopic mode was Director's Discretionary Time observations of the Type Ia supernova in M82 (SN 2014J) on multiple nights. Panel 1 of Figure 3.5 shows members of the FLIPO team as we maneuvered the supernova onto the FLITECAM slit. Panel 2 of Figure 3.5 shows the preliminary accumulated spectra of the supernova as shown in Logsdon et al. (2014). The blue shaded regions in Figure 3.5 indicate parts of the spectra that are very difficult to observe from the ground because of low atmospheric transmission. Note that the strongest emission line, Co II at $\sim$1.77 μm (see discussion in Vacca et al. 2015), is not observable in its entirety from the ground. The FLITECAM SN 2014J results, including spectra in the 2.7-3.5 μm regime not shown here, are presented in Vacca et al. (2015). As discussed in detail in that work, most of the features covered in the FLITECAM/SOFIA spectra of the supernova are well-matched to supernovae models, including the width of the Co II emission feature at $\sim$1.77 μm. A good agreement between the spectrum and the models is significant as Type

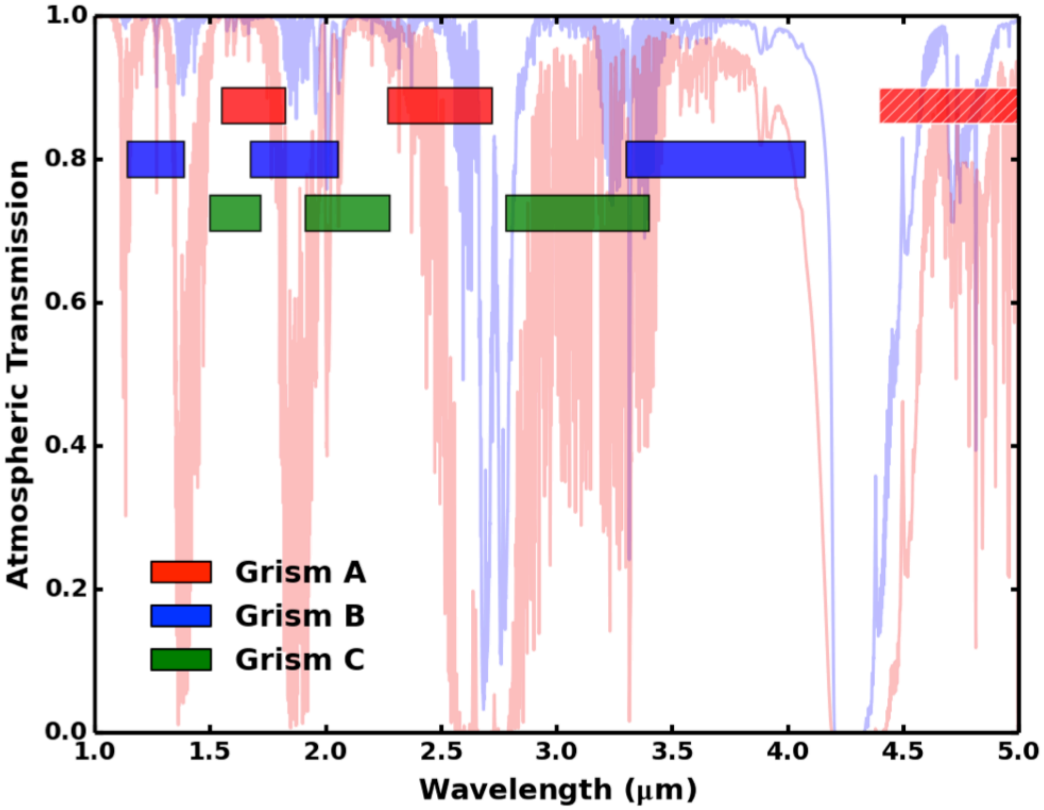

Figure 3.4 From the SOFIA Observer's Handbook (Figure credit: Ryan Hamilton, USRA): Spectral coverage of the three FLITECAM grisms, labeled A (red), B (blue), and C (green). Each grism can be used in three orders by selecting a suitable order-sorting filter from filter wheel #1. For comparison, the ATRAN models of atmospheric transmission are shown for Maunakea (red) and the stratosphere (blue). The longest wavelength regime of Grism A (red hashed rectangle) saturates in the FLIPO configuration and was not commissioned until FLITECAM's first solo configuration flights (see Chapter 4).

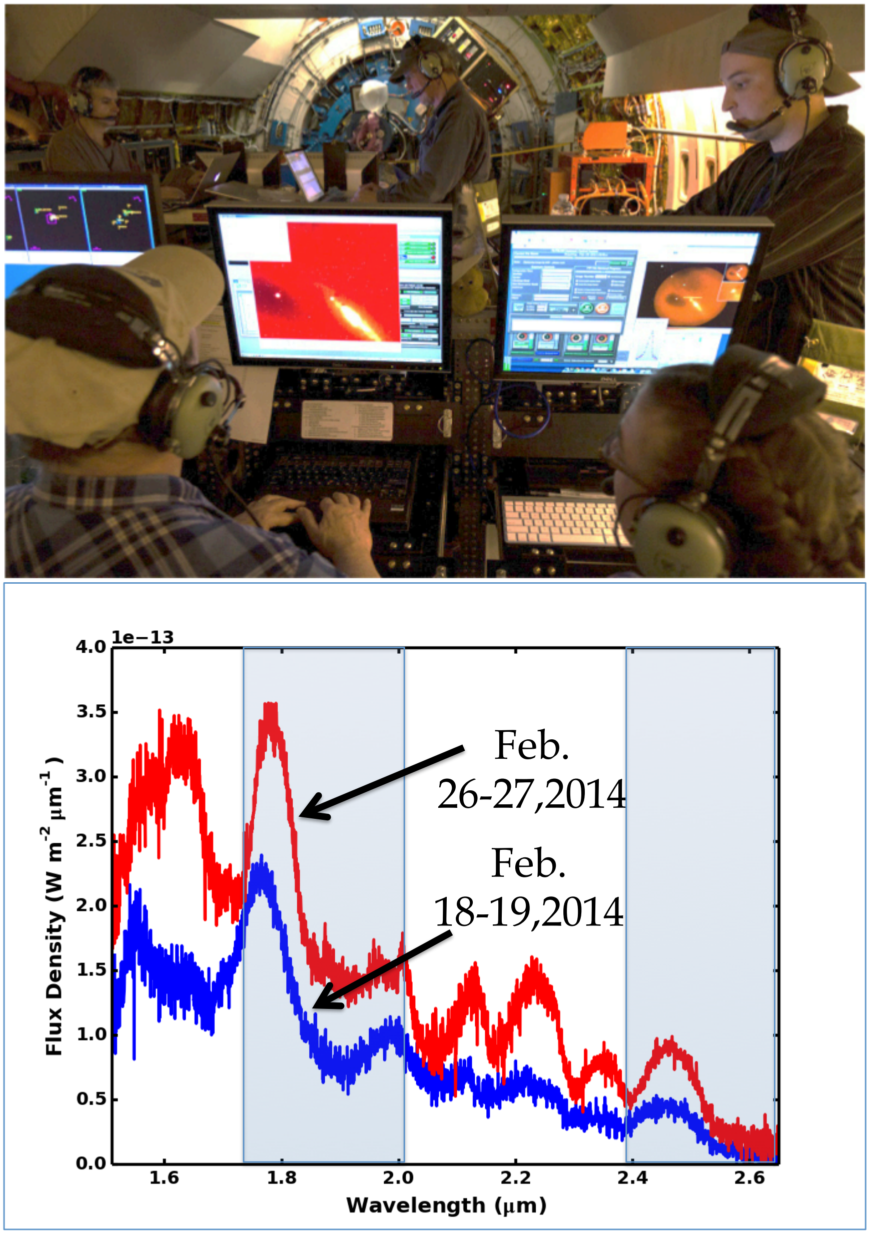

Figure 3.5 Top: The FLIPO team observing SN 2014J. From bottom left: Ian McLean, Georgi Mandushev, Edward (Ted) Dunham, Ryan Hamilton, and Sarah Logsdon. Bottom: Using 5 grism modes (data from 4 grism modes shown) we observed the Type Ia Supernova in M82. The blue shaded regions indicate parts of the spectra that are difficult to observe from the ground because of low atmospheric transmission (Plot credit: Ryan Hamilton, USRA). The full results of the SN 2014J work are presented in Vacca et al. (2015).

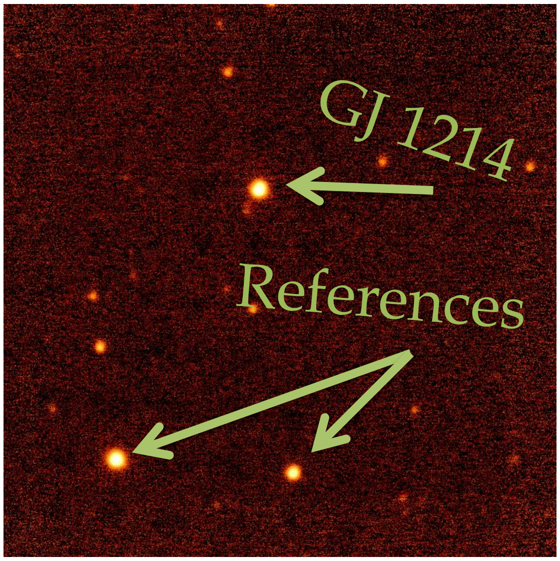

Figure 3.6 Cropped FLITECAM image of the field containing GJ 1214. Observing a transit of GJ 1214b was one of the early science programs for FLIPO. This frame was based on a set of five-point dither images taken on a test flight leg a few days before the actual transit observations. The filter was the 1% wide filter at 1.90 μm.

Ia supernovae light curves are an essential component of the so-called 'cosmic distance ladder,' serving as the primary method for measuring extragalactic distances (see e.g. Riess et al. 1996). However, there are regions of the spectra, particularly in spectra taken ∼44 days after explosion compared to spectra taken ∼36 days after explosion, that deviate from the models. These results highlights FLITECAM's utility for constraining the physics of current supernova models.

3.3.5 Transit photometry of GJ1214b

Simultaneous optical and infrared, high-cadence photometric observations of transits and occultations has become a major science goal of the FLIPO configuration. During the commissioning flights in February 2014 we observed a transit of the exoplanet GJ 1214b. Figure 3.6 shows an image of the field taken with FLITECAM. In concert with HIPO and SOFIA's Focal Plane Imager (FPI+; Wolf et al. 2014; Pfüller et al. 2016), we were able to image a transit simultaneously in four wavelength bands, three optical (two HIPO channels and one FPI channel) and one near-infrared (FLITECAM). The General Investigators (GIs) for this observation, Claudia Dryer and Daniel Angerhausen, were on board.

Using FLITECAM's continuous data-taking mode, frames were recorded every 30s for about 3.5 hours. The infrared band selected for the FLITECAM observations was the narrow Paschen-α continuum filter at 1.90 μm. This wavelength was chosen as a possible diagnostic of water vapor in the exoplanet atmosphere. A quick photometric analysis during flight showed that the transit was detected by all cameras. Characterizing systematics due to the airborne environment (such as changes in Mach number) can impact such observations and special care has been taken to understand and remove these systematics. Another challenge of observing transits with FLIPO is that there is no compensation for field rotation. In the case of GJ1214, we chose to locate the imaging boresight on the exoplanet star so that the target star would remain fixed on the FLITECAM array within the pointing accuracy of SOFIA. However, as the reference stars were not on the boresight, they moved to different pixels as the field rotated. This drift introduces a photometric error unless the flat field is very good and very stable. Because the 1.90 μm filter is very narrow, it was challenging to build up enough signal for a flat field using the sky. We attempted to do this with dithered observations before and after the transit, but imprecise flat-fielding implied larger errors on the FLITECAM data set. The final results of the GJ 1214b observation, including all four light curves, were recently submitted to *Astronomy & Astrophysics* for publication (Angerhausen et al. *submitted*).

3.4 FLIPO's First Deployment: New Zealand, Summer 2015

After commissioning in the FLIPO mode in February 2014, FLITECAM was returned to the UCLA IR Lab and underwent formal acceptance as a Facility Science Instrument (FSI) for SOFIA (see Chapter 2, Section 2.7). After FLITECAM's Physical Configuration Audit in February 2015, the UCLA FLITECAM team's attention turned to preparing for FLITECAM's next SOFIA flights – two flights in the FLIPO configuration on deployment in New Zealand. The goals of these two flights were to prepare for and to observe a Pluto occultation[3] just fifteen days prior to the New Horizons fly by of Pluto. The nearly contemporaneous nature of the occultation and the New Horizons fly-by made observations of the occultation particularly valuable. In principle, by observing this occultation we would be able to calibrate decades of ground based data with the data retrieved from New Horizons. Observing the occultation with FLIPO and the FPI+ at four different wavelengths simultaneously also presented a unique opportunity to test for the presence of haze in Pluto's atmosphere, which is wavelength dependent. The GI for the SOFIA Pluto occultation proposal was Michael J. Person (MIT).

3.4.1 Deployment Preparation

In addition to participating in larger science and logistical team meetings with the entire Pluto occultation team (including SOFIA staff, the GI's science team, the HIPO team, and the FPI+ team), the UCLA FLITECAM team's preparation for the Pluto occultation included hands-on work in both the IR Lab and at the Armstrong Flight Research Center (AFRC) Building 703 (SOFIA's home base). With the support of Ian McLean and Eric Becklin, I was able to take a larger managerial roll over the IR Lab team's Pluto occultation activities. I also had the privilege of serving as the primary FLITECAM Instrument Operator during the Pluto occultation flights.

3.4.1.1 Cadence Tests

IR Lab work to support the occultation began in earnest with instrument cold tests in Spring 2015. One of our primary actions was to investigate the optimal high-cadence observing strategy for FLITECAM. This work was required because of the short duration of the occultation: from ingress to egress, the duration of the Pluto occultation would last for

---

[3] In general, an occultation or transit light curve of an object with no atmosphere, will have a sharp ingress and egress. An occultation or transit light curve of an object with an atmosphere (such as Pluto) will have a gentler ingress and egress as the starlight is refracted through the atmosphere of the occulting/transiting object.

two minutes[4]. In order to get baseline measurements on either side of the transit as well as sufficient coverage of the transit itself, the observing strategy was to take a long (∼30 minutes), continuous sequence of short exposures. After on-sky testing, each individual exposure was set to 1.25 seconds. Until the Pluto occultation, FLITECAM had never been run that quickly for an extended period of time, so stress-testing was needed to understand FLITECAM's behavior in this scenario. We also wanted to test FLITECAM's three data-taking options to determine which was the best to use during the occultation.

In practice, there are three ways to take data with FLITECAM. 1) Standard operation: FLITECAM observations are typically executed from the STARGATE computer, which is an Apple Mac Mini that runs FLITECAM's instrument control software. The instrument control software is a high-level software that communicates with FLITECAM's other two computers (MKIR and FARSCAPE) to run and monitor FLITECAM and also sends commands to the telescope and monitors SOFIA housekeeping. Once an observing sequence is executed in STARGATE, STARGATE sends the data taking parameters (i.e. exposure time, co-adds, etc.) to the detector control computer, MKIR. MKIR is a custom-built computer that communicates directly with the onboard FLITECAM detector electronics via a set of optical fibers. Once an observation is complete, STARGATE retrieves the data as a fits file from MKIR through an FTP socket and then modifies the original MKIR header to add information such as FLITECAM and telescope ephemeris, before storing the data locally. Data stored on STARGATE is therefore complete with all header information present. MKIR also stores a local copy of each fits file. 2) MKIR only: The FLITECAM Instrument Operator can take images directly from MKIR, with the caveat that only detector information (such as integration times, coadds, timestamps, etc.) is included in the header. 3) MKIR Movie Mode: The third data taking option is to operate the detector directly from MKIR using MKIR's specialty 'movie mode' feature. In this mode, images are taken and stored on MKIR's DSP board until the DSP buffer is full. All of the images stored in the DSP buffer are then transferred into a single, 3-dimensional .fits file. Because movie mode

---

[4] To first order, the duration of a Pluto occultation is determined by the size of Pluto and the rate of Earth's orbital motion

only writes to disk when the DSP buffer is full, write overheads are smaller than standard MKIR observations, which writes to disk after each observation. The efficiency of movie mode depends on the number of frames stored in each fits file. However, movie mode had not been tested in flight and concern regarding timestamp accuracy led us to drop this third option from consideration for the Pluto occultation.

Cadence testing in the lab showed that the standard observing mode (using the STARGATE computer) had a fairly substantial overhead per frame (∼3 seconds). Observing directly from MKIR incurred a much shorter overhead of ∼0.55 seconds per frame. After consulting with the rest of the SOFIA Pluto occultation team, including the GI, we decided to observe the occultation from MKIR only, even though it would be lacking some of the header information STARGATE observing would include. Some of the missing header information could be recovered post-flight from the Observatory ephemeris logs. Cadence testing also showed that MKIR's data taking efficiency decreases by a few seconds for every 100 .fits files stored in MKIR's default data directory. Simply moving frames to another directory resolves this issue. To automate the moving process, Chris Johnson created a data archiver cron job that checks for and moves data files from MKIR's default directory to an archive directory after a user specified number of frames.

3.4.2 Packing and Shipping

While on deployment in New Zealand, SOFIA operates out of the US Antarctic Program's base at Christchurch International Airport. Although the base provides facilities from which to run SOFIA's deployment activities, all equipment necessary to operate the SOFIA instruments must be either brought on SOFIA or shipped separately from AFRC Building 703. In order to ensure we had everything we needed to operate FLITECAM successfully in New Zealand, extra care was required to pack FLITECAM's ancillary equipment, including any available spares for FLITECAM's critical components. Each piece of equipment was documented on shipping manifests and photographed prior to packing. In all, we transported five boxes of support equipment and spares as well as a sixth box carrying FLITECAM's

Figure 3.7 Left: The FLITECAM cryostat and handling cart mounted in their custom-built shipping fixture. Note the large isolator springs designed to protect against physical shock to the instrument. Right: The FLITECAM crate moving through the SOFIA hangar to be loaded onto the truck that will deliver it to LAX for shipment to New Zealand.

liquid cryogen fill tubes to New Zealand in addition to the actual instrument components (cryostat, Counterweight rack, and Principal Investigator rack).

Four SOFIA instruments (HIPO, FLITECAM, FORCAST, and GREAT) were scheduled for observing on the 2015 New Zealand deployment. However, only one instrument (with the exception of FLIPO) can be mounted to SOFIA at any given time. Furthermore, SOFIA's hold is only big enough to contain one instrument. The SOFIA project decided to fly SOFIA to New Zealand with FORCAST installed and GREAT in the cargo hold. Thus, FLIPO had to be shipped to New Zealand on a commercial cargo plane. Naturally, we wanted to ensure that FLITECAM arrived in New Zealand in the same condition as it left UCLA. In order to accomplish this goal, special attention was paid to crating the FLITECAM cryostat and counterweight rack (CWR)[5]. Of particular concern during crating was protecting against 1) exposure to weather, 2) electrostatic shock, and 3) physical shock.

To protect against physical shock, the cryostat installed on its handling cart was mounted to a custom-built steel shipping fixture attached to four sets of isolator springs. Because we

---

[5] FLITECAM's Principal Investigator (PI) rack was installed in an extra PI rack mount on SOFIA for transport to New Zealand.

Figure 3.8 Left: The FLITECAM counterweight rack (CWR) undergoing a fit check in its foam-lined crate. Right: The FLITECAM CWR (left) and accessory pallet (right). Here I am investigating the CWR manifest attached to the side of the box.

were not able to fit-check this shipping fixture before FLITECAM packing began, a team of SOFIA personnel, NASA machinists, and IR Lab personnel worked together over several days to refine the original assembly design to precisely fit FLITECAM and to ensure the cryostat was safely packed for shipping. As shown in Figure 3.7, FLITECAM, installed in its shipping fixture, was mounted to a ULD pallet, which formed the base of FLITECAM's shipping crate. The remaining walls and lid were wood. Before the crate walls were erected, FLITECAM's electrical connectors were covered with electrostatic discharge (ESD) caps to prevent electrostatic shock, and covered in vented plastic wrap to limit the amount of moisture reaching the cryostat in case of rain. My role in the cryostat crating process to answer questions about FLITECAM, document and photograph the fixture assembly process, and create a disassembly manual to be used by the team in New Zealand when un-crating FLITECAM. It should also be noted that the CWR was mounted in a custom foam-lined, wooden crate and was covered in vented plastic wrap to prevent water damage (see Figure 3.8).

3.4.3 FLITECAM in the New Zealand Lab

Once HIPO and FLITECAM arrived in New Zealand and were unpacked, they were placed in the Science Instrument (SI) Cache in the US Antarctic Center base. In the SI Cache, FLITECAM was first exercised warm to verify functionality and then pumped out and cooled. Once the instrument reached operating temperatures, we began a series of cold tests. About 20 frames into those cold tests, the detector control computer (MKIR) began to behave erratically. After multiple unsuccessful attempts to bring the system back to normal operating behavior, we became concerned that the cold temperature of the Cache was inducing a cold failure in the MKIR power system. A sensitivity to cold had manifested in the MKIR system before during line ops testing on SOFIA, during a particularly cold flight, and once in the lab when we intentionally cooled the backend of the MKIR computer by setting it close to a portable air-conditioning unit. Previously, we had been able to recover MKIR functionality by heating the MKIR power supply with a heat gun, so we attempted to warm up MKIR in the Cache. This initial warming successfully recovered MKIR for about 50 data frames and then the system failed again. After another set of attempts to reboot MKIR in which the system struggled to come up, worked for several frames and then crashed again, we decided that the unpredictable detector computer was an extreme risk for a time-sensitive occultation to be observed in a cold, New Zealand winter climate.

Fortunately, we had brought a spare detector controller with us to New Zealand. In anticipation of a possible MKIR failure, the SOFIA project was able to acquire an obsolete, but very similar detector control computer in Summer 2014. This control computer was developed by Mauna Kea Infrared, the company who developed MKIR, to run an identical detector (Aladdin III InSb array) in the SpeX instrument (Rayner et al., 2003). The SpeX detector control computer became obsolete when the SpeX team upgraded from an InSb detector to a more modern HgCdTe H2RG detector, but was still completely functional. The IR Lab's System Administrator and FLITECAM team member, Chris Johnson, had set up the SpeX system to be compatible with MKIR's software. We decided to continue our cold testing using the SpeX computer. These tests included FLITECAM functionality checks, FLITECAM and HIPO relative timing tests, and repeated cadence testing. After the successful completion of our cold tests, we officially installed the SpeX chassis in place of the MKIR chassis in FLITECAM's PI rack. The SpeX computer ultimately flew on both flights in New Zealand and has flown on all FLITECAM flights since the New Zealand deployment.

3.4.4 Pluto Occultation: Check Flight and Occultation Flight

Two days prior to the check flight, FLIPO was installed on SOFIA and both the FLITECAM and HIPO teams exercised our instruments to verify continued functionality. We also verified that both instruments were able to interact with SOFIA's Mission Controls and Communication System (MCCS). On UT 28 June 2015, the whole "Pluto occultation team" participated in a ∼5 hour check flight. This check flight had several goals. The main priority was a simulated run of the occultation, with all three instruments (HIPO, FLITECAM, and the FPI+) observing just as they would during the actual observation the next night. In addition to practicing taking a continuous set of high-cadence data, this test also included a set of chopper nod tests designed to verify each instrument's relative timing in order to synchronize each instrument's light curve(s) post-observation. Also on the check flight, the pilot's practiced intercepting an occultation path. Furthermore, the FLITECAM team set FLITECAM's boresight to ensure that the occulting star was in a clean part of FLITECAM's detector, checked instrument focus, and took a few frames of data on the Pluto field. During the check flight, the FLITECAM team noted an intermittent excess background in FLITECAM K band images. This background was significant because it did not subtract well and the K filter was the filter we planned to observe the occultation in. We had seen this intermittent excess background on prior FLIPO flights, but had not had the time or data to characterize it properly. On this flight, however, multiple FLITECAM team members suspected that the K-band background seemed to be elevation dependent. We were not able to explore that theory on the check flight, but we set aside time early on the occultation flight to test the elevation dependency of the background and to determine whether an alternative filter would eliminate this excess background and thus be a better choice for the occultation observation.

The Pluto occultation flight (SOFIA flight #223) took off just after 10:00 hours UT 29 June 2015. After a telescope set-up leg, we spent ∼30 minutes testing FLITECAM's standard H (λ_{eff}=1.63 μm; FWHM=0.28 μm) and K (λ_{eff}=2.10 μm; FWHM=0.40 μm) filters as well as the order-sorting, *Hwide* (λ_{eff}=1.79 μm; FWHM=0.59 μm) filter at several different elevation angles. It was immediately clear that the excess background we had observed in the K band was indeed a function of elevation (see Chapter 4 for more details). The FLITECAM team with input from HIPO PI, Ted Dunham, and Michael Person, decided that the *Hwide* filter was the best filter to observe the occultation in. The *Hwide* filter is less impacted by the excess background than the K band, and provided ∼2-3 times greater signal on the occultation star than the K band data for the same exposure time. Though the H filter provided similar signal to noise as the *Hwide* filter, the redder *Hwide* filter was preferred because it provided the FLIPO occultation observations with a wider wavelength grasp. After the occultation, we also performed elevation tests using the pupil viewing. These pupil viewing tests would turn out to be crucial in informing our understanding of

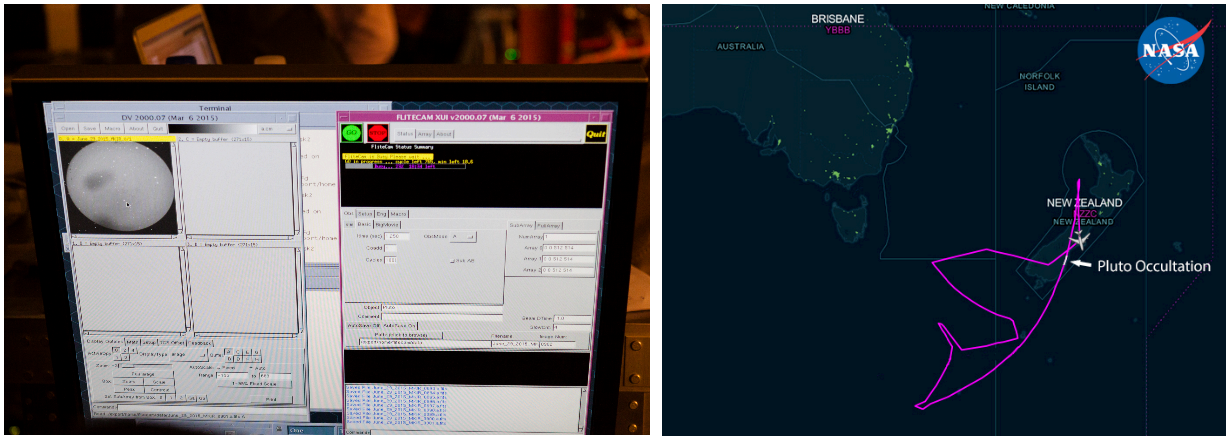

Figure 3.9 Left: Taking data of the Pluto occultation field in FLITECAM's MKIR computer. The cursor in the on-sky image in the upper left is pointing to the soon-to-be occulted star. Right: The as-flown SOFIA flight path for the occultation after an in-flight course correction (Image Credit: NASA/SOFIA/L. Proudfit).

the excess background in K band (again see Chapter 4 for more details). The occultation observation itself went off seamlessly (see Figure 3.9). In flight positioning updates from the Pluto team stationed at Lowell Observatory (led by Amanda Bosh) moved our flight path much further North than the flight plan we took off with. This course correction enabled us to be right in the central flash[6] region of the occultation, right off the coast of New Zealand. All three instruments (four bands) observed the full occultation, including central flash. Ground-based sites such as Mt. John Observatory in New Zealand and several observatories in Austraila were also able to observe either full or partial light curves, but only the SOFIA curves show the central flash at multiple wavelengths. The results of this occultation have been submitted to *Icarus* (Bosh et al. *submitted*).

---

[6] A central flash occurs when the light from the occulted star is focused by the occulting object. In order to observe the central flash, SOFIA needed to be within 75 km of the geometric center line of the occultation (Bosh et al. *submitted*; Olkin et al. 2014).

3.5 Conclusion

Several improvements were made to both FLITECAM hardware and software following the observatory verification flights in October 2011. During six flights in February 2014, FLITECAM was commissioned successfully in the FLIPO configuration. This configuration has FLITECAM co-mounted with the optical instrument, HIPO. In this arrangement there is a warm dichroic beam splitter and a fold mirror in front of the FLITECAM entrance window. The emissivity and increased background made it impractical to commission FLITECAM beyond 4 μm. I have shown that FLITECAM, in the FLIPO configuration, is suitable for narrow band Paschen-α and PAH imaging, which is difficult from the ground, as well as spectroscopy from 1-4 μm. During commissioning, we were fortunate that a target of opportunity occurred during our flight series, supernova SN 2014J. The FLITECAM spectroscopic observations provided data coverage for spectral regions that are not well transmitted to the ground. High cadence photometric observations, such as the GJ 1214b transit and the Pluto occultation, make use of the unique capability of FLIPO and the FPI+ to observe at four wavelengths simultaneously. The Pluto occultation made full use of the SOFIA platform by obtaining more complete observations than were possible at any ground based observatory in the world.

CHAPTER 4

FLITECAM Solo Commissioning

After the Pluto occultation, FLITECAM returned to AFRC Building 703 as an accepted FSI. In August 2015, the IR Lab team delivered the remaining FLITECAM equipment to SOFIA to complete the formal delivery of FLITECAM. FLITECAM then flew on three flights in the solo configuration during Fall 2015. As this flight series was the first for FLITECAM in the solo configuration, these three flights consisted of both commissioning tasks and science observations. Five more solo flights were executed in Fall 2016. This second solo flight series completed solo commissioning and included both Guaranteed Time observations (GTO) and Guest Investigator (GI) science observations. In this chapter, I quantify FLITECAM's relative performance in the FLIPO and solo configurations (Section 4.1) and highlight some key science cases for the solo mode (Section 4.2). I also report on excess backgrounds observed at low elevations in both the solo and FLIPO configurations (Section 4.3). These excess backgrounds have been traced to reflected emission from the outboard engine on the telescope cavity side of the SOFIA aircraft. A baffle installation to mitigate the largest contributor to these reflections was implemented just prior to the October 2016 flights.

4.1 FLIPO and Solo mode in-flight performance comparisons

With data in hand from both FLITECAM's FLIPO and solo configurations, the performances in each mode can be directly compared. Both FLITECAM and FLIPO are mounted at the Nasmyth focus of the telescope. In both cases, FLITECAM is mounted to a flange, which is in turn mounted to SOFIA's Nasmyth tube (again, see Figure 1.3). As briefly discussed in the introduction to Chapter 3 of this work, the fundamental difference between the FLIPO configuration and the solo configuration is that the FLIPO configuration comprises two additional optics: a dichroic beamsplitter and a silver-coated fold mirror. The infrared light from SOFIA's tertiary mirror is reflected off the beamsplitter to the fold mirror and then reflected once more off the mirror and into FLITECAM's entrance window. Unlike the science instruments themselves, which are on the cabin side of the bulkhead that separates the telescope from the rest of the airplane, the FLIPO fore optics are mounted on the telescope end of FLITECAM+HIPO flange (i.e. inside the SOFIA Nasmyth tube). The Nasmyth tube is exposed to the stratosphere. However, there is little air circulation towards the rear of the Nasmyth tube, meaning that the fore optics are warm (near cabin temperature) during flight. The additional fore optics lead to increased backgrounds for FLITECAM in the FLIPO configuration, particularly at wavelengths > 2 μm. These increased backgrounds are quantified in the sub-sections below. As evidenced by the science results presented in Chapter 3, FLITECAM in the FLIPO configuration is still able to provide good science and employs all of its observing modes, both imaging and spectroscopy, from $\sim$1-4 μm.

4.1.1 Relative Imaging Sensitivities

In order to quantify FLITECAM's relative backgrounds in the FLIPO and solo configurations, I measured the median background value of individual raw, on-sky data frames in counts per second per arcsecond^2 (DN/s/$''^2$). The final value reported for each filter in Table 4.1 is the average value of the measurements of the individual frames in that filter. As FLITECAM's detector is an engineering grade device, it does have patches of lower quantum efficiency (QE). To make our measurements, I chose a portion of the detector near the center of the array and away from low QE areas. We only include data observed at elevations ≥ 44 ° to minimize the impact of excess backgrounds discovered when observing at low telescope elevations (see Section 4.3 for explanation). Table 4.1 lists the background values for four of FLITECAM's specialty, narrowband filters: Paschen-α, Paschen-α Continuum, Ice, and PAH. This table is based on the first three flights in the solo configuration. Data in some of FLITECAM's other imaging bands from those first flights are limited and thus they are

Table 4.1. FLITECAM vs FLIPO Narrowband Imaging Sensitivities

Band	FLIPO [a] (DN/s/sq. ″)	Solo [a] (DN/s/sq. ″)	Relative Sensitivity Improvement (Solo Configuration)
Paschen-α	61	41	~22%
Paschen-α cont.	51	35	~21%
Ice (3.08 μm)	26,000	1540	~310%
PAH (3.3 μm)	35,400	3260	~230%

[a] Average background values for four of FLITECAM's narrow-band imaging filters in both the FLIPO and solo configurations. All data included in the above measurements were observed at telescope elevations from 44°-53° and SOFIA primary mirror temperatures of -23° to -32° Celsius. The backgrounds are significantly improved in the solo mode when compared to the FLIPO mode at 3 μm.

not included here. The third column in Table 4.1 lists the relative sensitivity improvement for FLITECAM imaging data observed in the solo configuration as compared to the FLIPO configuration. Due to the high reflectivity of the fore optics (see Dunham et al. 2014), signal improvements in the solo mode are small compared to the reduction in background at longer wavelengths and are not included in our sensitivity improvement measurements. This improvement measure is defined as $100 * (\sqrt{(FLIPObackground)}/\sqrt{(solobackground)} - 1)$. While the backgrounds are slightly lower in the solo mode at Paschen-α, and Paschen-α Continuum, there is a significant reduction in sky background in the longer wavelength Ice and PAH filters.

4.1.2 Relative Spectral Sensitivities

In a similar manner to Section 4.1.1, I also characterize the background sensitivity of FLITECAM's four longest wavelength grism spectroscopy modes (~2.27-5.5 μm; Table 4.1.2). I focus my analysis on spectra obtained using the wider ~2″ half (R~1300) of FLITECAM's slit. In order to characterize the background as a function of wavelength in our spectra, I have taken the median value of the background (DN/s/$''^2$) in each half of each spectrum. In other words, for each data frame I make two measurements, one at the shorter wavelengths and one at the longer ones. I then calculate the average background value of the short and long wavelength data in all frames for each grism mode and instrument configuration. The longest wavelength spectroscopy mode (~4.4-5.5 μm) is saturated in the shortest exposure time in the FLIPO configuration; only solo configuration data exists at these wavelengths. The third column of Table 4.1.2 lists the relative sensitivity improvement as described in Section 4.1.1. For grism modes that can be observed by both instrument configurations, there is relatively little sensitivity loss in the FLIPO configuration. This is likely due to the fact that the slit mechanism is located just behind FLITECAM's entrance window and, once inserted into the beam, blocks almost all of the incident radiation except along the slit itself (see Figure 2 in Smith and McLean 2006).

Table 4.2. FLITECAM vs FLIPO Long Wavelength Spectroscopic Sensitivities

Band (Grism Mode)	FLIPO [a] (DN/s/sq. ″)	Solo [a] (DN/s/sq. ″)	Relative Sensitivity Improvement (Solo Configuration)
2.270-2.722	14	14	∼0%
(KlA)	66	58	∼7%
2.779-3.399	1150	990	∼8%
(LMC)	1660	1240	∼12%
3.303-4.074	2770	2110	∼15%
(LMB)	8490	6630	∼13%
4.395-5.533	N/A	19800	Only usable in solo mode
(LMA)	N/A	37800	Only usable in solo mode

[a] Average background values for FLITECAM's four longest-wavelength grism spectroscopy modes in both the FLIPO and solo configurations. Note that the longest wavelengths are not observable in the FLIPO configuration as the background saturates at the lowest exposure times. All data included in the above measurements were observed at telescope elevations from 39.5°-51° and SOFIA primary mirror temperatures of -25° to -30° Celsius.

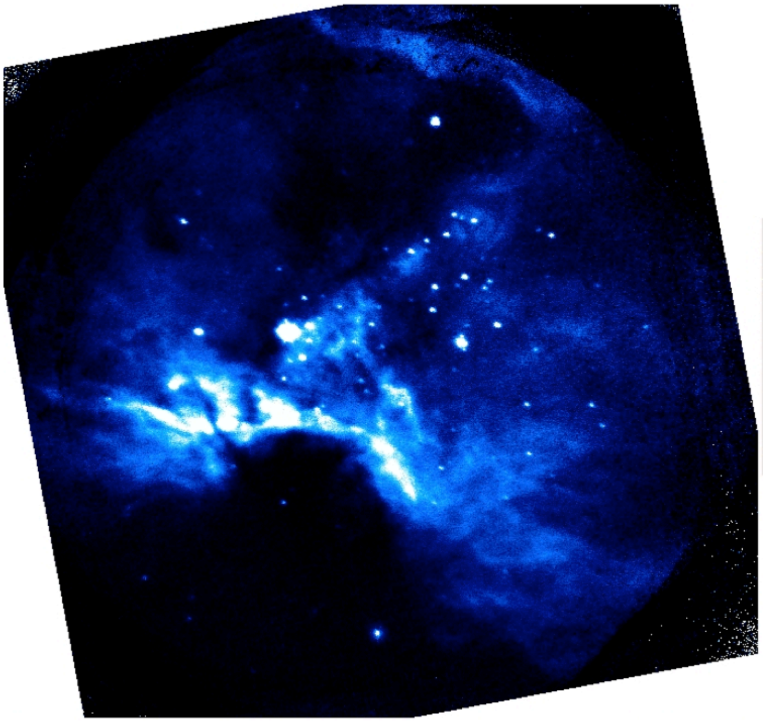

Figure 4.1 A 150s mosaic image of NGC 2024 in FLITECAM's 3.3 μm PAH filter. The data were reduced with the FLITECAM imaging pipeline, developed at the SOFIA Science Center. FLITECAM in the solo configuration allows full-frame observations in the PAH and narrow-band L filters.

4.2 FLITECAM Solo mode example science cases

As described in Chapter 3, the advantage of the FLIPO configuration is that it can provide contemporaneous sky coverage in three wavelength bands – two optical bands with HIPO and a near-infrared band with FLITECAM. This multi-wavelength coverage has proved particularly useful for observations of objects such as exoplanets (Angerhausen et al., 2014, 2015, *submitted*) and solar system objects (Bosh et al. *submitted*) where the science goal is to disentangle wavelength-dependent atmospheric properties. Solo configuration offers increased sensitivity in both long-wavelength imaging and spectroscopy.

4.2.1 Imaging

During FLITECAM's first three solo configuration flights in 2015, FLITECAM observed in its standard JHK imaging filters as well as Paschen-α, Paschen-α Continuum, 3.08 μm Ice, PAH, and narrow-band L (3.6 μm). The lower backgrounds in the solo mode enabled us to obtain full frame (1024x1024 pixels or $8'$) dithered images[1] in PAH (see Figure 4.1), which were observed in 512x512 sub-arrays in the FLIPO mode to avoid saturating the detector. Full frame images were also obtained in the narrow-band L filter, even at low telescope elevations where the background is higher (see Section 4.4). Thus, FLITECAM's solo configuration increases FLITECAM's observing efficiency and effective field of view from 3-4 μm. FLITECAM's broad-band imaging filters at wavelengths longer than 3 μm and the 4.6 μm narrow-band M filter were not tested in flight until the October 2016 solo flight series. During those 2016 flights, the FLITECAM team successfully observed in FLITECAM's L (λ_{eff} = 3.53 μm), L' (λ_{eff} = 3.86 μm), and narrow-band M filters, though sub-arrays were required. A 256x256 subarray was used for the L and L' observations, and a 128x128 subarray was used for the narrow-band M filter.

4.2.1.1 Star-forming science with FLITECAM

As discussed in Section 1.4, FLITECAM on SOFIA is a unique platform for observing Paschen-α and PAH, which are incredibly difficult to observe from even the best ground-based sites (see Figure 3.1), but can potentially provide valuable insight into the evolution of young, high-mass star-forming regions. Early FLITECAM imaging science from the FLIPO commissioning flights included dithered Paschen-α and PAH observations of NGC 2024, a star-forming region in the Orion complex (distance = 363 pc; Brown et al. 1994). However,

---

[1] For the extended, star-forming regions presented in this dissertation, the data were all observed in "dither-nod-dither" mode. This mode is available as part of FLITECAM's Automated Observing Request (AOR) software. A dither-nod-dither AOR 1) executes a user-specified dither pattern on the science target field, 2) moves the telescope to a user-specified sky position, 3) executes the same dither pattern on the sky field, and 4) then returns the telescope to the science field. The dithered sky data are ultimately used to create a sky flat during the data reduction process. All data presented here were reduced with the FLITECAM imaging pipeline, developed at the SOFIA Science Center. See Section 3.3.2 for more details on data reduction.

the FLIPO mode PAH observations were restricted to a 512x512 subarray, so we were only able to observe a portion of the NGC 2024 field in PAH (see Figure 3.2). We revisited the NGC 2024 field during the solo flights and successfully obtained full-frame PAH imaging, as well as 3.08 μm (Ice) and 3.6 μm (bbl) continuum images.

During both the 2015 and 2016 solo flights, we observed the W3 star forming region, which is part of the W3/W4/W5 molecular complex. W3 is located at a distance of 1.95 $\pm$ 0.04 kpc ($\sim$6000 ly) in the Perseus arm of the Milky Way (Xu et al., 2006). During the 2015 flights, we focused our observations on the main ionizing sources in the W3 region. Zooming in on the W3A region (see Figure 4.2), the PAH image shows a strong arc of emission. At the distance of W3, the radius of this arc 0.58 ly. We also see strong Paschen-α emission in W3 main, particularly in W3A. An examination of the final, coadded Paschen-α image from the 2015 flights showed extended Paschen-α at the southwest corner of the FLITECAM field. Thus, during the 2016 flights, we returned to W3 and imaged southwest of our original pointing to further investigate the extended Paschen-α emission. Figure 4.3 shows a composite of the Paschen-α images at both pointings. The extended Paschen-α emission forms a circular loop, which includes some filamentary structure (again see Figure 4.3). There is a star near the center of the circular loop. Further analysis of the NGC 2024 and W3 observations is on-going and planned for summer 2017; see Chapter 6 for discussion of future work.

4.2.2 Grism Spectroscopy

As FLITECAM was originally commissioned at a ground-based observatory, a direct comparison between FLITECAM's performance on the ground and in the stratosphere can be made. We obtained $\sim$3 μm spectroscopy for the planetary nebula NGC 7027 in three FLITECAM configurations: solo configuration using the Shane telescope at Lick Observatory (Smith and Mclean 2008, 2006), FLIPO configuration on SOFIA (McLean et al., 2012), and solo configuration on SOFIA. A comparison between the spectra taken in FLITECAM solo mode from both Lick and SOFIA is shown in Figure 4.4. The Lick spectrum (Smith and McLean 2008)

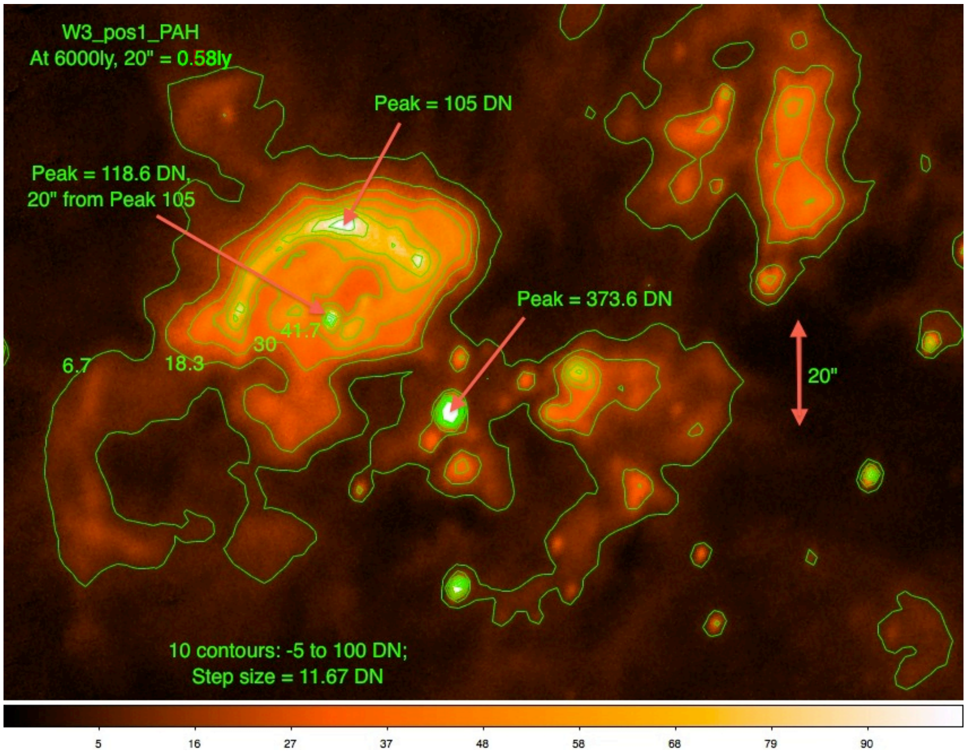

Figure 4.2 FLITECAM PAH image zoomed in to the W3A region to better illustrate the sharp arc of emission from polycyclic aromatic hydrocarbon grains. The image is overlaid with contours. The peak flux in the PAH arc in this exposure is 105 DN). W3 is estimated to be 1.95 kpc ($\sim$6,000 ly) away, which implies that the scale of the arc (radius) is $\sim 20''$ or about 0.2 pc (0.58 ly).

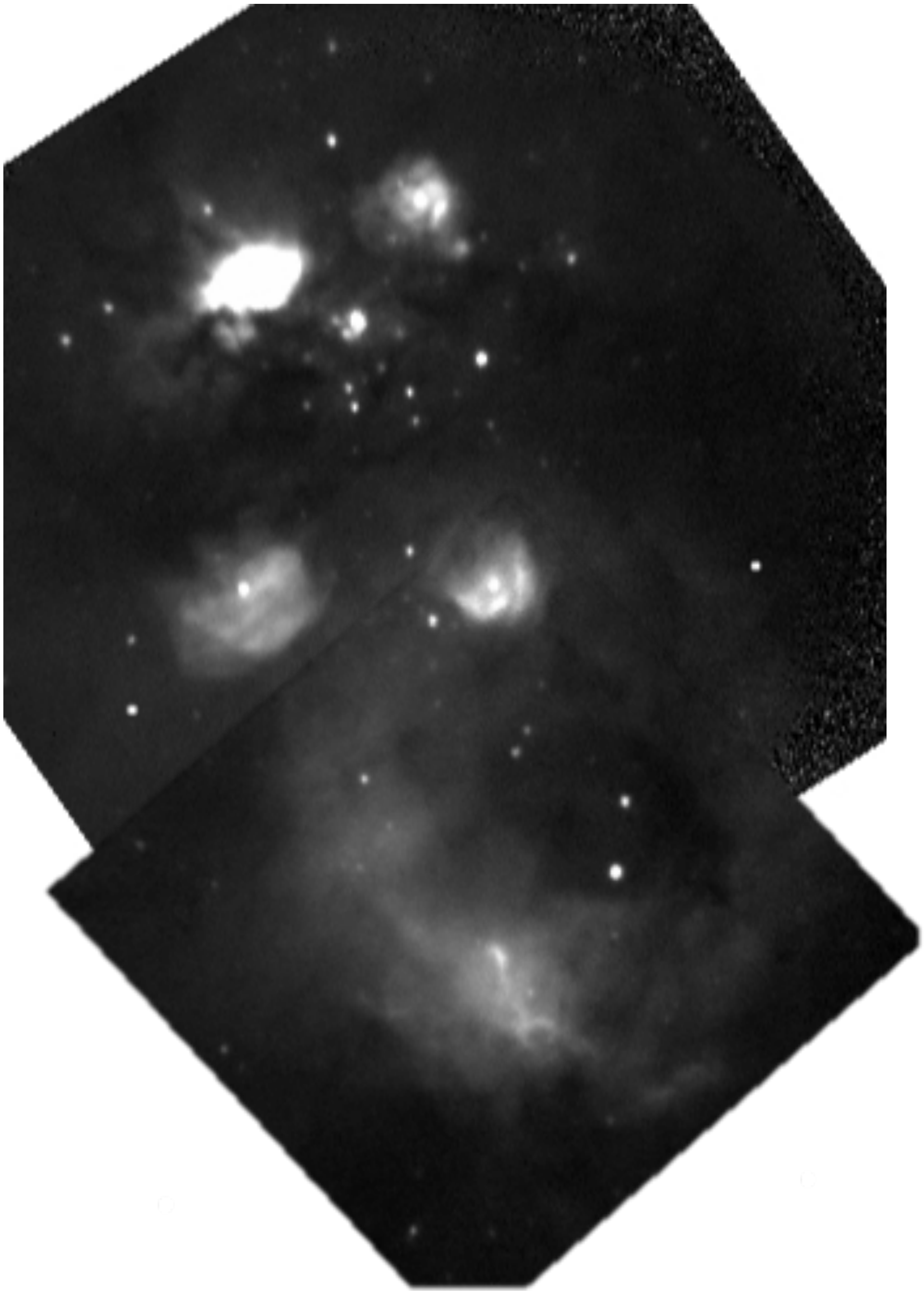

Figure 4.3 The W3 region observed in two FLITECAM pointings using the Paschen-α filter. The first pointing (top image) includes the W3A region shown in Figure 4.2 in the upper left. The second pointing shows an extended loop of Paschen-α to the southwest (The image orientation is North up, East left).

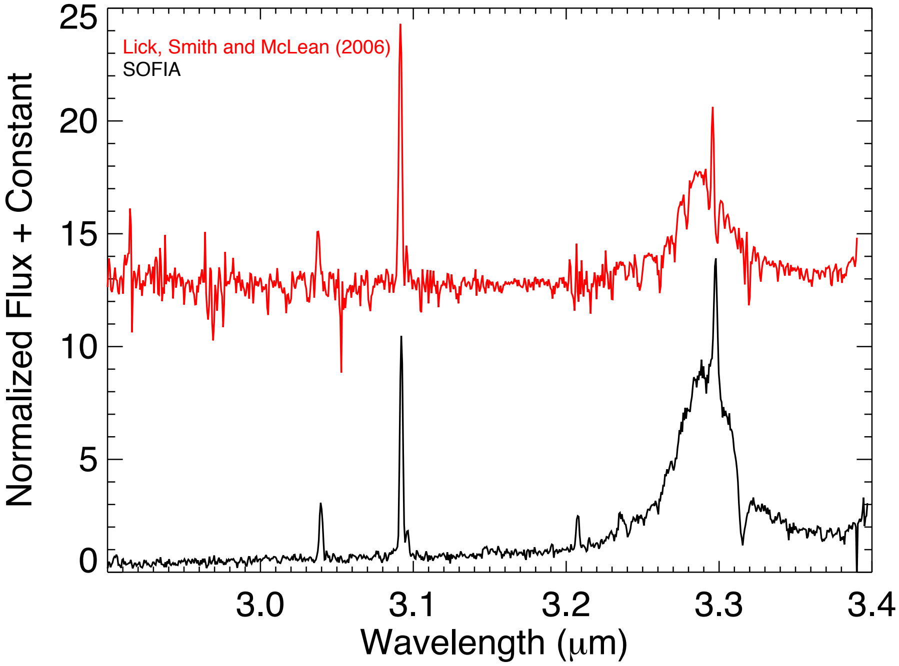

Figure 4.4 NGC 7027 spectroscopy observed with FLITECAM solo configuration at Lick Observatory (red; Smith & McLean 2006) and FLITECAM solo configuration on SOFIA (black; Logsdon et al. 2016). The Lick spectrum is offset in the y-axis for clarity. As noted in Smith & McLean (2006), the absorption lines in the Lick spectrum are residual atmospheric water lines.

was reduced using a modified version of the REDSPEC pipeline (McLean et al., 2003) and has been telluric corrected using a standard star (see Smith and McLean 2008 for further analysis of the Lick data using ATRAN (Lord 1992) atmospheric modeling). The SOFIA spectrum was reduced using fspextool, a modified version of the Spextool pipeline (Cushing et al., 2004), and has not been telluric corrected. Both FLITECAM configurations on SOFIA see a significant reduction in atmospheric water vapor at these wavelengths compared to the ground based data. While all grism spectroscopy modes except the longest wavelength mode (∼4.4-5.5 μm) were tested at Lick, the Shane telescope is much warmer than the SOFIA telescope and observing beyond 3.4 μm at Lick is an extreme challenge. Even with added fore optics, the FLIPO configuration on SOFIA is capable of grism observations out to 4.07 μm, allowing observations of Brackett-α. The solo configuration on SOFIA extends FLITECAM's spectroscopic range out further still to 5.5 μm[2] (see Figure 4.5).

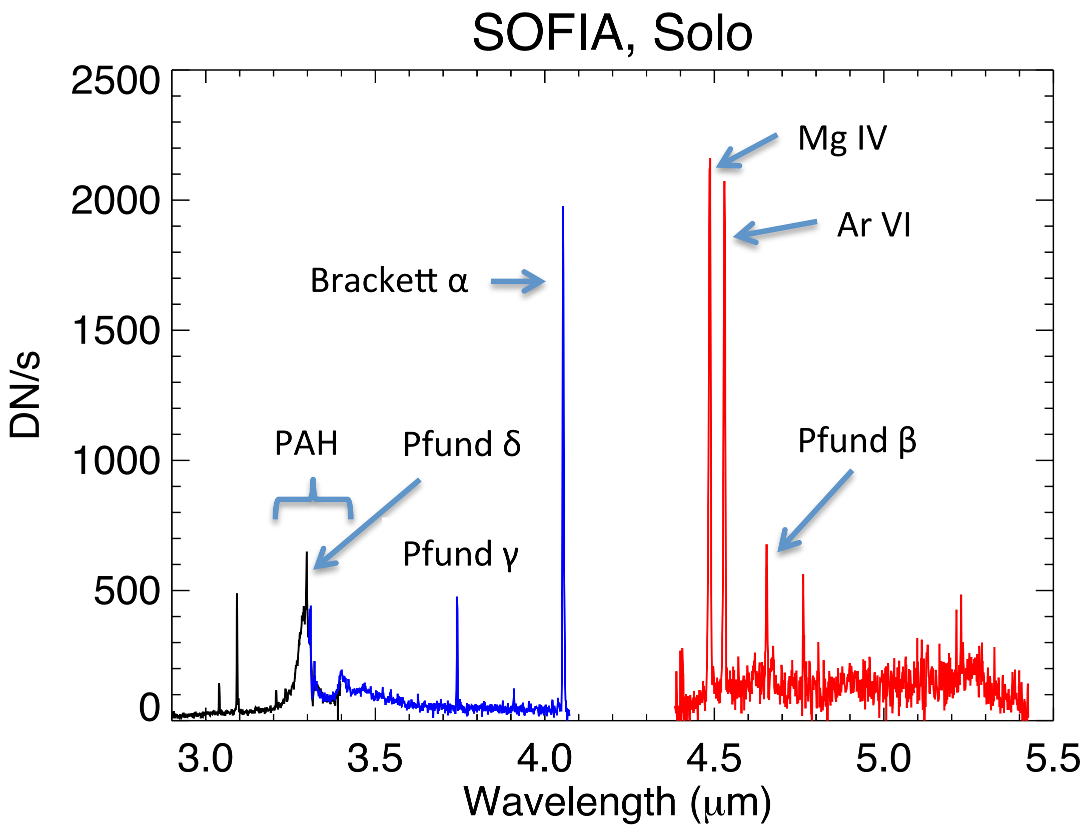

Figure 4.5 NGC 7027 spectroscopy observed with the FLITECAM solo configuration on SOFIA. The three colors indicate the three grism modes used to observe the spectrum. Key emission features are labeled. The additional spectral coverage in solo configuration reveals many strong, atomic emission lines at longer wavelengths.

---

[2] The first 4.4-5.5 μm spectra of NGC 7027 were observed on the Kuiper Airborne Observatory, SOFIA's predecessor, at R $\leq$ 120 (Russell et al., 1977; Bregman et al., 1983). Our FLITECAM spectrum may be the first medium-resolution spectrum of NGC 7027 at these wavelengths.

4.3 Elevation Dependent Backgrounds: Discovery and Mitigation[3]

During FLIPO commissioning in February 2014, the FLITECAM team noticed a non-uniform excess background at low elevations seen most easily at K band (2.1 μm). Other commissioning and science tasks prevented a detailed study of the effect during commissioning. The issue was again noticed during a practice flight for the Pluto occultation, which took place one day before the occultation near the south island of New Zealand. This time, the extra background significantly affected the K band signal to noise at the elevation of the expected position of the occultation. A team member noticed that the excess background changed as the wings tipped in elevation. Figure 4.6 shows the results of the in-flight focal plane test to measure the median background counts of three of FLITECAM's imaging filters as a function of telescope elevation. This focal plane test was observed in the same filters and at the same telescope elevations as described below for the PV data. Because the telescope is fixed in inertial space the source of the background must be fixed to the aircraft.

After a successful observation of the occultation, but before the airplane lost altitude, the FLITECAM team engaged FLITECAM's pupil viewing (PV) mode in an attempt to determine the source(s) of the excess background emission. PV mode tests had been attempted during observatory verification flights in 2011, but an electronic fault prevented full characterization of the PV images obtained from those flights (see McLean et al., 2012 for details). On the occultation flight, we acquired PV images in FLITECAM's Hwide, and K band filters stepping in elevation from 20° to 50° in increments of 5°. The Hwide filter (λ_c = 1.79 μm; FWHM = 0.52 μm) is a non-standard, broad band, order-sorting filter designed for use with FLITECAM's girsms. Three of the K band PV images are shown in Figure 4.7. Standard H band (λ_c = 1.63 μm; FWHM = 0.28 μm) PV images were also obtained over the same elevation range, but in increments of 10° due to time constraints during flight and to match the focal plane images taken the previous night (see Figure 4.6).

---

[3] The analysis and mitigation of the excess background emission measured on the Pluto occultation flight was led by members of the SOFIA team (Eric Becklin, Ryan Hamilton, William (Bill) Vacca, and Patrick Waddell).

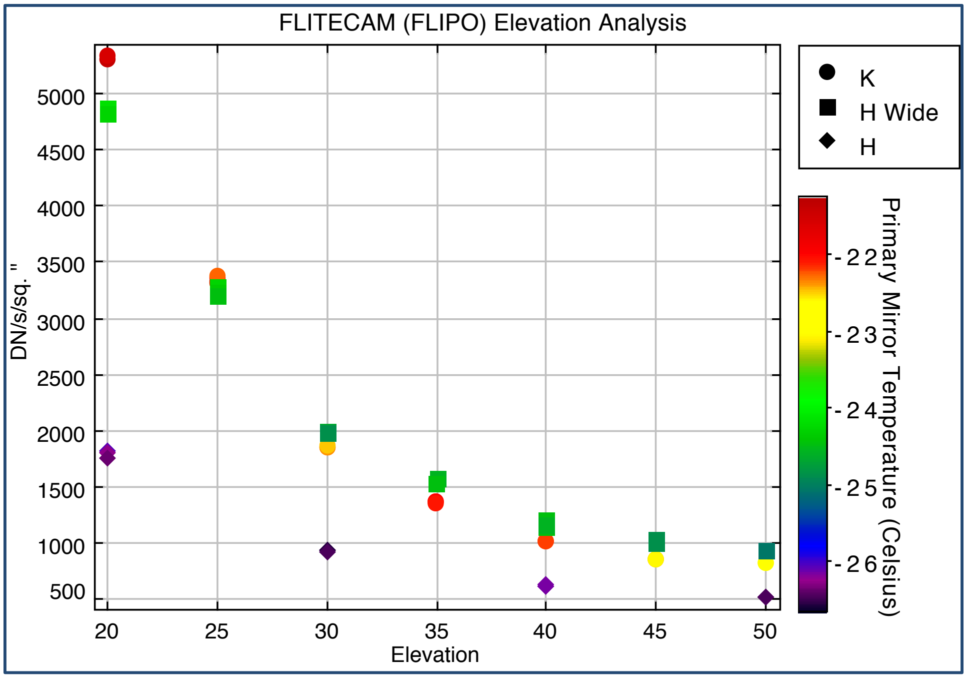

Figure 4.6 Data taken from focal plane images showing median counts per second per arcsecond^2 (DN/s/$''^2$) as a function of telescope elevation. Data were observed in FLITECAM's H (blue diamonds; 1.6 μm), *Hwide* (green squares; 1.8 μm), and K (red circles; 2.1 μm) band filters during a practice flight for the Pluto occultation. There is a significant increase in background at low elevations, particularly at longer wavelengths.

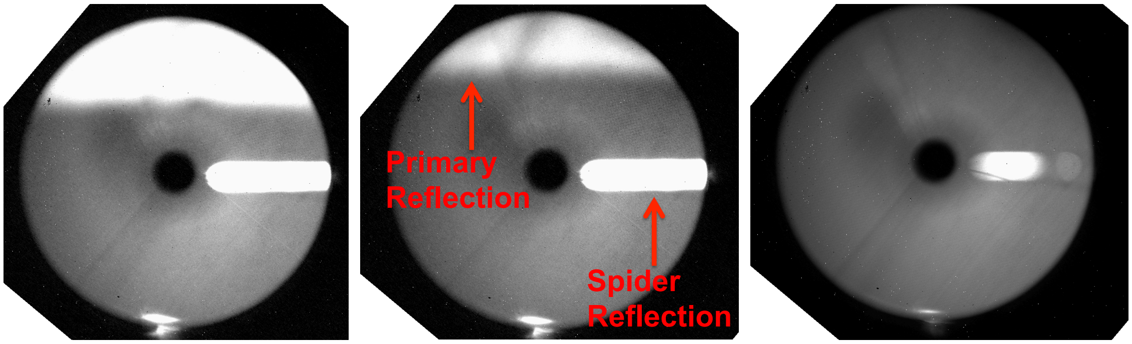

Figure 4.7 (From Left to Right) K band pupil viewing images taken at 20°, 25°, and 40° elevation showing engine emission reflecting off SOFIA's primary mirror and aft spider. The spider reflection is the brightest region in pupil images above ~20°.

At the lowest elevations (20° and 25°), the excess emission is reflecting off two surfaces – directly off the primary mirror and off the aft spider (one of three spiders supporting the SOFIA's secondary mirror). The low-elevation reflections off the primary were predicted in a stray light analysis by Breault Research Organization during SOFIA's design phase in the late 1990s, but the aft spider reflections came as a surprise. Except at the very lowest elevations, where the reflections from the primary and the spider are roughly equal in intensity, the reflected emission off of the spider is by far the dominant component of the observed excess emission. Indeed, the primary mirror reflections fall off rapidly and are only visible in our 20-25° data, whereas the spider reflections persist through 40° elevation. Measurements of the FLITECAM data at 1.6, 1.8 and 2.1 μm show that the emission reflected from the spider is about 700K. This temperature is approximately the temperature expected from emission from the hot cone in the flow of the engines (Dinger et al., 1992). Engine plume emission may also be present, but has not been detected to date. Plume emission is primarily line emission, and also has a similar temperature (Dinger et al., 1992). The amount of emission seen at 1.6 μm at an elevation of 30°, averaged over the primary is similar to the emission seen in the OH airglow originating in the upper atmosphere.

How is the engine emission being reflected off the aft spider and into the beam? The three secondary mirror support spiders are made of carbon fiber. The lower edges of each spider (the edge facing the primary mirror) have been sanded round and left uncovered, making these edges relatively good reflectors in the infrared. FLITECAM/SOFIA team members Eric Becklin and Bill Vacca both calculated the expected reflection radiation from the engine cone, to show that within an order of magnitude, the amount of emission observed by FLITECAM is consistent with the emission expected. The original spider design plan was to put either black or reflective baffles over the bottom of the secondary spiders. This effort was lost when the program was cancelled in 2006. With the discovery of the aft spider reflection, the SOFIA program decided to place IR black baffles, designed by Patrick Waddell, on the bottom of all 3 spider vanes, to eliminate this reflected engine emission. The new baffles are painted with a new stray light coating developed for SOFIA, called J-black (Waddell and Black 2016), and were installed prior to the FLITECAM observations in Fall

2016. While the new spider baffles did indeed eliminate the aft spider reflection, FLITECAM pupil viewing images from the October 2016 flights showed another low-elevation reflection. Further investigation of this reflection is being undertaken by Eric Becklin, Bill Vacca, and Patrick Waddell[4].

4.4 Conclusions

Since FLIPO commissioning in 2014, FLITECAM has been accepted and delivered to SOFIA as a facility class science instrument. It is now maintained and operated by the Observatory. Three FLITECAM solo commissioning and science flights occurred in Fall 2015, which allowed us to directly compare FLITECAM's imaging and grism performance in the FLIPO and solo configurations for the first time. Additional fore optics in the FLIPO mode lead to increased backgrounds when compared to the solo configuration, particularly in FLITECAM's long wavelength imaging modes ($> 2\ \mu$m) and longest wavelength grism mode, which is unobservable in the FLIPO configuration. However, even with increased backgrounds, FLITECAM in the FLIPO mode is still suitable for full-frame imaging out to 3 μm, subarrayed imaging out to 4 μm, and grism spectroscopy out to 4 μm as shown in Chapter 3 of this work. The FLIPO mode is ideal for science cases where simultaneous multi-wavelength coverage can inform physical parameters, such as occultations and transits, as illustrated in the successful observation of the June 2015 Pluto Occultation. The solo configuration extends FLITECAM's full frame imaging capabilities out to 4.6 μm and its grism spectroscopy capabilities out to 5.5 μm. FLITECAM solo mode, example science cases discussed here included medium and narrow-band imaging of the NGC 2024 and W3 forming regions, and spectroscopy of NGC 7027. In both configurations, FLITECAM on SOFIA enables observations of wavelength regions that are challenging to observe from the ground. Finally, excess background emission at low elevations was discovered during early FLITECAM commissioning. This emission was traced to the outboard engine on the telescope side of the aircraft.

---

[4] A discussion of the SOFIA cavity's stray light performance, including the FLITECAM results prior to the spider baffle install, can also be found in Waddell et al. (2016).

The engine emission is reflected off both the primary mirror itself and the aft spider supporting the secondary mirror. The spider reflections are the dominant contributor to the excess background at all but the lowest elevations. A baffle installation in 2016 mitigated spider reflections, but a secondary reflection was discovered.

CHAPTER 5

Probing Late T dwarf $J-H$ Color Outliers for Signs of Age

5.1 Introduction

Like stars, brown dwarfs are classified into spectral types (M, L, T, and Y) based on changes in their observed spectral morphologies. These changes are predominantly, but not exclusively, driven by changes in temperature, with the M dwarf class comprising both low-mass stars and the warmest brown dwarfs ($T_{eff} \gtrsim 2500$ K) and the T and Y dwarf classes comprising the coldest brown dwarfs ($T_{eff} \lesssim 1400$ K; e.g. Kirkpatrick 2005; Cushing et al. 2011). Unlike main-sequence stars, brown dwarfs are not massive enough to maintain stable hydrogen fusion in their cores. This lack of a sustainable energy source means that brown dwarfs continuously cool as they age, creating a degeneracy between luminosity (temperature), mass, and age. Thus independently determining the mass and/or age of individual field brown dwarfs has long presented a challenge to observers. Brown dwarfs whose mass and/or age can be independently determined are so-called "benchmark" brown dwarfs (e.g. Pinfield et al. 2006; Liu et al. 2008). Brown dwarf companions in assumed coeval systems where the age and metallicity of the primary star are well-constrained and the mass of the brown dwarf can be dynamically measured are ideal benchmarks, but such systems are rare (e.g. Dupuy et al. 2009; Crepp et al. 2012).

For single field objects, inferred properties from kinematics (e.g. Dahn et al. 2002; Vrba et al. 2004; Schmidt et al. 2007; Faherty et al. 2009; Dupuy & Liu 2012), and age-diagnostic spectral signatures of gravity (e.g. McGovern et al. 2004; Allers & Liu 2013; Martin et al. 2017) and metallicity can help differentiate ages. The surface gravity of a brown dwarf is determined by its mass and radius ($g=GM/R^2$). A young brown dwarf will have a smaller mass and larger radius, and thus a lower surface gravity, than an older brown dwarf at that same temperature. Additionally, the metallicity of a brown dwarf is dependent on the chemical enrichment of its natal environment. Like stars, brown dwarfs with sub-solar metallicities are likely old, and brown dwarfs with super-solar metallicity are young. Thus, young brown dwarfs tend to have low gravity and solar or super-solar metallicity, while old brown dwarfs have higher gravity and solar or sub-solar metallicity. A well-characterized sample of brown dwarfs at a large range of temperatures, gravities, and metallicities serves as a powerful probe of atmospheric evolution at the lowest masses and temperatures and informs the broader understanding of Galactic evolution.

As discussed in Chapter 1, warmer M and L dwarfs were identified in large numbers in the early 2000s, but colder T dwarfs, particularly late-type T dwarfs of spectral types ∼T5 and later, were more elusive. However, within the last decade, spectroscopic follow-up of T dwarf candidates identified from near-to-mid infrared imaging surveys such as the Wide-Field Infrared Survey Explorer (WISE; Wright et al. 2010) and the UKIRT Infrared Deep Sky Survey (UKIDSS; Lawrence et al. 2007), has more than doubled the number of known T dwarfs and revealed a large population of late-type T dwarfs[1] (e.g. DwarfArchives.org, and the compilation by Mace 2014). With these additions, we now have enough confirmed late-T dwarfs to identify photometric and spectroscopic trends (e.g. Kirkpatrick et al. 2011, 2012; Burningham et al. 2013; Mace et al. 2013a) and to investigate outliers.

T dwarfs are classified by their near-infrared spectra (Burgasser et al., 2006b), which are broadly shaped by methane (CH_4) and water (H_2O) absorption features. The strengths of CH_4 and H_2O absorption are largely influenced by changes in temperature in the atmospheres of these T dwarfs (Burgasser et al., 2006a). However, the overall impact of secondary parameters such as gravity, metallicity, and clouds on T dwarf atmospheres can be significant (e.g. Burrows et al. 2002). For example, collision-induced absorption (CIA) of H_2 is strongly dependent on gravity and also on metallicity. Increased H_2 CIA opacity leads to a suppres-

---

[1] It is important to note that WISE follow-up also led to the discovery of the Y dwarf class (Cushing et al., 2011).

sion of the K band flux in T dwarfs (Saumon et al., 2012). At shorter wavelengths, the shape of the blue wing of the Z/Y band is impacted by pressure-broadening of the Na D ($\sim 5890\mathring{A}$) and K I ($\sim 7700\mathring{A}$) doublets in the red-optical part of the spectrum. In low-metallicity, high pressure photospheres, these strong alkali lines are expected to enhance the blue-wing of the Z/Y band (Burrows et al., 2002, 2006; Burgasser et al., 2006a).

The past four years have seen the discovery of the first bonafide late-T subdwarf age benchmarks[2], which serve to inform the roles sub-solar metallicity and high-gravity play in shaping the emergent spectral morphology of the late-T dwarf population. Mace et al. (2013b) (henceforth M13b) presented the first unambiguous late-T subdwarf discovery, Wolf 1130C. Wolf 1130C is a sdT8 companion to a sdM and white dwarf binary system. Inferring metallicity from the M dwarf, Wolf 1130C has the lowest known metallicity of a T dwarf ([Fe/H]$= -0.7 \pm 0.12$ dex; Mace et al., in preparation). This low metallicity is most evident in the Y-band spectrum of Wolf 1130C, which is unusually blue compared to the T8 spectral standard (see Figure 5 of M13b and Figure 5.3 of this text). The discovery of Wolf 1130C was soon followed by the discovery of the sdT6.5 dwarf ULAS J131610.28+075553.0 (ULAS J1316+0755; Burningham et al. 2014), which also displays an unusually blue Y-band spectrum and a suppressed K band, indicative of low-metallcity/high-gravity. Other late-T age benchmarks with inferred sub-solar metallicities include HIP 73786B (Scholz, 2010; Murray et al., 2011), a T6 dwarf companion to a K5 dwarf with a metallicity of [Fe/H] = -0.3 ± 0.1 (Cenarro et al., 2007), and BD +01° 2920B (T8p), a companion to a G1 dwarf with a metallicity of [Fe/H] = -0.38 ± 0.06 (Pinfield et al. 2012; references therein).

Wolf 1130C not only stands out as the most metal-poor, late-T subdwarf discovered to date, it also stands out in $J-H$ color space with $J-H = 0.068 \pm 0.119$ (Mace et al., 2013b). While $J-H$ colors become increasingly bluer with spectral type from late-L to mid-T, T dwarfs with spectral types later than T5 tend to plateau in $J-H$ color (e.g. Burningham et al. 2013; Mace et al. 2013a; see Figure 1). As discussed in M13b, there are several late

---

[2] A subdwarf ('sd') is a metal-deficient star or brown dwarf. Subdwarfs were first identified by Kuiper (1939) as stars that lay below the main sequence in a color-magnitude diagram. The first known substellar subdwarf was 2MASS J05325346+8246465, an L-type dwarf discovered by Burgasser et al. (2003). To date there are 36 known L-type subdwarfs (Zhang et al. 2017 and references therein).

T-dwarfs with unusual colors that stand out from the plateau in $J - H$ color space. Based on MKO photometry from the literature, M13b defined the width of the late-T, $J - H_{MKO}$ plateau to be $-0.5 \leq J - H_{MKO} \leq -0.2$ (see Figure 5.1). Objects with a $J - H_{MKO}$ color > -0.2 were defined as "red" and objects with a $J - H_{MKO}$ color < -0.5 were defined as "blue." Here I refer to objects that lie between the "red" and "blue" color cuts (-0.5 $\leq$ $J - H_{MKO} \leq$ -0.2) as "normal." M13b hypothesized that red $J - H$ color outliers (like Wolf 1130C) may represent the metal-poor/high-gravity objects in the late-T dwarf population, and that the blue $J - H$ color outliers may represent the converse, namely the metal-rich/low-gravity objects. As discussed in M13b, several of the known "red" $J - H$ outliers, such as Wolf 1130C, show signs of old age, and in contrast, blue outliers show evidence of youth. However, there are exceptions to the red and blue designations. For example, HIP 73786B has a normal $J - H$ color ($J - H$ = -0.46 ± 0.04), only 1σ from the "blue" color cut of M13b, which would suggest that it is a potentially metal-rich/low-gravity object, however, as discussed above, its inferred metallicity is sub-solar.

The goal of this chapter is to spectroscopically investigate the nature(s) of the late-T dwarf $J - H$ color outlier population, and thus to test the M13b hypothesis. To identify metallicity/gravity trends in the late-T dwarf population, I compare spectral standards and atmospheric model grids from BT-Settl (Allard et al., 2011, 2012), Burrows et al. (2006), Saumon et al. (2012), and Morley et al. (2012) to medium-resolution, Keck/NIRSPEC Y and H band spectra of thirteen late-T dwarfs. The Y band was chosen because of its ability to separate temperature, which is correlated with H_2O absorption at the long-wavelengths of the Y band, from gravity and metallicity, which, as discussed above, modulate the flux at bluer wavelengths. I expect the least variation in J-band morphology within a given spectral type bin, because spectral typing of these late-type objects is predominantly done in the J band. Thus, to spectroscopically test for the impact of gravity, metallicity, and additional atmospheric parameters like clouds (e.g. Marley et al. 2010; Burgasser et al. 2010) that may lead to unusual $J - H$ colors, I also observed the targets in H band. In Section 5.2, I describe the sample selection, observations, and data reduction technique. Spectroscopic results are presented in Section 5.3. Section 5.4 presents an analysis of the individual spectra, including atmospheric model fitting and a detailed comparison to spectral standards. Section 5.5 discusses the implications of these results and a summary is provided in Section 5.6.

5.2 Sample, Observations, and Data Reduction

5.2.1 Sample Motivation and Selection

Here I present a sample of thirteen T6-T9 brown dwarfs, twelve of which are identified as $J - H_{MKO}$ color outliers following the criteria outlined in M13b. The thirteenth object is HIP 73786B (discussed above), which provides a potentially interesting counter-example to the M13b color hypothesis. Beyond imposing the M13b color criteria, I further require that all of the objects in the sample are observable from the Northern Hemisphere and are bright enough for medium resolution spectroscopic follow-up with the NIRSPEC instrument (McLean et al., 1998) on Keck II ($J < 19.5$ mag). Adding Wolf 1130C to that number, this sample includes over half (13/23) of the late-T dwarf $J - H$ color outlier population as presented in Table 3 of M13b. A summary of the observations is presented in Table 5.1. Of the thirteen dwarfs in the sample, five are classified as "red," seven are classified as "blue," and one is classified as "normal."

5.2.2 NIRSPEC Observations and Data Reduction

All data were obtained between June 2012 and December 2014 using the medium resolution (R∼2000) mode of the NIRSPEC instrument (McLean et al., 1998) on the Keck II telescope. Keck/NIRSPEC is well-suited for medium resolution follow-up of these faint objects as it combines the light-collecting power of the 10-m Keck 2 telescope with a sensitive near-IR spectrometer. Even with a 10-m telescope, the J_{mag} of these objects (between 16.6 and 19, see Table 5.5) make them too faint for NIRSPEC's high-resolution (R∼20,000) mode. In most cases, the targets were observed in both NIRSPEC's N1 filter (equivalent to Y band; ∼0.95-1.12 μm) and N5 filter (equivalent to H band; ∼1.5-1.78 μm) configurations. The exceptions are WISE J075946.98-490454.0 (henceforth WISE J0759-4904; Kirkpatrick et al.

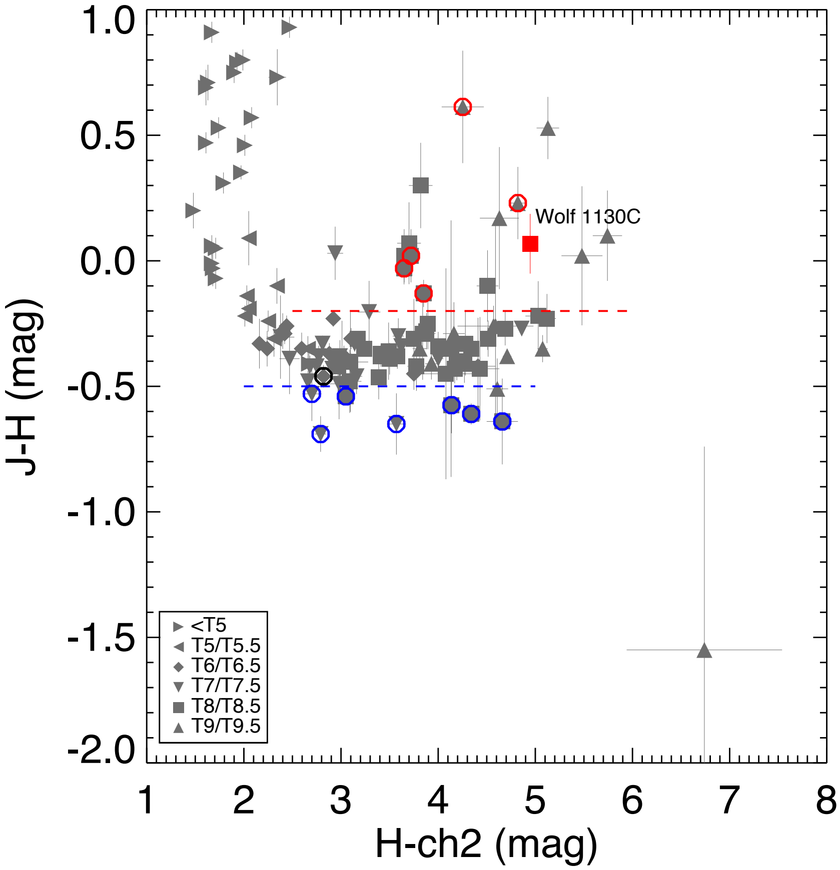

Figure 5.1 A modified version of Figure 8 in M13b: $J - H$ vs $H - ch2$ of T dwarfs from the literature (photometry from Albert et al. 2011, Burningham et al. 2010, 2013, Dupuy & Liu 2012, Kirkpatrick et al. 2011, 2012, Leggett et al. 2010b, 2013, Mace et al. 2013a,b, Thompson et al. 2013). For T dwarfs with spectral types later than T5, $H - ch2$ serves as a proxy for spectral type, with redder $H - ch2$ colors implying later spectral types (Kirkpatrick et al., 2011). The red and blue dashed lines denote the color criteria of M13b; Wolf 1130C is denoted with a red square and labeled for emphasis. Circled objects denote the targets in the sample[3] where the color of the circle denotes their M13b color classification. Late-T dwarfs largely follow a well-defined sequence in $J - H$ vs $H - ch2$, though outliers do exist. Investigating the cause(s) of the unusual outlier photometry is the aim of this study.

2011, Mace et al. 2013a), ULASJ101721.40+011817.9 (ULAS 1017+0118; Burningham et al. 2011), and WISEJ161441.46+173935.5 (WISE J1614+1739; Kirkpatrick et al. 2011). Only Y-band data was obtained for WISE J0759-4904 and WISE J1614+1739. Both Y and H band data was obtained for ULAS J1017+0118, but the SNR for the Y band data was ∼1-2 per resolution element and was deemed too low for this analysis. For two objects, WISE J000517.48+373720.5 (WISE J0005+3732) and WISE J054047.00+483232.4 (WISE J0540+4832), existing NIRSPEC N3 (equivalent to J band; ∼1.15-1.35 μm) spectra are presented in Mace et al. (2013a). Table 5.1 also lists previously unpublished NIRSPEC Y- and H-band spectra for T dwarf spectral standards used in the analysis.

Unless otherwise noted in Table 5.1, targets and standards were observed using NIRSPEC's 0.57″ (3 pixel) slit in the typical AB (or ABBA) nod pattern in order to enable sky background subtraction. Single nod exposure times were either 300s or 600s depending on target brightness. For telluric corrections, an A0 standard star was observed at a similar airmass to the target star either proceeding or following target observations. Flat field, dark, Ne and Ar arc lamp frames (for wavelength calibration) were also observed with each target in each observing mode. All data were reduced in IDL using the publicly available REDSPEC package[4]. REDSPEC performs the standard wavelength calibration, background subtraction, flat fielding, telluric correction, and source extraction. Absorption features in the A0 spectra are removed by interpolation before the calibrator is used for telluric correction. The REDSPEC software is described in more detail in McLean et al. (2003). After reduction, individual target nod pairs are averaged together to improve S/N and a barycentric velocity correction is applied.

---

[3] At the time of writing, *Spitzer ch2* data is not available for HIP 73786B (black circle), so for this object the plotted x-axis value is $H - W2$. Using *W2* photometry instead of *ch2* photometry will induce a small horizontal offset in the location of HIP 73786B compared to the rest of the sample (see e.g. Mainzer et al. 2011), but will not impact the $J - H$ photometry, which is the more relevant quantity for this investigation.

[4] See `https://www2.keck.hawaii.edu/inst/nirspec/redspec.html`

Table 5.1. NIRSPEC Observations

Object Name	Short Name	Discovery Ref.[a]	SpT	SpT Ref.[a]	Band [b]	Date Observed	Exp. Time (sec)	A0	Slit Width ($''$)
WISE J000517.48+373720.5	WISE J0005+3737	1	T9	1	N1	11-Nov-14	3600	HD 222749	0.57
		1	T9	1	N5	11-Nov-14	3000	HD 222749	0.57
ULAS J013939.77+004813.8	ULAS J0139+0048	2	T7.5	2	N1	2-Dec-14	4800	HD 18571	0.57
		2	T7.5	2	N5	2-Dec-14	3600	HD 18571	0.57
CFBDS J030135.11-161418.0	CFBDS J0301-1614	3	T7p	3	N1	11-Nov-14	3600	HD 23683	0.57
		3	T7p	3	N5	12-Nov-14	4200	HD 23683	0.57
WISE J054047.00+483232.4	WISE J0540+4832	1	T8.5	1	N1	11-Nov-14	3000	HD 45105	0.57
		1	T8.5	1	N5	11-Nov-14	2400	HD 45105	0.57
WISE J075946.98-490454.0	WISE J0759-4904	4	T8	4	N1	2-Dec-14	4200	HD 74042	0.57
CFBDS J092250.12+152741.4	CFBDS J0922+1527	3	T7	3	N1	14-Apr-14	3600	HD 111744	0.57
		3	T7	3	N5	3-Dec-14	3000	HD 79108	0.57
ULAS J095047.28+011734.3	ULAS J0950+0118	5	T8p	5	N1	13-Apr-14	3600	HD 95126	0.57
		5	T8p	5	N5	2-Dec-14	3000	HD 79108	0.57
ULAS J101721.40+011817.9	ULAS J1017+0118	6	T8p	6	N5	3-Dec-14	3000	HD 79108	0.57
ULAS J150457.65+053800.8	HIP 73786B	7	T6p	7	N1	14-Apr-14	1800	7 Ser	0.57
		7	T6p	7	N5	20-Jun-14	2400	HD 123233	0.57
WISE J161441.46+173935.5	WISE J1614+1739	4	T9	4	N1	13-Apr-14	2400	26 Ser	0.57
		4	T9	4	N1	14-Apr-14	2400	26 Ser	0.57
WISE J161705.74+180714.1	WISE J1617+1807	8	T8	8	N1	12-Apr-14	2400	q Her	0.57
		8	T8	8	N5	20-Jun-14	2400	q Her	0.57
WISE J181210.85+272144.3	WISE J1812+2721	8	T8.5	8	N1	21-Jun-14	1800	HD 199217	0.57
		8	T8.5	8	N5	20-Jun-14	2400	HD 192538	0.57
ULAS J214638.83-001038.7	Wolf 940B	9	T8.5	9	N1	21-Jun-14	2400	HD 210501	0.57
		9	T8.5	9	N5	11-Nov-14	2400	HD 210501	0.57

Table 5.1 (cont'd)

Object Name	Short Name	Discovery Ref.[a]	SpT	SpT Ref.[a]	Band [b]	Date Observed	Exp. Time (sec)	A0	Slit Width ($''$)
Previously Unpublished NIRSPEC Spectral Standard Observations									
2MASSI J0415195-093506	2MASS J0415-0935	10	T8	11	N1	23-Dec-02	1200	HD 34481	0.38
UGPS J072227.51-054031.2	UGPS J0722-0540	12	T9	13	N1	2-Dec-14	1800	HD 64653	0.57
		12	T9	13	N5	3-Dec-14	1800	HD 64653	0.57
2MASSI J0727182+171001	2MASS J0727+1710	10	T7	11	N1	12-Nov-14	1800	HD 57208	0.57
		10	T7	11	N5	12-Nov-14	1800	HD 57208	0.57
Previously Unpublished Brown Dwarf Spectroscopic Survey (BDSS) Comparison Object Observation									
2MASSI J0937347+293142	2MASS J0937+2931	10	T6p	11	N1	7-Mar-01	1200	AG +27 1006	0.38

[a] Discovery and Spectral Type references- (1) Mace et al. (2013a); (2) Chiu et al. (2008); (3) Albert et al. (2011); (4) Kirkpatrick et al. (2011); (5) Burningham et al. (2013); (6) Burningham et al. (2008); (7) Scholz (2010); (8) Burgasser et al. (2011); (9) Burningham et al. (2009); (10) Burgasser et al. (2002), (11) Burgasser et al. (2006b), (12) Lucas et al. (2010), (13) Cushing et al. (2011)

[b] Keck/NIRSPEC J band spectra of WISE J0540+4832 and WISE J0005+3737 were presented in Mace et al. (2013a). A Keck/NIRSPEC J band spectrum of 2MASS J0727+1710 and both J and H band spectra of 2MASS J0415-0935 were presented in McLean et al. (2003).

5.3 Results

The sample is comprised of one T6 dwarf, three T7/T7.5 dwarfs, seven T8/T8.5 dwarfs, and two T9 dwarfs. In Figure 5.2 I present Y- and H-band NIRSPEC spectra, plotted together by spectral type. Spectra are colored according to their $J-H$ color (i.e. targets with a "red" $J-H$ color are plotted in red, and targets with a "blue" $J-H$ color are plotted in blue). For the T7-T9 objects, medium-resolution spectral standards observed as part of the NIRSPEC Brown Dwarf Spectroscopic Survey (BDSS; e.g. McLean et al. 2003) are also plotted for comparison. Except for the H-band observations of the T8 standard, presented in McLean et al. (2003), the Y- and H-band spectra of the standards are presented here for the first time. All spectral standards were reduced in the same manner as described in Section 5.2.2. Figure 5.3 compares the T8/T8.5 spectra with the spectrum of the extremely metal-poor, T8sd Wolf 1130C presented in M13b.

Somewhat surprisingly based on the Wolf 1130C discovery, visual comparison of the targets with each other and with Wolf 1130C suggests that the spectral morphologies of the dwarfs in this sample are more consistent with spectral standards than Wolf 1130C. For the T8/T8.5 objects, which comprise seven of the thirteen objects in the sample, there is *no clear delineation* between the unusually red and blue objects in the sample. Instead, the targets tend to clump around the spectral standard. The broad similarities among the T8/T8.5 targets are particularly evident in the Y band, where the flux of the peak-normalized Wolf 1130C is significantly broadened towards the blue end of the band, indicative of sub-solar metallicity/high-gravity, whereas the targets in this sample all have much narrower and redder flux peaks. Why is the sample so homogeneous, and why are none of the color outliers as extreme as Wolf 1130C? I examine potential explanations for this homogeneity in Section 5.5.

Though fairly homogeneous overall, the individual targets in the sample are not identical. For example, one of the two T9 objects in Figure 5.2 is visually separated from the other color outlier and the spectral standard in the Y-band. In Section 5.4 I take a closer look at the individual objects in the sample and use model and spectral standard comparison to

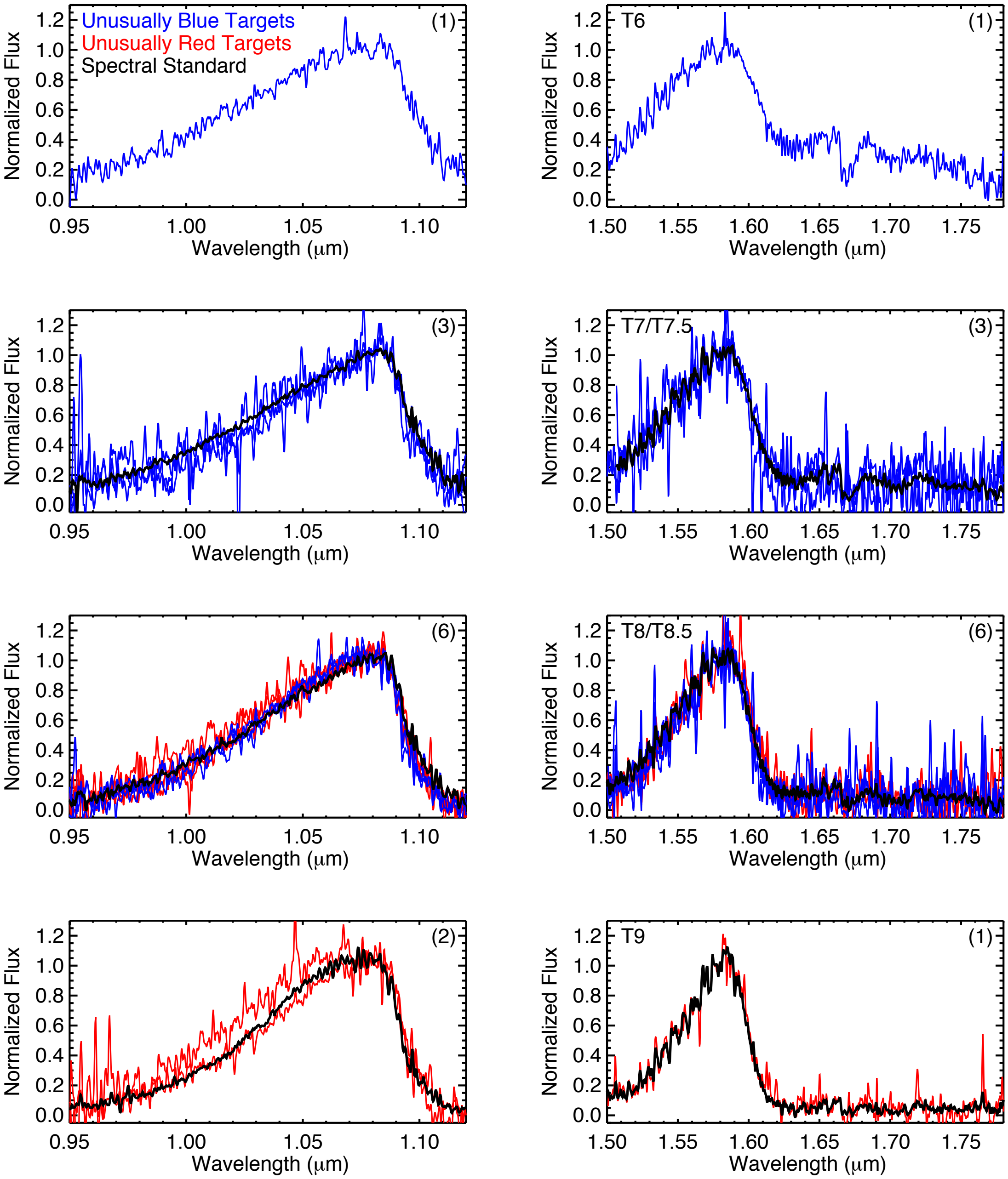

Figure 5.2 NIRSPEC Y-band (left) and H-band (right) spectra of the sample from T6 (top panel) to T9 (bottom). The spectra are normalized at 1.08 μm and 1.59 μm respectively. Objects with unusually red and blue $J - H_{MKO}$ colors as defined by M13b are plotted by color accordingly. The number given in parenthesis at the upper left of each panel indicates the number of spectra over-plotted in that panel. When available, spectral standards from the Brown Dwarf Spectroscopic Survey (BDSS; McLean et al. 2003), are overplotted in black for comparison. The spectral standards are as follows: 2MASSI J0727182+171001 (T7; Burgasser et al. 2002, 2006b), 2MASSI J0415195-093506 (T8; Burgasser et al. 2002, 2006b), and UGPS J072227.51-054031.2 (T9; Lucas et al. 2010; Cushing et al. 2011).

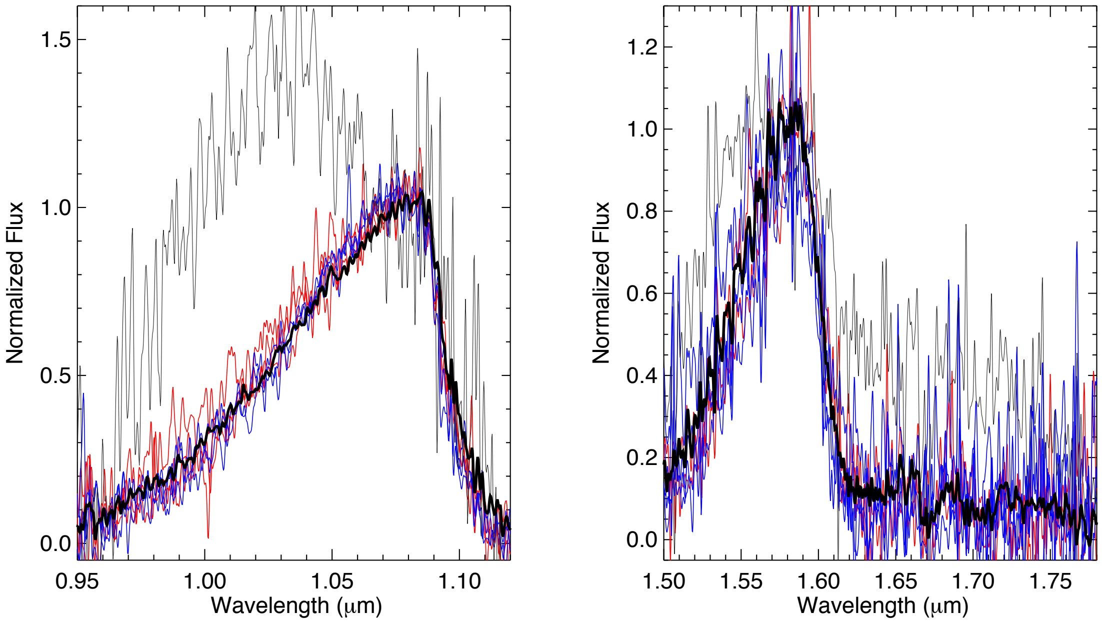

Figure 5.3 NIRSPEC Y- and H- band spectra of the T8 and T8.5 dwarfs in this sample (see Figure 5.2 for details) compared to the Y- and H- band spectra of the metal-poor, sdT8 Wolf 1130C (grey; M13b). The Y band of Wolf 1130C is significantly broadened towards the blue end of the band and the H band features both a broader peak and decreased methane absorption.

investigate the variations among the targets.

5.4 Analysis

In the following section, I investigate the range of model parameter space probed by the targets in the sample. I also highlight and discuss the model fits and known properties of four objects that visually deviate from their respective spectral standard. This section begins with a brief discussion of the four publicly-available atmospheric models employed in this analysis.

5.4.1 A Comparison of the Models

With temperatures < 1000 K, the latest-type T dwarfs pose a challenge for atmospheric modeling due to the complex molecular chemistries, clouds, and disequilibrium processes present in their atmospheres (for a detailed review of brown dwarf atmospheric model development and construction see Marley & Robinson 2015). Nevertheless, several teams have made significant strides towards modeling the atmospheres of these cool objects. We consider four sets of model atmosphere grids in this analysis: the cloud-free models of Burrows et al. (2006) (henceforth Burrows models), the cloudy CIFIST 2011 version of the BT-Settl models (henceforth BT-Settl models; Allard et al. 2011, 2012), the cloud-free models of Saumon et al. (2012) (henceforth Saumon models), and the sulfide cloud models of Morley et al. (2012) (henceforth Morley models). Though the Burrows model grid is lower-resolution than the NIRSPEC data and only reaches a minimum temperature of $T_{eff} = 700$ K, it is the only publicly available model set that includes both subsolar ([Fe/H] = -0.5 dex) and supersolar ([Fe/H] = +0.5 dex) metallicities at late-T dwarf temperatures. The publicly available BT-Settl models do provide non-solar metallicity grids, but the complete non-solar set only extends down to $T_{eff} = 1000$ K. Some sub-solar metallicity spectra for limited $\log g$ values down to $T_{eff} = 800$ K are also available in the publicly available BT-Settl grids, but the limited non-solar metallicity spectra were not considered in this analysis. The Saumon and Morley models only consider solar metallicities, but the two models have the advantage

Table 5.2. Model Comparison

Model Short Name	Reference	T_{eff} Range	$\log g$ Range	Clouds?	[Fe/H]
Burrows	Burrows et al. 2006	700-2300 K	4.5-5.5	no[a]	-0.5, 0., +0.5[b]
BT-Settl	Allard et al. 2011, 2012	400-7000 K	3.5-5	yes	0.[c]
Saumon	Saumon et al. 2012	300-1500 K	3.75-5.5	no	0.
Morley	Morley et al. 2012	400-1300 K	4-5.5	yes	0.

[a] Cloudy Burrows models are available, but we only consider the clear models in this analysis.

[b] At T_{eff}= 700 K, [Fe/H] = +0.5 dex is only available for the log(g) = 5.0 dex case.

[c] Non-solar [Fe/H] CIFIST 2011 BT-Settl models are available, but do not cover the the entire range of temperatures considered in this analysis and were thus not included in this work.

that they only differ in their treatment of clouds, allowing for a direct test of the impact of clouds on the data. Table 5.2 summarizes the parameter space covered by each model used in this analysis.

Figure 5.4 is a direct comparison of the peak-normalized spectra output from the four models given identical input parameters (T_{eff} = 700 K, $\log g$ = 4.5 dex (cgs), [Fe/H] = 0 dex; f_{sed}[5]=3 for the Morley model spectrum). While all four models are in relatively good agreement in the *J* band, the BT-Settl models predict deeper 1.65 μm methane absorption in the *H* band, and both the BT-Settl and Burrows model spectra show enhanced flux in the blue wing of the *Y* band when compared to the Saumon and Morley model spectra. While these variations are not entirely unexpected given the differences in molecular line lists, particularly for methane, and varied treatment of alkali metals and clouds among the models, these differences must be kept in mind when comparing the models with each other and with observed data. The physical implications of these differences are discussed in more

---

[5] As described in Morley et al. (2012), f_{sed} describes the sedimentation efficiency of the atmosphere. In the Morley models, f_{sed} ranges from 2 to 5, with 2 indicating small particle sizes/optically thick clouds and 5 indicating large particle sizes/optically thinner clouds.

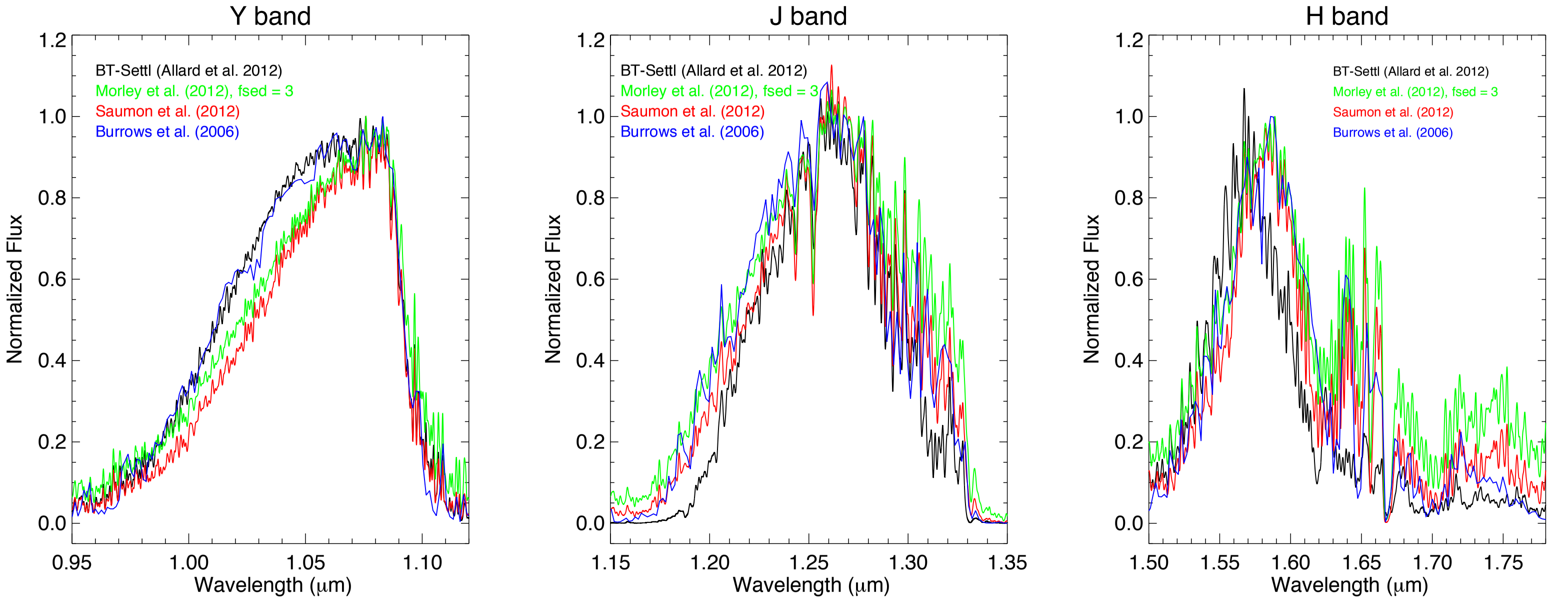

Figure 5.4 Direct comparison of the BT-Settl (black, Allard et al. 2011, 2012), Burrows (blue; Burrows et al. 2006), Saumon (red; Saumon et al. 2012), and Morley (green; Morley et al. 2012) atmospheric models in *Y*, *J*, and *H* band. All models assume T_{eff}= 700 K, $\log g$= 4.5 dex, and solar metallicity. The BT-Settl, Saumon, and Morley models have been binned down to match the resolution of NIRSPEC. The Burrows models are lower resolution than the NIRSPEC data, and thus are plotted at their native resolution. The Morley model assumes f_{sed}= 3. There are clear differences in the models at these low temperatures, particularly in the blue wing of the *Y* band and in the strength of the methane dropout in the *H* band. These discrepancies are discussed further in Section 5.4.2 of the text.

detail in Section 5.4.2.

5.4.2 Model Fitting

Using chi-squared minimization, I compare the target spectra to the four model grids discussed above. I normalize both data and model spectra to the flux peak in each band (~1.08 μm in Y and ~1.58 μm in H band) prior to fitting by calculating the robust mean of the data within ± 0.01 μm of the flux peak and dividing each data point by that value. I fit the Y- and H- band spectra individually for each target. Each model spectrum is smoothed to the resolution of the target data by convolving the model data with a Gaussian profile and interpolating onto the target's wavelength solution before fitting. In the case of the lower-resolution Burrows models, the spectra are only interpolated onto the NIRSPEC target's wavelength solution before fitting.

To explore the parameter space probed by the models and to look for trends in the data set, I ran a series of model fit tests holding one quantity fixed (either T_{eff} or $\log g$) and allowing all other quantities to vary (see Tables 5.3 and 5.4). In the fixed effective temperature case, I hold T_{eff} to fall within the 1σ range of T_{eff} for that spectral type (rounded to the nearest 50K) as derived in Filippazzo et al. (2015)[6] and allow gravity, f_{sed}, and metallicity (where applicable) to vary. In the fixed gravity-case, I hold gravity fixed at $\log g = 4.5$ dex and allow T_{eff}, f_{sed}, and metallicity (where applicable) to vary. I then visually inspected the best-fit results in each scenario by plotting the best-fit model solution for each of the four atmospheric model grids against each target. I also calculated and examined the Target-Data residuals for each model. Example best-fit results for WISE J1812+2721, a T8.5 "blue" target in our sample, at fixed T_{eff} and gravity are shown in Figures 5.5 and 5.6 respectively. For clarity, the residuals have been binned to R~200.

---

[6] Filippazzo et al. (2015) use parallaxes (or, in a few cases, kinematic distances) and a combination of optical to mid-infrared photometry and spectroscopy to determine bolometric luminosities (L_{bol}) for a sample of late-M, L, and T dwarfs. They then combine their measured L_{bol} with radii determined from evolutionary models to derive a semi-empirical T_{eff} versus spectral type relation for the young and field brown dwarf population. The uncertainty on the T_{eff} fit is 113 K.

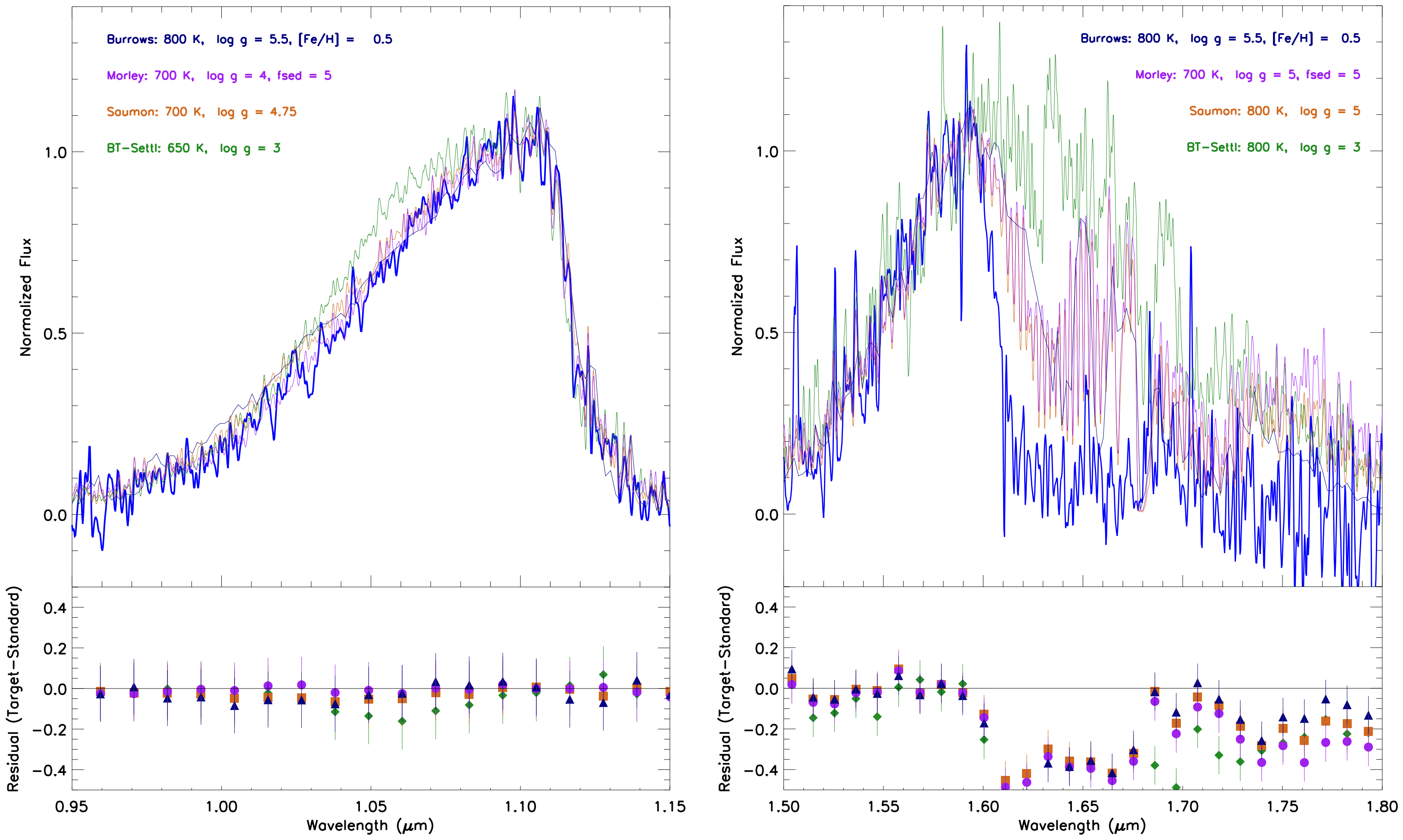

Figure 5.5 Comparison of the Y and H band spectra for the bluest T8.5 dwarf in the sample, WISE J1812+2721, to the best-fit atmospheric models for the BT-Settl, Burrows, Morley, and Saumon grids obtained while holding T_{eff} fixed to fall within the 1σ range of T_{eff} for T8 ($550 \leq T_{eff} \leq 800$) and T9 ($400 \leq T_{eff} \leq 600$) dwarfs as defined in Filippazzo et al. 2015. The target spectrum is colored by its $J-H$ color as blue. The best fit model spectrum and the resulting residuals for the Burrows (navy triangles), Morley (purple circles), Saumon (orange squares), and BT-Settl (green diamonds) model atmosphere grids are also plotted. For the H-band spectrum, the models are only fit to the 1.5-1.59 μm region. Note that the BT-Settl model overestimates the flux of the target in the 1.05 μm region of the Y band.

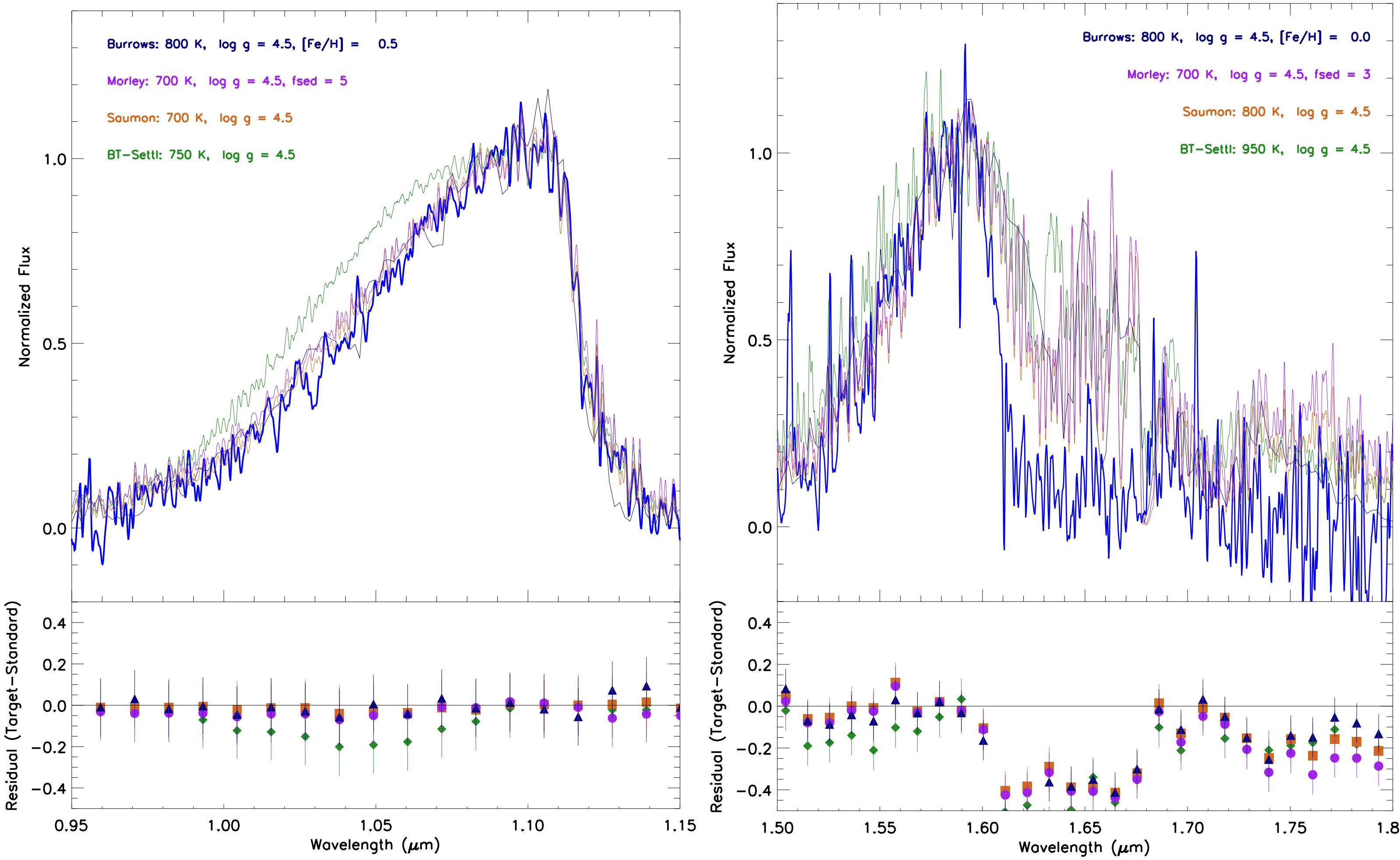

Figure 5.6 Comparison of the Y (left) and H band (right) spectra for the bluest T8.5 dwarf in the sample, WISE J1812+2721, to the best-fit atmospheric models for the BT-Settl, Burrows, Morley, and Saumon grids while holding $\log g = 4.5$ dex. See Figure 5.5 for more details.

5.4.2.1 Trends in the Y-Band Fits for fixed T_{eff}

With T_{eff} fixed, I am able to investigate the impact of gravity, metallicity, and f_{sed} where applicable, on the data set (see Table 5.3). For each model grid, the variation between the best-fit values for each object of a given spectral type is typically small. For example, six of the seven T8/T8.5 targets are best-fit by the exact same Burrows model ($T_{eff} = 800$, $\log g =$ 5.5 dex, and [Fe/H] = +0.5 dex), and the standard deviation in model fits for the BT-Settl, Saumon, and Morley models are typically within one step[7] in the model grid ($\Delta T_{eff} < 100$ K, $\Delta \log g \leq 0.5$ dex, $\Delta f_{sed} = 0.9$). The lack of spread between individual fits from a given model implies that there is no distinct trend in model fit with $J - H$ color (see Section 5.5 for a discussion on the homogeneity of the sample).

While the variation between the best-fit results for each spectrum given a specific model grid is typically less than a step size, there are more significant variations in best-fit results across the four model grids. As discussed in Section 5.4.1, the BT-Settl models and the Burrows models predict enhanced flux in the blue-wing of the Y band when compared to the Morley and Saumon models at the same T_{eff} and $\log g$ values. When all four models are independently fit to the same target with T_{eff} fixed, the best-fit BT-Settl models tend to have a lower gravity (for most spectra, $\log g$ = 3-3.5 dex) compared to the best-fit model spectra from the other three model grids. The lower gravity serves to narrow the overall Y-band flux peak, notably decreasing the flux in the blue wing of the Y band as discussed in the Introduction to this chapter. Even with lower best-fit gravities than the other model grids, the BT-Settl models tend to overestimate the flux for most of the targets and the NIRSPEC spectral standards in the ~1.05 μm region (see e.g. Figure 5.5). The Burrows model grid also predicts enhanced flux in the blue wing of the Y band compared to the equivalent T_{eff} and $\log g$ Saumon and Morley model grids. However, the Burrows model grid does not span the full range of gravity space that the BT-Settl grid probes, only allowing 4.5 dex $< \log g$ $<$ 5.5 dex. Instead, to account for an excess blue-wing flux, the Burrows best-fit model

---

[7] The typical parameter step sizes for the model grids considered in this analysis are ΔT_{eff} = 100 K, $\Delta \log g$ = 0.5 dex, Δf_{sed} = 1, though some model grids have finer sampling for smaller ranges of T_{eff} and $\log g$.

spectra for nine of the twelve targets in the sample with Y-band spectra feature a super-solar [Fe/H], which similarly decreases the blue-wing flux. It should be noted that these nine objects include both red and blue outliers, so again there is no color trend associated with this result. The three remaining targets (HIP 73786B, CFBDS J0301-1614, and WISE J1614+1739) are fit by solar metallicity Burrows models and are discussed individually in Section 5.4.3. In most cases the Morley and Saumon model fits return best-fit spectra that agree to within $\Delta T_{eff} \leq 100$ K and $\log g \leq 0.5$ dex, and most targets are fit with Morley $f_{sed} = 4$ or 5 (see Section 5.5.2 for more discussion on clouds and variability).

5.4.2.2 Trends in the Y-Band Fits for Fixed $\log g$

With gravity fixed to $\log g = 4.5$ dex, I am able to probe the impact of T_{eff}, metallicity, and f_{sed} on the data set (see Table 5.4). The fixed gravity results are very similar to those determined in the fixed T_{eff} scenario. For every target, the Burrows models reproduce the same best-fit [Fe/H] value in both scenarios. For most targets, the T_{eff} at fixed gravity for each model grid agrees within 100 K of the best-fit value derived for that model grid in the fixed T_{eff} scenario. There are only three targets that have at least one model-fit T_{eff} value more than 150K from the value obtained for that model in the fixed T_{eff} scenario. These exceptions are CFBDS J0301-1614, HIP 73786B, and WISE J1617+1807. For CFBDS J0301-1614 and HIP 73786B, the Morley T_{eff} values vary by 300 K and 450 K respectively and the f_{sed} values also vary by 3 and 2 steps respectively. Both of these objects stood out in the fixed T_{eff} case as well and are discussed in more detail below. For WISE J1617+1807 the Burrows temperatures differ by 200 K and the Morley temperatures differ by 150 K. WISE J1617+1807 is well-matched by the T8 spectral standard (see Section 5.8), showing no strong evidence for spectral peculiarity. This object highlights the need for caution when assigning physical properties to individual targets based on a single model fit over a narrow wavelength region. I measure and provide individual fit values in Tables 5.3 and 5.4 to identify trends and outliers, but do not assign specific T_{eff}, $\log g$, and metallicity values to individual targets.

Table 5.3. *Y*- and *H*- band Model Fits: Fixed T_{eff}

			Y band				*H* band			
Short Name	SpT	Model ^{a,b}	T_{eff}	$\log g$	[Fe/H]	f_{sed}	T_{eff}	$\log g$	[Fe/H]	f_{sed}
WISE J0005+3737	T9									
		BT-Settl (fixed T_{eff} range)	550	3	-	-	600	5	-	-
		Burrows (fixed T_{eff} range)	800	4.5	0.5	-	700	4.5	0	-
		Morley (fixed T_{eff} range)	450	4	-	4	600	5.5	-	4
		Saumon (fixed T_{eff} range)	450	4.25	-	-	600	3	-	-
ULAS J0139+0048	T7.5									
		BT-Settl (fixed T_{eff} range)	800	3	-	-	950	5.5	-	-
		Burrows (fixed T_{eff} range)	900	4.5	0.5	-	900	4.5	-0.5	-
		Morley (fixed T_{eff} range)	800	4	-	5	900	5.5	-	4
		Saumon (fixed T_{eff} range)	800	3	-	-	950	3.75	-	-
CFBDS J0301-1614	T7p									
		BT-Settl (fixed T_{eff} range)	700	3.5	-	-	700	5	-	-
		Burrows (fixed T_{eff} range)	700	5	0	-	700	4.5	0	-
		Morley (fixed T_{eff} range)	700	4	-	5	700	4.5	-	5
		Saumon (fixed T_{eff} range)	700	4.5	-	-	700	5.5	-	-
WISE J0540+4832	T8.5									
		BT-Settl (fixed T_{eff} range)	800	3.5	-	-	800	3	-	-
		Burrows (fixed T_{eff} range)	800	5.5	0.5	-	800	5.5	0.5	-
		Morley (fixed T_{eff} range)	700	4.5	-	5	700	5	-	5
		Saumon (fixed T_{eff} range)	750	4.75	-	-	800	5	-	-
WISE J0759-4904	T8									
		BT-Settl (fixed T_{eff} range)	800	3.5	-	-	N/A	N/A	N/A	N/A
		Burrows (fixed T_{eff} range)	800	5.5	0.5	-	N/A	N/A	N/A	N/A
		Morley (fixed T_{eff} range)	700	4	-	3	N/A	N/A	N/A	N/A
		Saumon (fixed T_{eff} range)	800	4.75	-	-	N/A	N/A	N/A	N/A
CFBDS J0922+1527	T7									
		BT-Settl (fixed T_{eff} range)	850	3.5	-	-	950	3.5	-	-
		Burrows (fixed T_{eff} range)	900	5.5	0.5	-	900	5.5	0	-
		Morley (fixed T_{eff} range)	800	4.5	-	3	900	5	-	4
		Saumon (fixed T_{eff} range)	900	5	-	-	950	5	-	-
ULAS J0950+0118	T8p									
		BT-Settl (fixed T_{eff} range)	550	4	-	-	800	3	-	-
		Burrows (fixed T_{eff} range)	800	4.5	0.5	-	800	5.5	0	-
		Morley (fixed T_{eff} range)	550	4	-	5	800	5	-	5
		Saumon (fixed T_{eff} range)	550	4	-	-	800	5	-	-

Table 5.3 (cont'd)

Short Name	SpT	Model [a,b]	Y band T$_{eff}$	log g	[Fe/H]	f_{sed}	H band T$_{eff}$	log g	[Fe/H]	f_{sed}
ULAS J1017+0118	T8p									
		BT-Settl (fixed T$_{eff}$ range)	N/A	N/A	N/A	N/A	800	3.5	-	-
		Burrows (fixed T$_{eff}$ range)	N/A	N/A	N/A	N/A	800	4.5	-0.5	-
		Morley (fixed T$_{eff}$ range)	N/A	N/A	N/A	N/A	800	5	-	4
		Saumon (fixed T$_{eff}$ range)	N/A	N/A	N/A	N/A	800	5.5	-	-
HIP 73786B	T6p									
		BT-Settl (fixed T$_{eff}$ range)	950	5.5	-	-	1100	5	-	-
		Burrows (fixed T$_{eff}$ range)	1000	5.5	0	-	1100	5.5	0	-
		Morley (fixed T$_{eff}$ range)	900	5.5	-	4	1000	5.5	-	4
		Saumon (fixed T$_{eff}$ range)	900	5.5	-	-	1100	5.5	-	-
WISE J1614+1739	T9									
		BT-Settl (fixed T$_{eff}$ range)	550	3	-	-	N/A	N/A	N/A	N/A
		Burrows (fixed T$_{eff}$ range)	700	4.5	0	-	N/A	N/A	N/A	N/A
		Morley (fixed T$_{eff}$ range)	600	5	-	5	N/A	N/A	N/A	N/A
		Saumon (fixed T$_{eff}$ range)	550	3	-	-	N/A	N/A	N/A	N/A
WISE J1617+1807	T8									
		BT-Settl (fixed T$_{eff}$ range)	800	4.5	-	-	800	3	-	-
		Burrows (fixed T$_{eff}$ range)	800	5.5	0.5	-	800	5	0	-
		Morley (fixed T$_{eff}$ range)	550	5	-	5	800	5	-	5
		Saumon (fixed T$_{eff}$ range)	800	5.5	-	-	800	5.5	-	-
WISE J1812+2721	T8.5									
		BT-Settl (fixed T$_{eff}$ range)	650	3	-	-	800	3	-	-
		Burrows (fixed T$_{eff}$ range)	800	5.5	0.5	-	800	5.5	0.5	-
		Morley (fixed T$_{eff}$ range)	700	4	-	5	700	5	-	5
		Saumon (fixed T$_{eff}$ range)	700	4.75	-	-	800	5	-	-
Wolf 940B	T8.5									
		BT-Settl (fixed T$_{eff}$ range)	800	3.5	-	-	800	3	-	-
		Burrows (fixed T$_{eff}$ range)	800	5.5	0.5	-	800	5.5	0.5	-
		Morley (fixed T$_{eff}$ range)	700	4.5	-	5	700	5	-	4
		Saumon (fixed T$_{eff}$ range)	600	4.75	-	-	800	5.5	-	-

[a] Model Citations: BT-Settl - Allard et al. (2011, 2012), Burrows - Burrows et al. (2006), Morley - Morley et al. (2012), Saumon - Saumon et al. (2012)

[b] 'Fixed T$_{eff}$ range' implies the best fit is obtained for each model while holding T$_{eff}$ fixed to fall within the 1σ range of T$_{eff}$ for a given spectral type as defined in Filipazzo et al. (2015) and allowing all other parameters ($\log g$, [Fe/H], f_{sed}) to vary.

Table 5.4. Y- and H-band Model Fits: Fixed $\log g$

			Y band				H band			
Short Name	SpT	Model ^{a,b}	T$_{eff}$	$\log g$	[Fe/H]	f_{sed}	T$_{eff}$	$\log g$	[Fe/H]	f_{sed}
WISE J0005+3737	T9									
		BT-Settl (fixed $\log g$)	700	4.5	-	-	500	4.5	-	-
		Burrows (fixed $\log g$)	800	4.5	0.5	-	700	4.5	0	-
		Morley (fixed $\log g$)	450	4.5	-	5	600	4.5	-	3
		Saumon (fixed $\log g$)	500	4.5	-	-	700	4.5	-	-
ULAS J0139+0048	T7.5									
		BT-Settl (fixed $\log g$)	750	4.5	-	-	1000	4.5	-	-
		Burrows (fixed $\log g$)	900	4.5	0.5	-	900	4.5	-0.5	-
		Morley (fixed $\log g$)	800	4.5	-	5	1000	4.5	-	2
		Saumon (fixed $\log g$)	850	4.5	-	-	1150	4.5	-	-
CFBDS J0301-1614	T7p									
		BT-Settl (fixed $\log g$)	750	4.5	-	-	550	4.5	-	-
		Burrows (fixed $\log g$)	800	4.5	0	-	700	4.5	0	-
		Morley (fixed $\log g$)	400	4.5	-	2	600	4.5	-	3
		Saumon (fixed $\log g$)	700	4.5	-	-	700	4.5	-	-
WISE J0540+4832	T8.5									
		BT-Settl (fixed $\log g$)	800	4.5	-	-	950	4.5	-	-
		Burrows (fixed $\log g$)	900	4.5	0.5	-	800	4.5	0	-
		Morley (fixed $\log g$)	700	4.5	-	5	700	4.5	-	4
		Saumon (fixed $\log g$)	750	4.5	-	-	800	4.5	-	-
WISE J0759-4904	T8									
		BT-Settl (fixed $\log g$)	800	4.5	-	-	N/A	N/A	N/A	N/A
		Burrows (fixed $\log g$)	900	4.5	0.5	-	N/A	N/A	N/A	N/A
		Morley (fixed $\log g$)	800	4.5	-	5	N/A	N/A	N/A	N/A
		Saumon (fixed $\log g$)	800	4.5	-	-	N/A	N/A	N/A	N/A
CFBDS J0922+1527	T7									
		BT-Settl (fixed $\log g$)	850	4.5	-	-	950	4.5	-	-
		Burrows (fixed $\log g$)	1000	4.5	0.5	-	1100	4.5	0	-
		Morley (fixed $\log g$)	800	4.5	-	3	1000	4.5	-	5
		Saumon (fixed $\log g$)	900	4.5	-	-	1050	4.5	-	-
ULAS J0950+0118	T8p									
		BT-Settl (fixed $\log g$)	550	4.5	-	-	950	4.5	-	-
		Burrows (fixed $\log g$)	800	4.5	0.5	-	700	4.5	-0.5	-
		Morley (fixed $\log g$)	400	4.5	-	5	800	4.5	-	3

Table 5.4 (cont'd)

			Y band				*H* band			
Short Name	SpT	Model [a,b]	T_{eff}	$\log g$	[Fe/H]	f_{sed}	T_{eff}	$\log g$	[Fe/H]	f_{sed}
		Saumon (fixed $\log g$)	400	4.5	-	-	900	4.5	-	-
ULAS J1017+0118	T8p									
		BT-Settl (fixed $\log g$)	N/A	N/A	N/A	N/A	950	4.5	-	-
		Burrows (fixed $\log g$)	N/A	N/A	N/A	N/A	1000	4.5	0	-
		Morley (fixed $\log g$)	N/A	N/A	N/A	N/A	900	4.5	-	5
		Saumon (fixed $\log g$)	N/A	N/A	N/A	N/A	950	4.5	-	-
HIP 73786B	T6p									
		BT-Settl (fixed $\log g$)	950	4.5	-	-	1050	4.5	-	-
		Burrows (fixed $\log g$)	1100	4.5	0	-	1000	4.5	-0.5	-
		Morley (fixed $\log g$)	550	4.5	-	2	1100	4.5	-	2
		Saumon (fixed $\log g$)	1000	4.5	-	-	1300	4.5	-	-
WISE J1614+1739	T9									
		BT-Settl (fixed $\log g$)	700	4.5	-	-	N/A	N/A	N/A	N/A
		Burrows (fixed $\log g$)	700	4.5	0	-	N/A	N/A	N/A	N/A
		Morley (fixed $\log g$)	550	4.5	-	5	N/A	N/A	N/A	N/A
		Saumon (fixed $\log g$)	550	4.5	-	-	N/A	N/A	N/A	N/A
WISE J1617+1807	T8									
		BT-Settl (fixed $\log g$)	800	4.5	-	-	950	4.5	-	-
		Burrows (fixed $\log g$)	1000	4.5	0.5	-	900	4.5	0	-
		Morley (fixed $\log g$)	800	4.5	-	4	800	4.5	-	4
		Saumon (fixed $\log g$)	900	4.5	-	-	900	4.5	-	-
WISE J1812+2721	T8.5									
		BT-Settl (fixed $\log g$)	750	4.5	-	-	950	4.5	-	-
		Burrows (fixed $\log g$)	800	4.5	0.5	-	800	4.5	0	-
		Morley (fixed $\log g$)	700	4.5	-	5	700	4.5	-	3
		Saumon (fixed $\log g$)	700	4.5	-	-	800	4.5	-	-
Wolf 940B	T8.5									
		BT-Settl (fixed $\log g$)	800	4.5	-	-	950	4.5	-	-
		Burrows (fixed $\log g$)	900	4.5	0.5	-	800	4.5	0	-
		Morley (fixed $\log g$)	700	4.5	-	5	700	4.5	-	3
		Saumon (fixed $\log g$)	750	4.5	-	-	800	4.5	-	-

[a] Model Citations: BT-Settl - Allard et al. (2011, 2012), Burrows - Burrows et al. (2006), Morley - Morley et al. (2012), Saumon - Saumon et al. (2012)

[b] 'Fixed $\log g$' reports the best fit obtained for each model while holding $\log g = 4.5$ dex and allowing all other parameters to vary.

5.4.2.3 Trends in the *H*-Band Fits

The 1.6 μm methane absorption in the H band of the target spectra is poorly matched by all four atmospheric model grids considered in this analysis. Incomplete methane line lists in the models are likely the dominant cause of the lack of agreement (Saumon et al., 2012). To minimize the impact of a poor methane fit on the model fit results, I only fit the 1.5-1.59 μm region of the H-band spectrum. As illustrated in Figures 5.5 and 5.6, even in the 1.5-1.59 μm region the best-fit atmospheric models tend to provide a poorer fit to the data than the Y-band fits. This is reflected in a larger scatter in the best-fit intra-model H-band results for both the fixed T_{eff} and fixed $\log g$ cases compared to the Y band results. However, as is the case for the Y band, neither the intra-model or the inter-model scatter is associated with a trend in $J - H$ color.

Even with the larger scatter, there are some general trends among the model fits. In the fixed T_{eff} case, the best-fit BT-Settl models tend to have a lower gravity (for most spectra, $\log g$ = 3-3.5 dex) than the best-fit model spectra from the other three model grids, just as they did in the Y band. Also, the Morley and Saumon gravity results are on average about 0.5 dex higher than in the Y-band fits. In the fixed $\log g$ case, the BT-Settl, Morley, and Saumon best-fit results for each object are either warmer or the same temperature than the best-fit result for that object in the Y band. The only exception to this is CFBDS J0301-1614, which is poorly fit by all model grids in the H band and is discussed in more detail below. Constrained to a fixed $\log g = 4.5$ dex, seven of the eleven targets with H-band spectra are fit by significantly cloudy (f_{sed} = 2-3) Morley models. This last result is likely unphysical, driven by forcing $\log g$ =4.5 dex. A lower gravity decreases the width of the flux peak in a normalized H band, and a cloudy atmosphere compensates by increasing the width of the blue-wing of the H band (see Figure 5.12). When $\log g$ is allowed to vary in the fixed T_{eff} scenario, the H-band Morley best-fits on average have $\log g = 5.0$ dex and f_{sed} = 4-5.

Ultimately, comparing the Y- and H-band spectra of the target sample to the BT-Settl, Burrows, Morley, and Saumon models serves to illustrate the differences among the models and highlights the difficulty of modeling the atmospheres of the coldest products of the star formation process. However, the overall homogeneity of the sample is supported by the best-fit results for each model grid. The Y-band fits in particular identify four potentially unusual targets worth further discussion. These targets are addressed in the next section.

5.4.3 Characteristics of Unusual Objects in the Sample

ULAS J150457.65+053800.8 (HIP 73786B):

HIP 73786B (T6p) is a known wide-separation, proper motion companion to HIP 73786A (Scholz 2010; Murray et al. 2011), which has a K8V spectral type (Gray et al., 2003). Based on WFCAM photometry from Murray et al. (2011), HIP 73768B is classified as 'normal' based on the M13b $J - H$ color criteria, however there is strong evidence that this object is unusual. HIP 73786B has an inferred distance of 18.6 ± 0.97 pc (van Leeuwen 2007) and a metallicity of [Fe/H] = -0.3 ± 0.1 dex (Cenarro et al., 2007), based on the properties of the primary. Burningham et al. (2014) present a R∼120 IRTF/SpeX (Rayner et al., 2003) spectrum of this object and showed that the Y-band flux peak is enhanced and the K-band flux peak is depressed, indicative of low-metallicity/high-gravity. In Figure 5.7, I compare the NIRSPEC Y- and H-band spectra of HIP 73786B to BDSS T dwarfs from the literature (McLean et al., 2003) and to a previously unpublished NIRSPEC BDSS Y-band spectrum of the likely metal-poor, T6p dwarf 2MASS J09373487+2931409 (2MASS J0937+2931; Burgasser et al. 2002, 2006b). Like Burningham et al. (2014), I also find that the Y-band flux peak is enhanced in the NIRSPEC data, and is best matched by the Y-band spectrum of 2MASS J0937+2931. All four best-fit model spectra at fixed T_{eff} range are consistent with high-gravity in the Y band and the truncated H band, including the BT-Settl model (see Table 5.3). Unlike Wolf 1130C, which has an enhanced H band compared to other T8 brown dwarfs, comparing HIP 73786B to other T4.5-T7 dwarfs in the BDSS shows that the H-band spectrum of HIP 73786B is reasonably well-matched by the T5.5 dwarf, 2MASSI J2356547-155310[8] (2MASS I2356-1553, Burgasser et al. 2002, 2006b). The

---

[8] It should be noted that the BDSS library does not include an H-band spectrum of 2MASS J0937+2931.

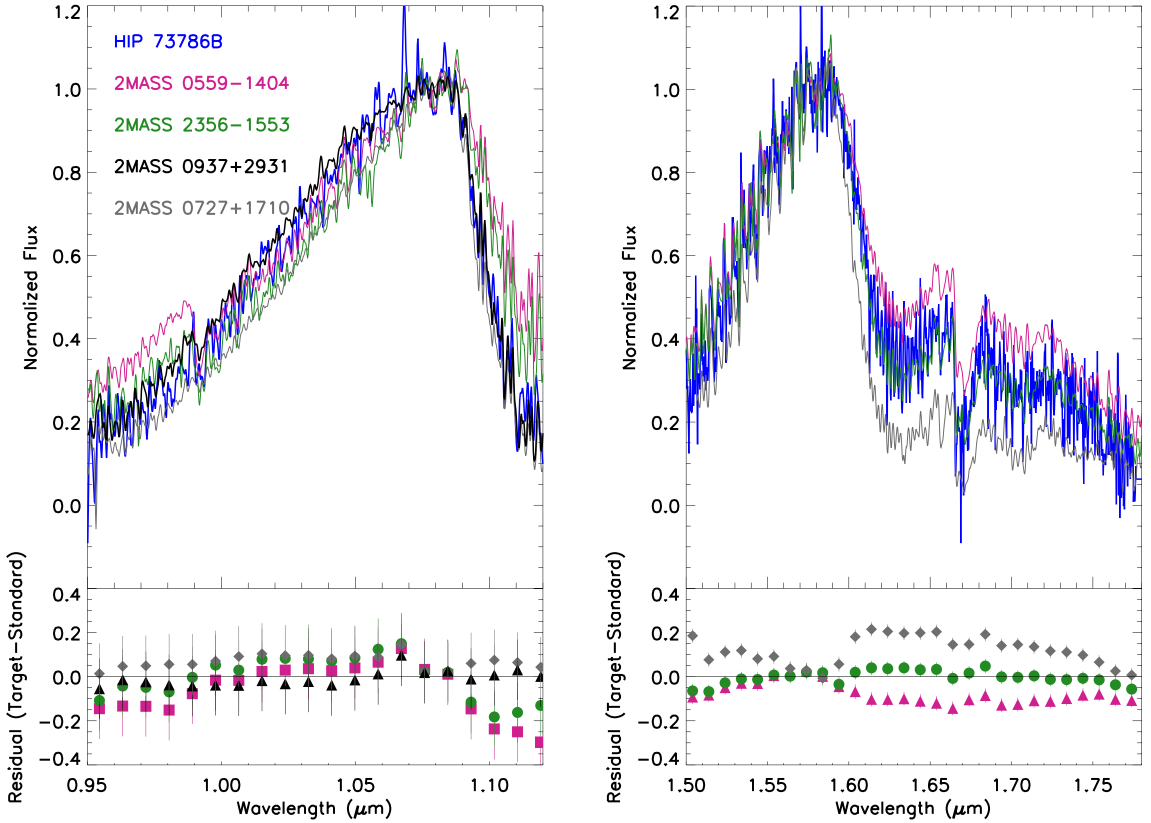

Figure 5.7 Comparison of the Y- (left) and H-band (right) spectra of HIP 73786B (T6p) in blue to BDSS T4.5-T7 brown dwarfs with Y- and H-band spectra including: 2MASS J05591914-1404488 (T4.5; Burgasser et al. 2000, 2006b, the T5.5 dwarf 2MASSI J2356547-155310 (2MASS J2356-1553; Burgasser et al. 2002, 2006b, the sub-solar metallicity T6 dwarf, 2MASS J0937+2931 (Burgasser et al., 2002, 2006b), and the T7 spectral standard, 2MASSI J0727182+171001 (T7; Burgasser et al. 2002, 2006b). 2MASS J0937+2931 is the best-match for HIP 73786B in the Y band, further supporting the Burningham et al. (2014) suggestion that HIP 73786B is metal poor and/or has a high gravity. The BDSS library does not include an H-band spectrum of 2MASS 0937+2931, but the H band is well-matched by 2MASS J2356-1553, a typical field dwarf of a similar spectral type to HIP 73786B. The agreement between 2MASS J2356-1553 and HIP 73786B in the H band implies that this object, while likely metal-poor and high gravity, has less extreme parameters than Wolf 1130C.

comparatively "normal" H band suggests that HIP 73786B is not as extreme as Wolf 1130C and may explain why HIP 73786B does not have an unusually red $J-H$ color for its spectral type.

CFBDS J030135.11-161418.0:

Albert et al. (2011) present an H-band spectrum of CFBDS J0301-1614 and use H-band spectral indices from Burgasser et al. (2000) to classify this object as a T7 dwarf. Comparing CFBDS J0301-1614's red $J-K_s$ and $H-K_s$ colors to BT-Settl models, Albert et al. 2011 suggest that CFBDS J0301-1614 may be low-gravity and/or high-metallicity. In Figure 5.8, I compare CFBDS J0301-1614 to the T7 and T8 spectral standards. I find that CFBDS J0301-1614 is underluminous in the blue-wing of the Y band when compared to both spectral standards, consistent with the low-gravity/high-metallicity hypothesis of Albert et al. (2011). In the H band, the target is slightly better matched by the T8 standard than the T7 standard, which is potential further evidence of low-gravity/high-metallicity as high-gravity/low-metallicity enhances the H band as seen in Wolf 1130C. Like the other three targets in this section, CFBDS J0301-1614's best-fit model results in both Y and truncated H band stand out from the bulk of the sample, though the model results vary. In most cases, the target is best fit by a $\log g < 5$. CFBDS J0301-1614 is classified as blue based on the M13b scheme and does indeed show spectral signatures of youth. Additional spectral coverage in J band, to confirm its H-band determined spectral type, and K band, to further test for the impact of low-gravity/high-metallicity, would be valuable for further investigation into this peculiar object.

ULAS J095047.28+011734.3:

Like Wolf 1130C, ULAS J0950+0117 (T8p) was identified as a wide-separation, binary companion to a low-metallicity, M dwarf primary (LHS 6176, [Fe/H] = -0.3 ± 0.1 dex; Luhman et al. 2012; Burningham et al. 2013). We find that the H-band NIRSPEC spectrum of ULAS J0950+0117 is well-fit by the T8 spectral standard, but that the blue wing of the Y band is marginally enhanced relative to the spectral standard (see Figure 5.10), consistent with low-metallicity/high-gravity. Mace et al. (2013a) present a Magellan/FIRE spectrum of ULAS J0950+0117 and also find that the Y band is slightly enhanced. They also detect

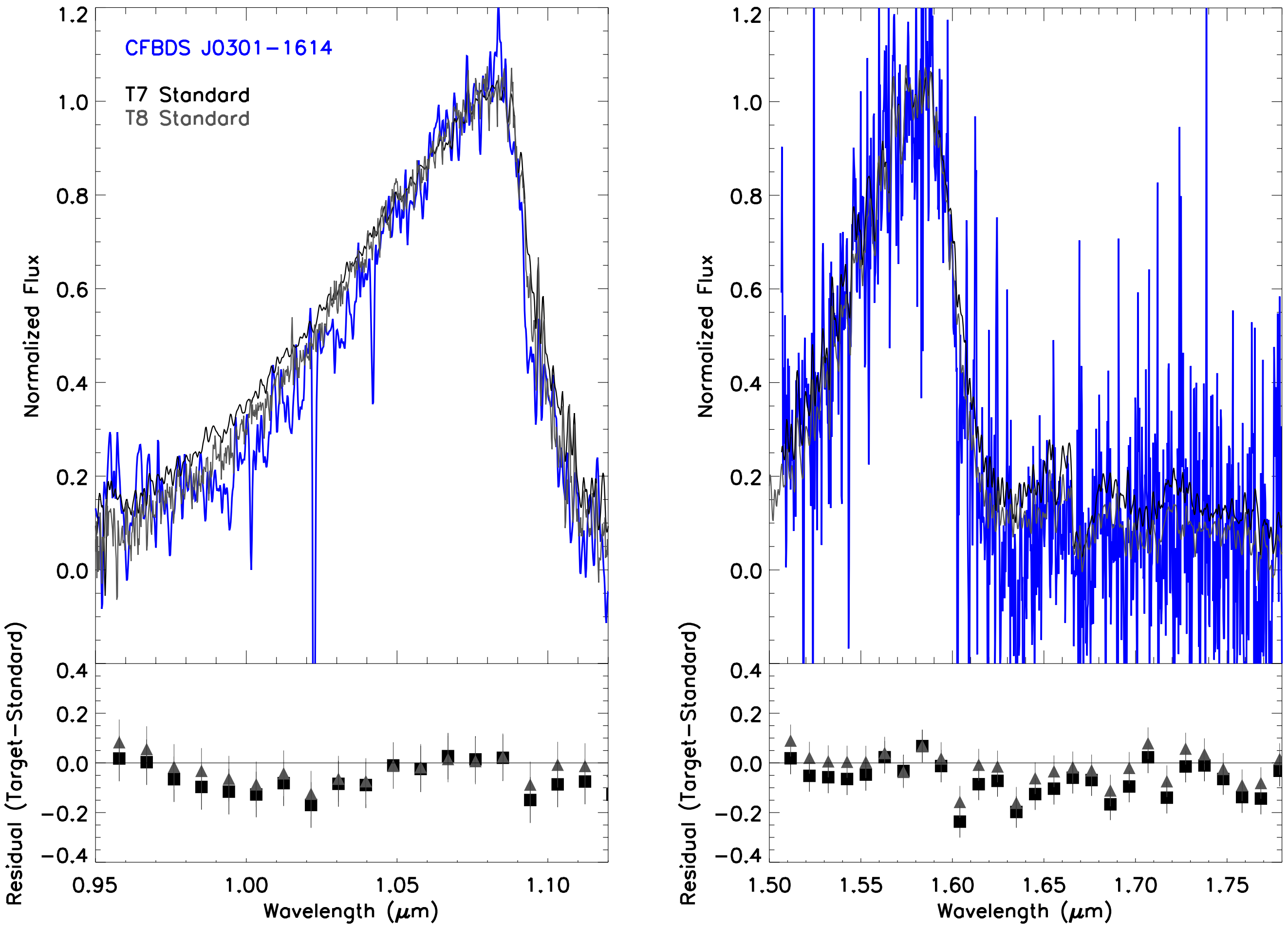

Figure 5.8 CFBDS J0301-1614 (T7; Albert et al. 2011) compared to the T7 (black) and T8 (grey) spectral standards. CFBDS J0301-1614 is plotted in blue to reflect its blue $J-H$ color. Target-Standard residuals for the T7 standard are plotted in black squares and the Target-Standard residuals for the T8 standard are plotted in grey triangles. In the Y band (left), CFBDS J0301-1614 is underluminous in the blue-wing when compared to both spectral standards. In the H band (right), the target is slightly better matched by the T8 standard. Both the Y- and H-band results are suggestive of high-metallicity/low-gravity..

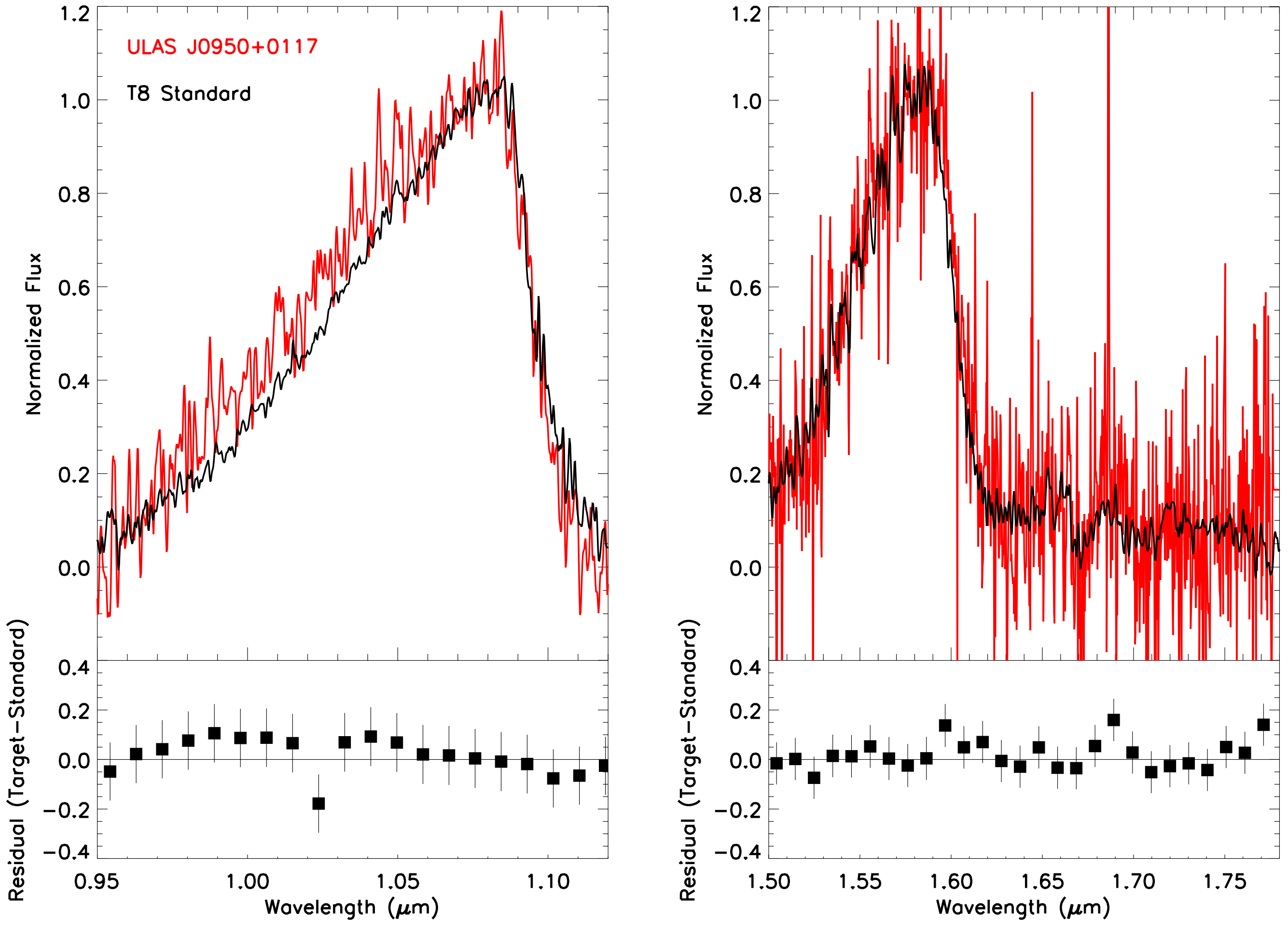

Figure 5.9 ULAS J0950+0117 (T8; Luhman et al. 2012; Burningham et al. 2013) compared to the T8 spectral standard (black). Target-Standard residuals are plotted in black squares. In the Y band, ULAS J0950+0117 is overluminous in the blue-wing when compared to the standard, though the H band is well-matched by the T8 standard.

a slightly enhanced H band and suppressed K band, though they do not classify the object as peculiar due to low signal-to-noise. Our NIRSPEC Y-band spectrum is poorly fit by the atmospheric models, though the truncated H-band model fits are consistent with the other T8/T8.5 brown dwarfs in this sample. The lack of peculiarity in the H band is unexpected given the unusually red $J - H$ color presented in Mace et al. (2013a). However, ULAS J0950+0117 has another H-band photometric measurement from Burningham et al. (2013) that implies a normal $J - H$ color (see Section 5.5 and Table 5.5). Further photometric follow-up to resolve the discrepant photometry is recommended.

WISE J161441.46+173935.5:
WISE J1614+1739 was identified as part of the follow-up of WISE color-selected brown dwarf candidates (T9; Kirkpatrick et al. 2011). WISE J1614+1739 is not a known companion and Gelino et al. (2011) found no evidence of a close-in, substellar companion to this object. Liu et al. (2013) note that the Y-band photometry of this object is unusual and they exclude it from their analysis. Leggett et al. (2013) remark that WISE 1614+1739 stands out as red in $J - H$ color space and suggests that more photometric follow-up is required to ensure that the red color is physical, not instrumental. This is the first work to report a Y-band spectrum of this object. In spite of the large error bars on the residual plot due to the extremely faint nature (J ∼19, see Table 5.5) of this target, we find that WISE J1614+1739 stands out as overluminous in the blue-wing of the Y band when compared to the T9 spectral standard, suggesting that it may be low-metallicity/high-gravity. Like ULAS J0950+0117, WISE J1614+1739 has discrepant H-band photometry in the literature. Both H-band photometric and spectroscopic follow-up on this object would confirm whether this object has an enhanced Y-band and normal H-band like HIP 73786B or an both an enhanced Y- and H-band like Wolf 1130C.

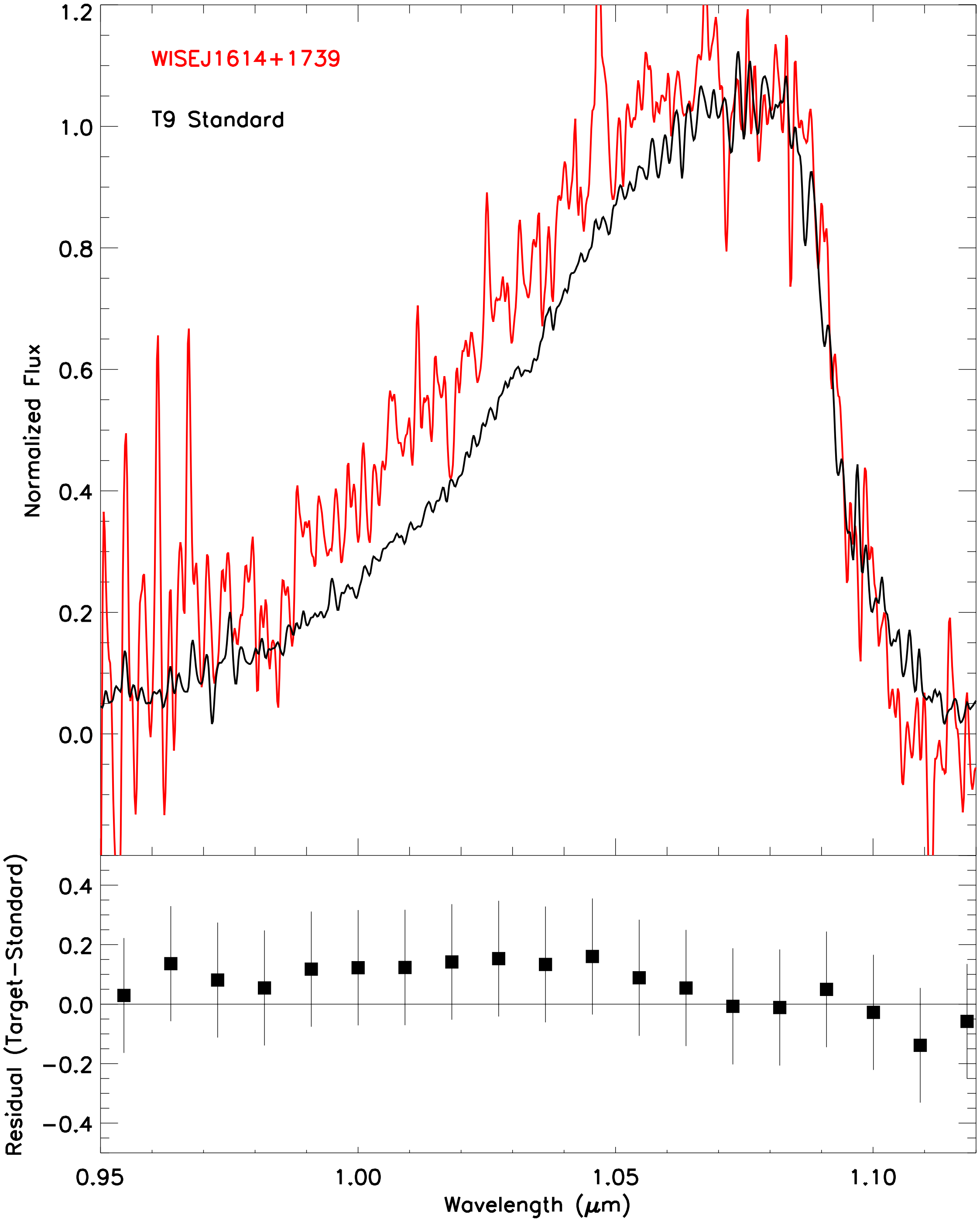

Figure 5.10 WISE J1614+1739 (T9; Kirkpatrick et al. 2011) compared to the T9 spectral standard (black). Target-Standard residuals are plotted in black squares. We find that the Y-band spectrum is overluminous in the blue-wing when compared to the standard.

5.4.4 Characteristics of Other Objects in the Sample

For interested readers, this section outlines the known spectral properties of targets in the sample that do not deviate from their spectral standard. Targets are organized by spectral type. Individual standard comparison plots for the objects discussed here are available in Section 5.8.

CFBDS J092250+152741:

CFBDS J0922+1524 was first discovered by Reyle et al. (2010). They present an H-band spectrum of CFBDS J0922+1524 and type it as a T7 dwarf based on the H-band spectral indices from Burgasser et al. (2006b). I present the first Y-band spectrum of this object. I also find that this blue object is well-matched by the spectral standard in both the Y and H bands.

ULAS J013939.77+004813.8:

ULAS J0139+0048 (T7.5) was discovered by Chiu et al. (2008). Chiu et al. (2008) present two sets of NIR photometry that classify the $J - H$ color of this object as red and blue respectively (see Section 5.5 for a discussion of the photometry of the sample). Comparing ULAS 0139+0048's $H_{MKO} - \mathit{ch2}$ to evolutionary models based on Marley et al. (2002) and Saumon & Marley (2008), Leggett et al. (2010) estimate a T$_{eff} \approx 850K$, $\log g \approx 5$ dex, and [m/H] ≈ 0 dex. I also do not find this object to be peculiar: both the T7 and T8 standards match the Y-band spectrum reasonably well, with the H band marginally better fit by the T7 standard.

WISE J075946.98-490454.0:

WISE J0759-4904 was identified as part of the WISE team follow-up of brown dwarf candidates (T8; Kirkpatrick et al. 2011). I present the first Y-band spectrum of this object. I find that this red object's Y-band spectrum is well-matched by the T8 spectral standard.

ULAS J101721.40+011817.9:

Discovered by Burningham et al. (2008), ULAS J1017+0118 is classified as T8p due to a reported dearth of methane absorption in its H band spectrum. Burningham et al. (2008) compare the spectrum to solar-metallicity BT-Settl model spectra and estimate its T$_{eff}$ to be between 750-850 K, and $\log g$ between 5-5.5 dex. In contrast, Leggett et al. (2010a) compare NIR and Spitzer photometry of ULAS J1017+0118 to evolutionary models and suggest that the target may be low gravity ($\log g$ = 4-4.5 dex) or high metallicity. Based on the M13b color criteria, ULAS J1017+0118 is classified as blue/young. The gravity results from this work's truncated H-band model fits are highly model dependent and range from $\log g = 3.5$ dex (BT-Settl) to $\log g = 5.5$ dex (Saumon). However, I find that the H-band spectrum of ULAS J1017+0118 is reasonably well-matched to the T7 and T8 standard.

WISE J161705.74+180714.1:

WISE J1617+1807 (T8) was identified by Burgasser et al. (2011) as a potentially cloudy, cool ($T_{eff} = 600 \pm 30$ K), low-gravity ($\log g = 4.0 \pm 0.3$ dex) T dwarf by comparison of a near-infrared spectrum from Magellan/FIRE (Simcoe et al., 2010) to the Saumon & Marley (2008) atmospheric models. The blue $J - H$ color of this object supports the Burgasser et al. (2011) result. However, I find that the target is well matched by its spectral standard in both NIRSPEC Y and H bands. In general, the model fits to this object are in good agreement with the other T8/T8.5 targets in the sample, with the exception of the Morley fit in the Y-band fixed $\log g$ case, as discussed in Section 5.4.2.2.

WISE J054047.00+483232.4:

WISE J0540+4832 is a T8.5 dwarf discovered by Mace et al. (2013a). I present the first Y- and H-band spectra of this object. I find that this red object's spectrum is intermediate between the T8 and T9 standard in both the Y and H bands, as supported by its spectral type.

WISEJ181210.85+272144.3:

Like WISE J1617+1804, WISE J1812+2722 (T8.5:) was identified by Burgasser et al. (2011) as a cool ($T_{eff} = 620 \pm 30$ K), low-gravity ($\log g = 4.3 \pm 0.3$ dex), late-type T dwarf. Except for the Burrows fit, which prefers a $\log g = 5.5$ dex, the Y-band model results are also consistent with low-gravity. The H-band gravity fits are consistent with the other T8/T8.5 dwarfs in the sample. Compared to NIRSPEC BDSS spectral standards, the Y band is perhaps slightly narrower than the T9 standard, but not significantly. The H band is better fit by the T9 standard in the flux peak, but is equally well-fit by the T8 and T9 standards in the methane band.

ULAS J214638.83-001038.7 (Wolf 940 B):

Discovered by Burningham et al. (2009), Wolf 940 B (T8.5) is the companion of an M4 dwarf. Burningham et al. (2009) derive a metallicity of [Fe/H]=-0.06 ± 0.20 dex for the system. Leggett et al. (2010a) present low-resolution Spitzer mid-infrared spectrum of Wolf 940B from 7.5-14.2 μm and include a detailed analysis of the metallicity of Wolf 940 B, concluding that the metallicity of Wolf 940B is within $\sim$0.2 dex of solar. The blue $J-H$ color of this object supports the Leggett et al. (2010a) result. Both the Y- and H-band spectra of Wolf 940B are well fit by the T9 standard.

WISE J000517.48+373720.5:

WISE J0005+3737 was identified as part of the WISE team follow-up of brown dwarf candidates (T9; Kirkpatrick et al. 2012). Leggett et al. (2015) present new near-infrared photometry from Gemini/NIRI that is discrepant with the WISE team photometry presented in Mace et al. (2013a) (see Section 5.5). I present the first Y- and H-band spectra of this object. I find that the T9 standard is an exceedingly good match to the H-band spectrum of WISE J0005+3737. The Y-band spectrum is marginally under-luminous compared to the T9 standard in the $\sim$1.05-1.10 μm region, but the rest of the Y-band spectrum is an excellent match to the standard. There is no clear sign of peculiarity in this object.

5.5 Discussion

In Section 5.4 I show that comparing the target spectra to atmospheric models by holding T$_{eff}$ or $\log g$ fixed reveals similarities and differences among the four atmospheric model grids used in this analysis, but does not reveal any general physical trends in the sample that correlate with $J-H$ color. Comparing each individual target in the sample to spectral standards from the BDSS further supports the overall homogeneity of the sample, though there are a few objects that stand out as unusual. In this section, I discuss the observational and physical mechanisms that could be driving the $J-H$ colors of the sample.

5.5.1 Discrepant Photometry in the Literature

Leggett et al. (2015) report the MKO photometry of 18 known late-T and Y dwarfs. Fourteen of these objects already have MKO or MKO-like photometry presented by the WISE team (Beichman et al., 2013, 2014; Kirkpatrick et al., 2012, 2013; Mace et al., 2013a). Of the 14 objects that overlap in the WISE team and Leggett et al. samples, five objects have discrepant (>2 sigma) J and/or H band magnitudes. Two of these objects are in the sample of color outliers: WISE J0005+3737 and WISE J1614+1739. Both objects are classified by WISE team photometry as unusually red, and would not qualify as color outliers based on the Leggett et al. (2015) photometry (see Table 5.5).

Leggett et al. (2015) argue that atmospheric variability in the 14 overlapping T and Y dwarfs is likely too small to account for the discrepancies in the near-infrared photometry, which can differ by up to a magnitude between datasets. A large near-infrared study of late-T/Y dwarf variability is still needed to statistically characterize the impact of variability on the near-infrared photometry of these late-type objects (see also Littlefair et al. 2017). However, detections of near-infrared variability from a handful of mid- to late-T dwarfs with typical peak-to-peak amplitudes $< 10\%$ (e.g. Buenzli et al. 2012, 2014; Radigan et al. 2012, 2014; Wilson et al. 2014; Rajan et al. 2015) support this claim. Peak-to-peak variability amplitudes of $<10\%$ have also been detected for T and Y dwarfs using mid-infrared data from Spitzer (Metchev et al. 2015; Cushing et al. 2016; Leggett et al. 2016). Leggett et al. (2015) instead suggest that the discrepant near-IR photometry of these objects may be due to previously "unrecognized differences in photometric systems" between the instruments at the Gemini Observatories used in Leggett et al. and the various instruments used by the WISE team.

To further investigate whether instrumental differences could lead to the discrepant photometry in this sample, I took a closer look at the available filter transmission curves for the instruments used by both the WISE team and Leggett et al. (2015). WISE J0005+3737 was observed by the WISE team using the OSIRIS instrument (Depoy et al., 1993) on the South-

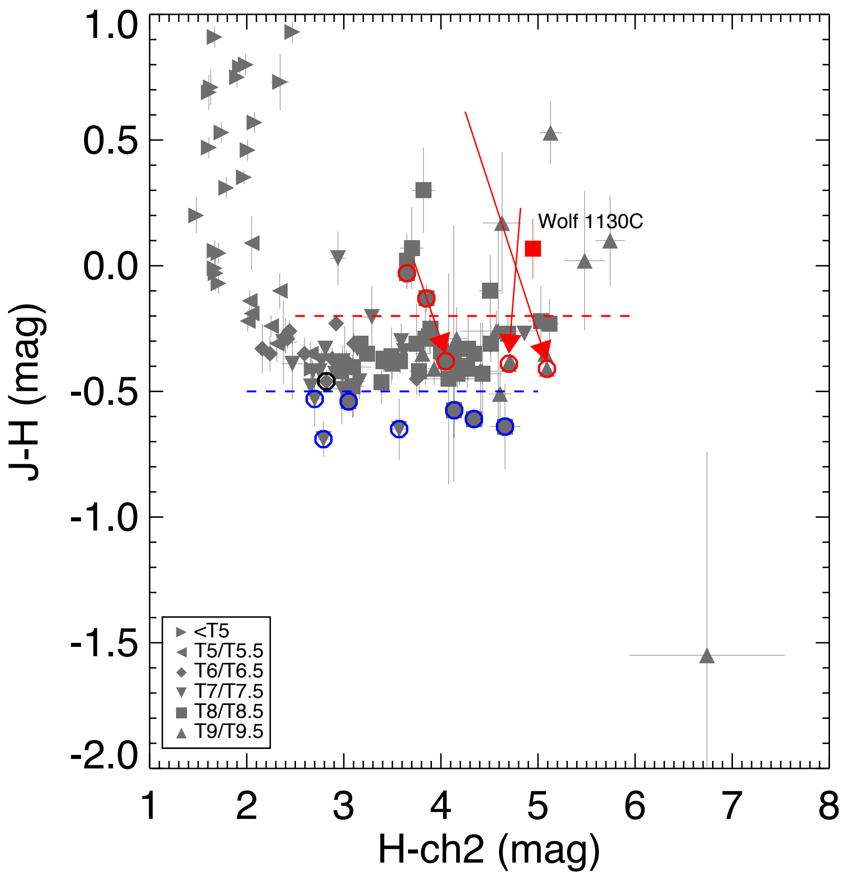

Figure 5.11 Same as Figure 5.1, but with updated photometry for three of the four targets with discrepant photometry (> 2 sigma) in the literature. The red arrows denote the movement of these three objects in color space, with the head of the arrow indicating photometry from Leggett et al. (2015) or Burningham et al. (2013) and the tail of the arrow indicating photometry from Kirkpatrick et al. (2011) or Mace et al. (2013a). The photometry from Kirkpatrick et al. (2011) or Mace et al. (2013a) were used to select the $J-H$ outliers for this sample. All three objects are re-classified from “red” to “normal” based on the Leggett et al. or Burningham et al. photometry. Of these three targets, two have NIRSPEC spectra with enhanced Y-band flux in comparison to their spectral standard.

Table 5.5. Near-Infrared MKO Photometry from the Literature

Short Name	SpT	J (mag)	J err (mag)	H (mag)	H err (mag)	$J-H$ (mag)	$J-H$ err	M13b classification	Instrument	Reference[a]
WISE J0005+3737	T9	18.3	0.12	18.1	0.08	0.23	0.144	red	OSIRIS (SOAR)	M13a
		17.59	0.02	17.98	0.02	-0.39	0.03	normal	NIRI	L15
ULAS J0139+0048	T7.5	18.43	0.04	19.12	0.05	-0.69	0.071	blue	UFTI/IRIS2	C08
		18.69	0.09	18.61	0.17	0.08	0.19	red	WFCAM (UKIDSS)	C08
CFBDS J0301-1614	T7p	18.34	0.07	18.99	0.10	-0.65	0.12	blue	WIRcam	A11
WISE J0540+4832	T8.5	18.49	0.02	18.62	0.05	-0.13	0.054	red	WIRC	M13a
WISE J0759-4904	T8	17.38	0.05	17.41	0.04	-0.03	0.064	red	PANIC	M13a
CFBDS J0922+1527	T7	18.28	0.04	18.81	0.10	-0.53	0.11	blue	WIRcam	A11
ULAS J0950+0118	T8p	18.09	0.07	18.07	0.08	-0.02	0.106	red	WIRC	M13a
		18.05	0.04	18.24	0.15	-0.19	0.16	normal	WFCAM (UKIDSS)	M13a
		18.02	0.03	18.4	0.03	-0.38	0.04	normal	WFCAM	B13
ULAS J1017+0118	T8p	18.53	0.02	19.07	0.02	-0.54	0.03	blue	UFTI	B08
HIP 73786B	T6p	16.59	0.02	17.05	0.04	-0.46	0.40	normal	WFCAM (UKIDSS)	Mu11
WISE J1614+1739	T9	19.084	0.059	18.471	0.216	0.613	0.224	red	SpartanIRC (SOAR)	K11
		18.9	0.02	19.31	0.04	-0.41	0.04	normal	NIRI	L15
WISE J1617+1807	T8	17.659	0.08	18.234	0.078	-0.57	0.112	blue	SpartanIRC (SOAR)	K11
WISE J1812+2721	T8.5	18.19	0.06	18.83	0.16	-0.64	0.171	blue	WIRC	K11; Burg11
Wolf 1130C	T8p	19.64	0.089	19.572	0.079	0.068	0.119	red	WIRC	M13b
Wolf 940B	T8.5	18.16	0.02	18.77	0.03	-0.61	0.04	blue	UFTI	B09

[a] References- M13a (Mace et al., 2013a); L15 (Leggett et al., 2015); C08 (Chiu et al., 2008); A11 (Albert et al., 2011); B13 (Burningham et al., 2013); B08 (Burningham et al., 2008); Mu11 (Murray et al., 2011); K11 (Kirkpatrick et al., 2011); Burg11 (Burgasser et al., 2011); M13b (Mace et al., 2013b); B09 (Burningham et al., 2009)

ern Astrophysical Research (SOAR) Telescope[9]. While the OSIRIS H-band filter curve is very similar to the MKO H-band curve, the OSIRIS J-band wavelength coverage is broader than the MKO J bandpass as defined in Simons & Tokunaga (2002). Mace et al. (2013a) list their OSIRIS photometry under the MKO heading in their Table 4, but the authors do note that the OSIRIS data is not on the MKO system. Thus I adopt the Leggett et al. (2015) MKO measurement for WISE 0005+3737. With this new photometry, WISE J0005+3737 is no longer classified as a color-outiler based on the M13b criteria. This is further supported by its normal Y and H band spectra as presented in this chapter.

WISE J1614+1739 was observed by the WISE team using the Spartan Infrared Camera (SpartanIRC; Loh et al. 2012) on the SOAR Telescope and by Leggett et al. (2015) using Gemini/NIRI. Like the Gemini/NIRI filters, the SpartanIRC/SOAR were designed as MKO filters, and the bandwidths of both the SpartanIRC and NIRI filter sets as listed on each instrument's website are nearly identical (see Table 5 in Loh et al. 2012 or the SpartanIRC website at Michigan State University[10] for more information on the SpartanIRC filters). However, both the J- and H-band photometry differ by $\geq 3\sigma$ between the two instruments ($\Delta J = 0.18 \pm 0.06$ mag; $\Delta H = 0.84 \pm 0.22$ mag). Either WISE J1614+1739 is variable, or there are other systematics in the data. Based on the SpartanIRC photometry, WISE J1614 is classified as "red," but it is classified as "normal" using the NIRI photometry. Unlike WISE J0005+3737, WISE J1614+1739 does show enhanced Y-band flux and further follow-up to resolve the photometric discrepancy would be valuable.

The sample also includes two targets, not included in Leggett et al. 2015, that have discrepant MKO photometry in the literature: ULAS J0950+0117 and ULAS J0139+0048. As discussed in M13b, there are three sets of J- and H-band photometry for ULAS J0950+0117 in the literature. Mace et al. (2013a) present Palomar/WIRC (Wilson et al., 2003) photometry and also report photometry from the UKIDSS archive (Lawrence et al., 2007). UKIDSS data were observed using the Wide Field CAMera (WFCAM) on UKIRT (Casali et al., 2007).

---

[9] SOAR/OSIRIS filter curves can be found at `http://www.ctio.noao.edu/instruments/ir_instruments/osiris2soar/config/index.html`

[10] `http://www.pa.msu.edu/~loh/SpartanIRCamera/`

Burningham et al. (2013) presented further UKIRT/WFCAM near-infrared photometry, as part of their follow-up of UKIDSS brown dwarf candidates. The J-band photometry for all three data sets are consistent within 1σ, but the H-band photometry ranges from H_{WIRC} = 18.07 ± 0.08 (Mace et al. 2013a) to H_{WFCAM} = 18.40 ± 0.03 mag (Burningham et al. 2013). Based on the WIRC data, ULAS J0950+0048 is classified as "red." Based on both sets of WFCAM data (from the UKIDSS database and as presented in Burningham et al. 2013), ULAS J0950+0117 is classified as "normal." The WIRC[11] and WFCAM[12] filter sets were both developed to MKO specifications and the filter curves are nearly identical. Given the unusual nature of ULAS J0950+0117 and the range of H-band photometry, further photometric follow-up on this object is recommended.

Chiu et al. (2008) reported two sets of MKO J- and H-band measurements for ULAS J0139+0048. The first set of J- and H-band measurements came from the UKIDSS database and the second were observed with the UKIRT Fast-Track Imager[13] (UFTI; Roche et al. 2003). Both the J- and H-band UFTI photometry disagree at $\geq 2\sigma$ with the UKIDSS photometry. The UKIDSS photometry yields a "red" color designation, while the UFTI photometry yields a "blue" designation. While Chiu et al. (2008) note the inconsistent photometry, they do not suggest a cause for the discrepancy. A visual inspection of the UKIDSS data does not reveal any artifacts in the field. I have adopted the UFTI data in this analysis as it has smaller uncertainties. This maintains a "blue" color designation for ULAS J0139+0048.

Of the four brown dwarfs in the sample with discrepant photometry in the literature, one object (WISE J0005+3737) does indeed appear to be discrepant due to significant differences in the filter transmission curves of the two instruments used to observe the target. This lends further support to the Leggett et al. (2015) assertion that instrumental differences can impact the photometry of these late-type T dwarfs and emphasizes the need for consistent photometry of the late-type T dwarf population on a well-calibrated instrument. However,

---

[11] `http://www.astro.caltech.edu/palomar/observer/200inchResources/wircspecs.html#filters`

[12] `http://www.ukirt.hawaii.edu/instruments/wfcam/user_guide/description.html`

[13] `http://www.ukirt.hawaii.edu/instruments/ufti/PARAMETERS.html#2`

the three remaining targets with discrepant photometry were observed with bona-fide MKO filters and the differences in filter transmission between the instruments used is negligible. While it is possible that there are other instrumental systematics impacting the results, the unusual spectral morphologies of two of the three remaining dwarfs with discrepant photometry suggests that there may also be physical motivation for the photometric differences. Photometric monitoring of late-T dwarfs at YJH bands may serve to separate the impact of atmospherically variability (e.g. clouds) from from morphological changes due to extreme physical parameters (e.g. [Fe/H], $\log g$).

5.5.2 Atmospheric Variability: Clouds and Temperature Variations

Adopting updated photometry for three of the four objects with discrepant photometry in the literature, moves all three of those objects into "normal" $J-H$ color space (see Figure 5.11). Excluding those three objects, however, leaves ten objects that are classified as outliers based on the M13b color criteria, nine of which exhibit Y- and H-band spectral morphologies that closely match their respective spectral standards. If we assume robust photometry for these objects, the question then becomes, is it possible to induce an unusual $J-H$ color for these objects while simultaneously maintaining a uniform normalized flux shape?

Morley et al. (2012) examine the impact of sulfide clouds on late-type T dwarfs. Analysis of the MKO photometry derived from the Morley et al. (2012) models[14] shows that, for a fixed T_{eff}, $\log g$, and metallicity, $J-H$ colors move red-ward with decreasing f_{sed} (increasing clouds). In peak-normalized Y- and H-band spectra, this translates to a broadening of the wings of each band, while the peaks remain relatively unchanged (see Figure 5.12), but the impact is small. Clouds *do* alter the relative strengths of the $YJHK$ bands at these late-T dwarf temperatures, however (see, e.g. Figure 5 in Morley et al. (2012)). Thus, a relative change between the strength of the bands would be detectable in flux-calibrated spectra, but we would not see such a change in this peak-normalized sample.

In Morley et al. (2014), the authors further examine the impact of patchy clouds and

---

[14] see `http://www.ucolick.org/~cmorley/cmorley/Models.html`

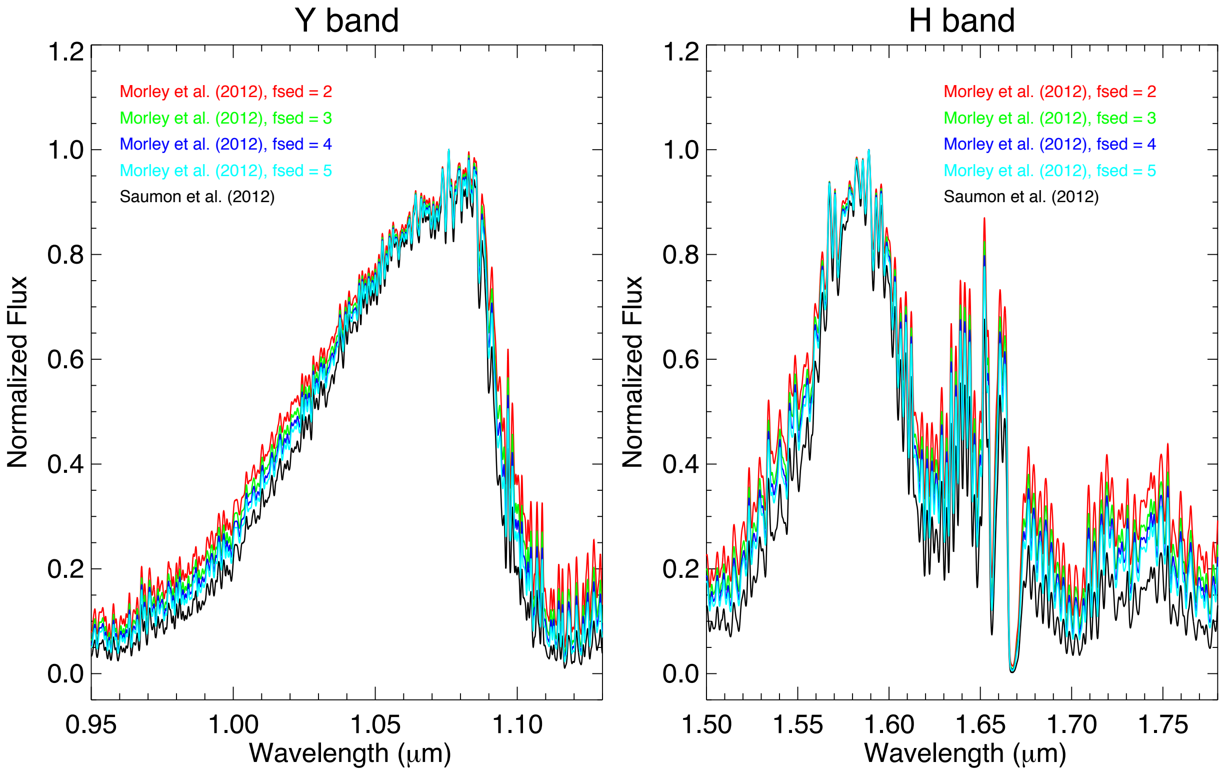

Figure 5.12 Peak-normalized Y- (left) and H -band (right) Morley et al. (2012) atmospheric model spectra at $\mathrm{T}_{eff} = 700$ K, $\log g = 4.5$ dex, solar metallicity, and varying f_{sed}. Saumon et al. (2012) cloudless models are also plotted for comparison. Holding everything else fixed, varying the sedimentation efficiency from $f_{sed} = 5$ (i.e. thin clouds) to $f_{sed} = 2$ (i.e. thick clouds), serves to broaden the wings of both the Y- and H-band spectra, but does not impact the shape or breadth of the flux peak itself.

hot spots on the atmospheres of T and Y dwarfs. They find that increased cloud cover again drives the $J - H$ color of late-T dwarfs red-ward for effective temperatures > 300 K, without significantly changing the mid-infrared colors or the peak morphology of the individual bands in the 1-2.5 μm spectrum (see their Figures 1 and 2). Thin global clouds or minimal patchy clouds in these late-T dwarf spectra lead to bluer colors than thick global clouds or significant patchy cloud cover. Clouds can account for a spread in $J - H$ color consistent with the observational spread we see for all but a few of the reddest $J - H$ outliers in this sample, including Wolf 1130C. If clouds are prevalent in late-T dwarf atmospheres, then clouds make $J - H$ color an inconsistent selector for metallicity/gravity variation. However, it should be noted that Line et al. (2015, 2016) do not generally find evidence for thick clouds in their atmospheric retrieval model fits to a sample of 11 late-T dwarfs.

Temperature fluctuations have also been proposed as a source of variability in brown dwarf atmospheres (e.g. Showman & Kaspi 2013; Robinson & Marley 2014). Morley et al. (2014) investigate the impact of hot spots in a cloud-free atmospheric model and find that adding energy at different levels in the atmosphere (i.e. different pressures) does indeed impact $J - H$ color (see their Figure 5). However, like the patchy cloud models, the hot spot models do not account for the reddest $J - H$ outliers in this sample. Spectroscopically, the Morley et al. (2014) hot spot models show the largest deviation in atmospheric absorption regions and are more prominent in the mid-infrared where cloud-induced variability is notably smaller. Thus we would not expect to see the impact of hot spots in ground-based, near-infrared spectra.

While the Morley et al. (2014) patchy cloud and hot spot models show that variability can drive scatter in $J - H$ color, an object like Wolf 1130C, which shows broad deviation from the spectral standard in the near-infrared, cannot be explained by variability alone, making it an unambiguous outlier in metallicity/gravity. Thus, while variability may explain some of the measured spread in $J - H$ color, variability alone is not able to account for the near-infrared photometry of the late-T dwarf population.

5.5.3 Gravity, Metallicity, Clouds, and Brown Dwarf Radii: A Complex Parameter Space

Atmospheric composition can have a significant impact on the radius of a brown dwarf. Burrows et al. (2011) generated three atmospheric models (cloudy with [Fe/H] = 0.0 dex, cloudy with [Fe/H] = 0.5 dex, cloud-free with [Fe/H] = 0.0 dex) to study the interplay between mass, radius, metallicity, clouds, and gravity. They find that, for a given mass, high metallicity and/or thick clouds, which increase atmospheric opacity, result in a larger radius (up to ∼10% - 25%) than a lower metallicity/cloud-free atmosphere. A cloud-induced spread in radii at a given mass and age, also implies a spread in gravity for that mass and age. The impact on the emerging spectral morphology from differences in radii are thus complex and parameter independent. As discussed in 5.5.2, Morley et al. (2012) show that sulfide clouds redden the near-infrared spectrum of late-T dwarfs at a fixed $\log g$. Increasing $\log g$ strengthens the CIA of H_2 which serves to make the near-infrared spectrum bluer (Saumon et al., 2012). However, the precise interplay between clouds, gravity, and metallicity can be much more complicated, emphasizing the challenge of fully-characterizing the atmospheres of late-type T dwarfs, particularly solitary T dwarfs in the field.

5.5.4 Looking Forward

Wolf 1130C illustrates the value of Y band spectroscopy for probing extreme metallicity and gravity in the late-T dwarf population. However, the overall homogeneity of the $J - H$ outliers studied here suggests that typical metallicity/gravity variation in the field T dwarf population is likely small. To isolate the impact of metallicity/gravity on near-infrared, late-T dwarf spectra from the impact of spectral variability, high signal-to-noise (S/N) spectra and models that are better calibrated at high- and low-metallicity will be required. K-band spectroscopy is also a valuable probe of extreme gravity/metallicity (e.g. Burgasser et al. 2006a; Saumon et al. 2012), but the faint nature of the K band implies that high S/N, medium-resolution, K-band spectra of late-T dwarfs will be easier to obtain with the next generation thirty-meter class telescopes or JWST.

Is $J - H$ color a good predictor of age for of late-type T dwarfs? The results from this study are inconclusive. Models indicate that $J - H$ color could be sensitive to atmospheric variability (Morley et al., 2012, 2014). Observational variability studies indicate that the impact of variability on near-infrared photometry is typically $<$ 10% outside of the L/T transition (e.g. Radigan et al. 2014). However, most variability studies to date have focused on L/T transition objects and included only a few mid-to-late T dwarfs, and a dedicated late-T and Y dwarf multi-wavelength variability study is needed. However, the intrinsically faint nature of these objects and the photometric errors associated with ground based photometry make ground-based variability studies challenging (e.g. Koen 2013). Moreover, inconsistent photometry of late-type T dwarfs in the literature can be larger than the expected change in magnitude from physical variability, emphasizing the need for consistent photometry to accurately make a definitive statement on the value of $J - H$ color as a probe of metallicity, gravity, clouds, and/or non-equilibrium chemistry.

5.6 Summary

In this chapter, I tested the hypothesis set forth in Mace et al. (2013b) that T dwarfs with unusual $J - H$ colors may show evidence of extreme age compared to the typical field population. To do so, I used Keck/NIRSPEC Y- and H-band spectroscopy to look for spectroscopic tracers of age such as non-solar metallicity or extreme gravity by comparison to spectral standards and four publicly-available atmospheric model grids. The overall sample is surprisingly homogeneous, though four objects stand out as metallicity/gravity outliers, two of which (HIP 73786B and ULAS J0950+0117) are previously known companions to stars with measured metallicity. Of the other two, CFBDS J0301-1614 has been previously identified as unusual, but the final object, WISE J1614+1739, has little information in the literature and is identified as unusual for the first time in this work. The new Y-band spectrum of WISE J1614+1739 presented here suggests that this object may be low-metallicity/high-gravity. Further follow-up of all four targets would be valuable as we begin to statistically probe tthe extremes of gravity and metallicity in the late-T dwarf population.

Model comparisons illustrated that the current, publicly-available atmospheric models are fairly heterogeneous in the 1.05 μm region of the Y band and in the 1.65 μm CH_4 absorption. Updated models with increased metallicity range and improved molecular line lists– particularly of CH_4– and updated treatment of alkali line broadening, will ultimately be required to map the full parameter space probed by the late-T dwarf population. Also, discrepant photometry in the literature emphasized the need for a near-infrared photometric survey carried out on a single, well-characterized instrument. Multi-wavelength, time series photometry to test for variability will also help quantify the impact of clouds on these late-type objects.

5.7 Acknowledgements

In addition to the acknowledgements listed in the front of this manuscript, I would like to thank Chris Gelino for a valuable discussion on photometry and Mike Cushing for a thoughtful discussion of SpeX and NIRSPEC spectral reduction. I would also like to thank the developers of the REDSPEC package, Sung-Soo Kim, Lisa Prato, and Ian McLean.

5.8 Chapter 5 Appendix

Here I present the Y- and H- band spectra of the targets described in Section 5.4.4 that do not show spectral signatures of extreme gravity and/or metallicity. Each target is compared to the spectral standard of that type or of the two nearest spectral standards if the target has a half spectral type classification. The spectra are organized by spectral type and colored by $J-H$ color as described in Section 5.3. Target-Standard residual plots are also provided, with the residual plots binned to R$\sim$200 for clarity.

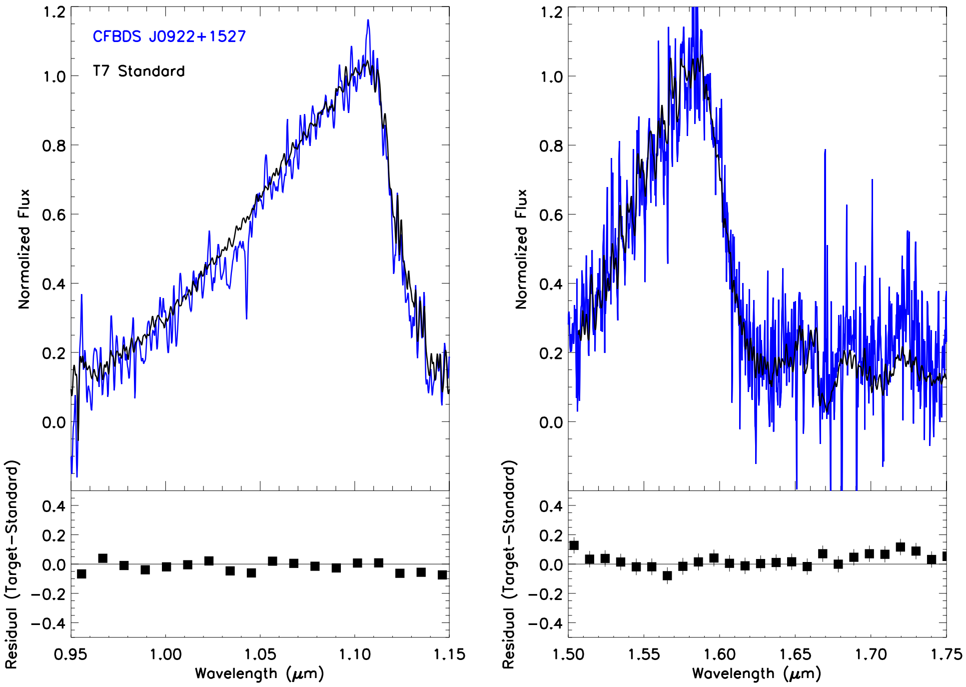

Figure 5.13 CFBDS J0922+1527 (T7)

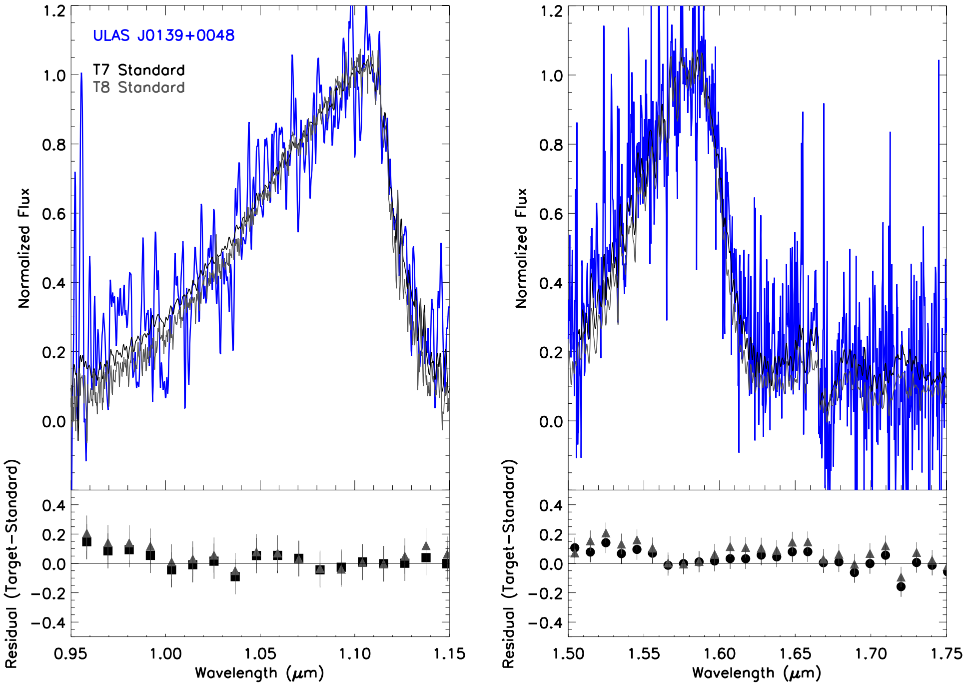

Figure 5.14 ULAS J0139+0048 (T7.5)

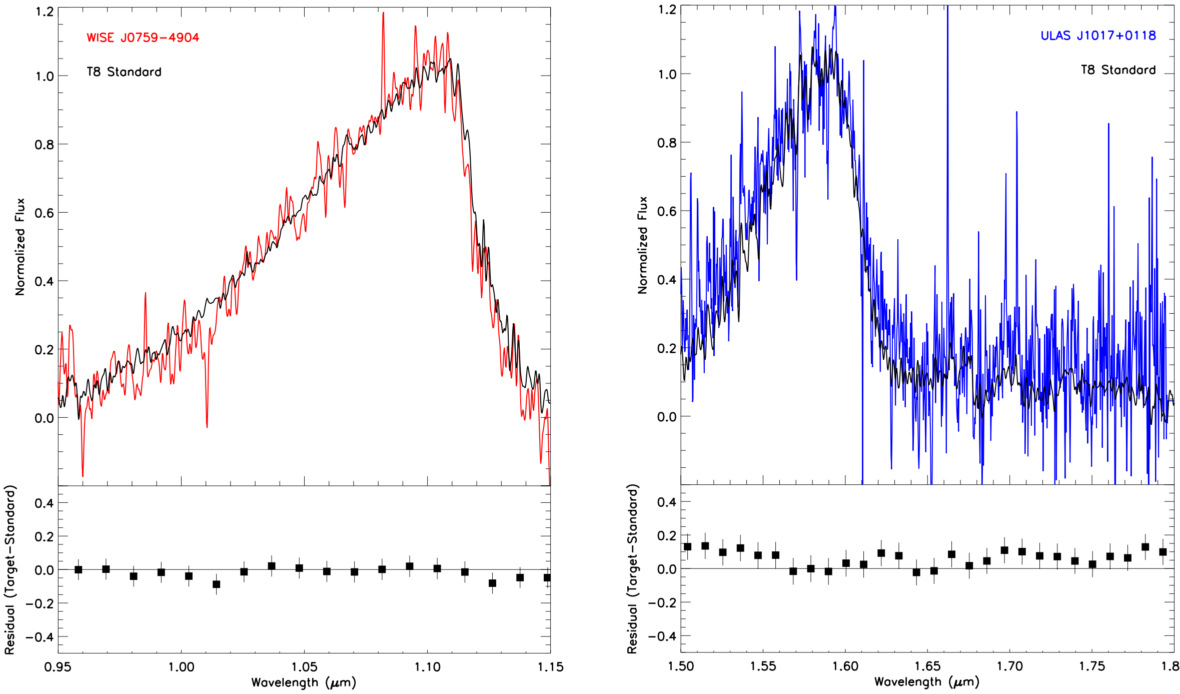

Figure 5.15 Y band spectrum of WISE J0759-4904 (T8; left) and H band spectrum of ULAS J1017+0118 (T8p).

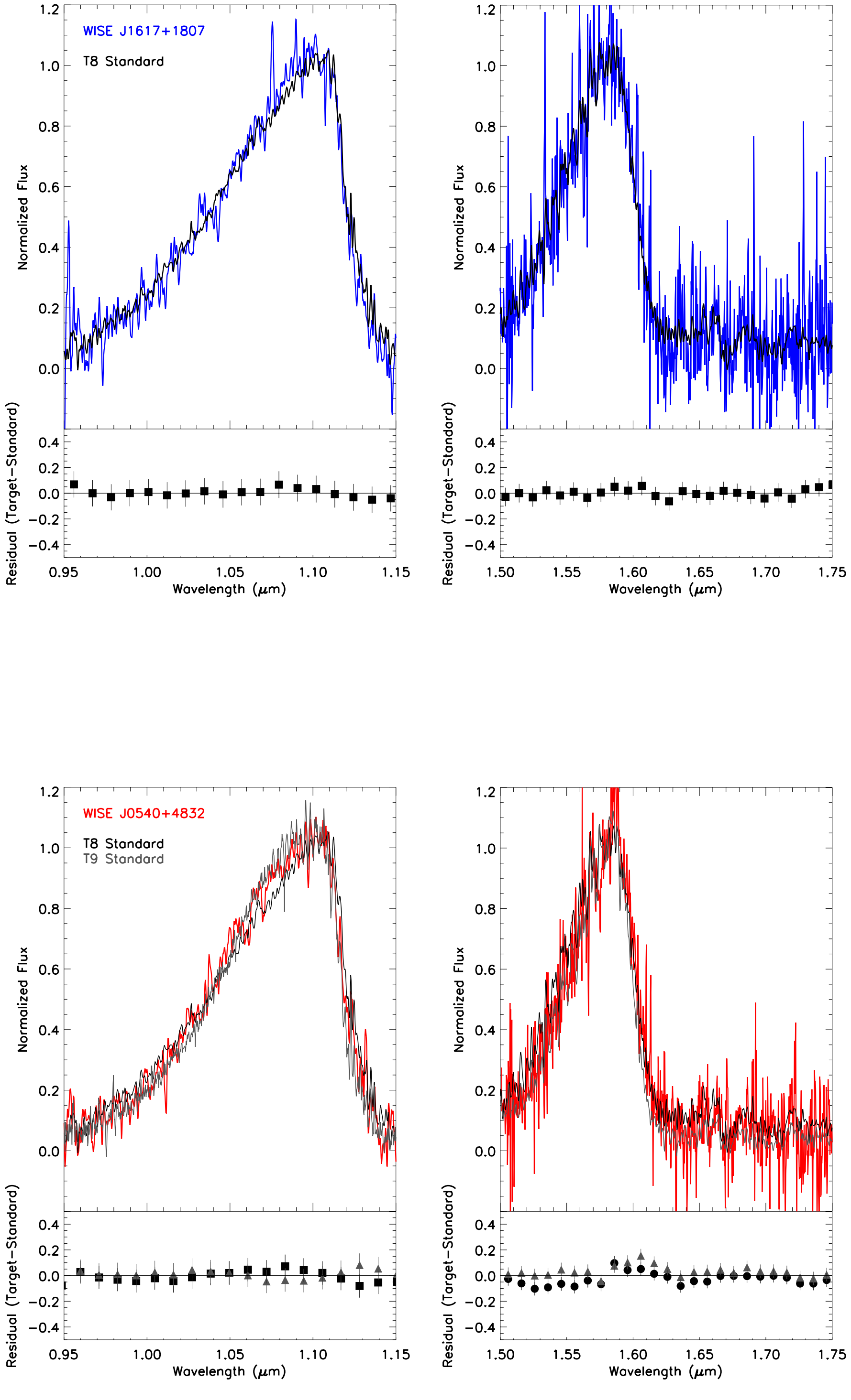

Figure 5.16 WISE J1617+1807 (T8; top) and WISE J0540+4832 (T8.5)

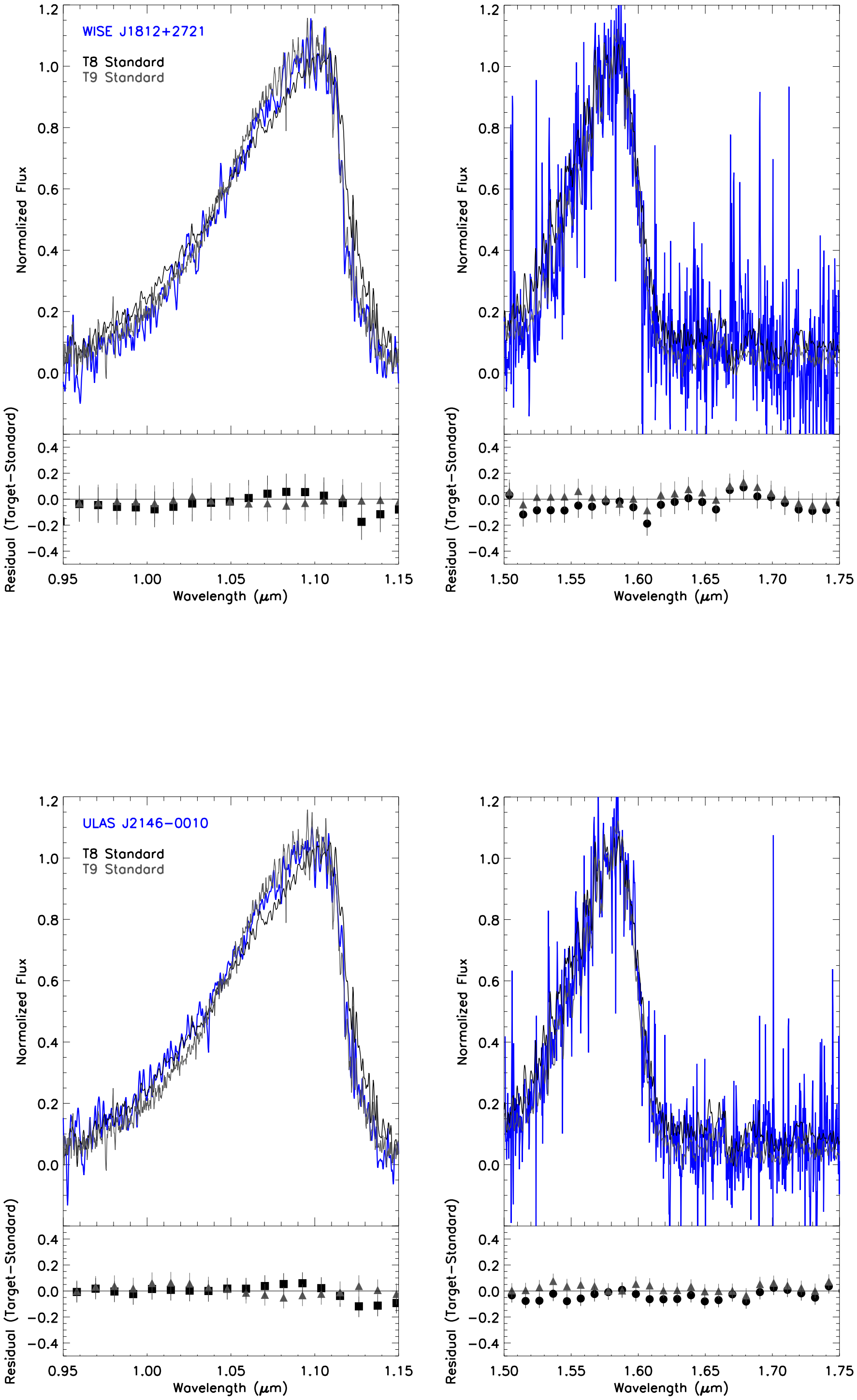

Figure 5.17 WISE J1812+2721 (T8.5; top) and ULAS 2146-0010 (Wolf 940B; T8.5)

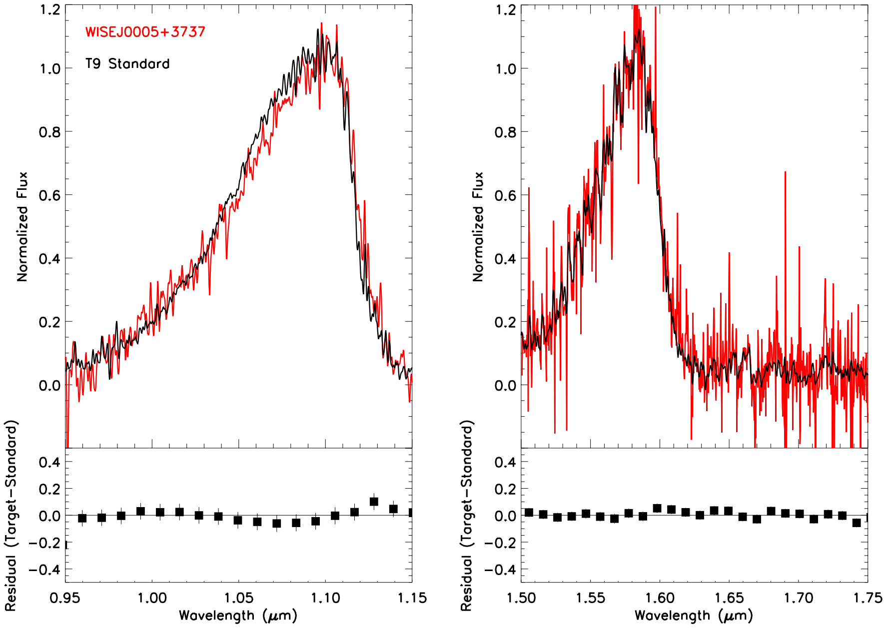

Figure 5.18 WISE J0005+3737 (T9)

CHAPTER 6

Conclusions and Future Work

Two of my goals for graduate school were to pursue a path of astronomical inquiry to address questions of star formation, especially for the coldest known products of star formation, and to become skilled in the development and leadership of astronomical instrumentation. This thesis describes both the development and application of infrared instruments, and reports original observations using FLITECAM on SOFIA and NIRSPEC on Keck. I played a leadership role in the in-lab development and on-sky commissioning of FLITECAM in both the FLIPO and solo configurations as the UCLA Instrument Scientist. Chapter 2 described my FLITECAM research and development work in the UCLA Infrared Lab. This lab work included the successful elimination of two light leaks in the FLITECAM filter wheel module and the discovery and mitigation of thermoacoustic oscillations in the FLITECAM liquid helium vent assembly. I also measured the resolution of FLITECAM's low-resolution slit and determined FLITECAM's filter wheel move logic. Finally, I supported FLITECAM's first deployment to New Zealand for the Pluto Occultation and FLITECAM's successful acceptance as a Facility Class Science Instrument on SOFIA, which included developing new documentation on instrument operation and assembly.

Chapter 3 of this work described FLITECAM commissioning and early science on SOFIA in the FLIPO configuration, a co-mounting of FLITECAM with the optical instrument, HIPO. FLIPO commissioning was completed over six flights in February 2014, during which time FLITECAM's imaging and spectroscopic modes from $\sim$1-4 μmwere characterized. Increased thermal backgrounds due to warm fore-optics precluded the commissioning of FLITECAM's longest wavelength modes in this configuration. FLIPO early science included spectroscopy of the Type IA supernova, SN 2014J, an exoplanet transit observation, and imaging of the star-forming region, NGC 2024. All three science cases included observations at wavelengths that are either difficult or impossible to observe from the ground, highlighting critical wavelength regimes where FLITECAM can add to the scientific discussion on a myriad of astrophysical questions. This chapter also describes FLIPO's first deployment to New Zealand to observe a Pluto occultation nearly contemporaneously with the New Horizons fly-by of Pluto. This observation fully realizes the power of the SOFIA platform. SOFIA's mobility allowed central flash observations of Pluto. The use of both FLIPO and the FPI+ allowed photometric coverage of the occultation with four optical to near-infrared passbands, which allowed us to test for the presence of haze in Pluto's atmosphere.

Chapter 4 of this work described FLITECAM commissioning and science in the solo configuration. With both FLIPO and solo commissioning in hand, we were able to directly compare FLITECAM's imaging and grism performance. The additional fore optics in the FLIPO mode lead to increased backgrounds when compared to the solo configuration, particularly in FLITECAM's long wavelength imaging modes (> 2 μm) and longest wavelength grism mode, which is unobservable in the FLIPO configuration. The solo configuration extends FLITECAM's full frame imaging capabilities out to 4.6 μm and its grism spectroscopy capabilities out to 5.5 μm. FLITECAM solo mode science cases included medium and narrow-band imaging of the NGC 2024 and W3 star-forming regions, and spectroscopy of NGC 7027. The early results of the star-forming research are promising and highlight FLITECAM's ability to probe the complex interaction between the newly-formed stars and the gas and dust in these regions. A detailed analysis of these two regions, with new data from FLITECAM's Fall 2016 solo flights, will be continued as I transition into the next stage of my career.

Chapters 3 and 4 also discussed the excess background emission at low elevations that was discovered during early FLITECAM commissioning. This emission is from the outboard engine on the telescope side of the aircraft, which is then reflected off both the primary mirror itself and the aft spider supporting the secondary mirror. The spider reflections are the dominant contributor to the excess background at all but the lowest elevations. A baffle installation in 2016 mitigated spider reflections, but a secondary reflection was discovered.

In Chapter 5, I presented the results of a Keck/NIRSPEC spectroscopic follow-up survey of thirteen late-type T dwarfs (T6-T9) with unusually red or blue $J-H$ colors. This research was carried out in parallel with the FLITECAM instrument development and commissioning work. Mace et al. (2013b) suggests that $J-H$ color outliers may represent the high-gravity, low-metallicity (old) and low-gravity, solar-metallicity (young) extremes of the late-type T dwarf population. To test this hypothesis, I used medium resolution Y- and H-band spectroscopy to probe regions of T dwarf atmospheres that are more sensitive to gravity and metallicity variations than the J band. I found that the spectral morphologies of the sample are largely homogeneous, though three objects stand out as potentially old and a fourth object stands out as potentially young. Of these four objects, three have been previously identified as unusual. To characterize the physical properties of the sample, I compared the target spectra to both spectral standards and publicly available atmospheric model grids. The best-fit parameters derived from model comparisons vary depending on the atmospheric model grid used, underlining the difficulty of modeling the coldest products of the star formation process. Updated models will be required to more fully characterize the properties of the late-T dwarf population. Discrepant photometry in the literature emphasized the need for a near-infrared photometric survey carried out on a single, well-characterized instrument in order to separate the impact of physical differences in $J-H$ color (e.g. atmospheric variability) from instrument-dependent differences. The results of Chapter 5 will be submitted for publication in the Astrophysical Journal.

Bibliography

Albert, L., Artigau, É., Delorme, P., et al. 2011, AJ, 141, 203

Allard, F., Homeier, D., & Freytag, B. 2011, in Astronomical Society of the Pacific Conference Series, Vol. 448, 16th Cambridge Workshop on Cool Stars, Stellar Systems, and the Sun, ed. C. Johns-Krull, M. K. Browning, & A. A. West, 91

Allard, F., Homeier, D., Freytag, B., & Sharp, C. M. 2012, in EAS Publications Series, Vol. 57, EAS Publications Series, ed. C. Reylé, C. Charbonnel, & M. Schultheis, 3–43

Allers, K. N., & Liu, M. C. 2013, ApJ, 772, 79

Angerhausen, D., Huber, K. F., Mandell, A. M., et al. 2014, in IAU Symposium, Vol. 293, Formation, Detection, and Characterization of Extrasolar Habitable Planets, ed. N. Haghighipour, 435–441

Angerhausen, D., Mandushev, G., Mandell, A., et al. 2015, Journal of Astronomical Telescopes, Instruments, and Systems, 1, 034002

Baker, J. G., & Menzel, D. H. 1938, ApJ, 88, 52

Becklin, E. E., Tielens, A. G. G. M., & Callis, H. H. S. 2006, Modern Physics Letters A, 21, 2551

Beckwith, S. V. W. 2013, The visible and near-infrared domain, ed. M. C. E. Huber, A. Pauluhn, J. L. Culhane, J. G. Timothy, K. Wilhelm, & A. Zehnder (New York, NY: Springer New York), 121–137

Beichman, C., Gelino, C. R., Kirkpatrick, J. D., et al. 2013, ApJ, 764, 101

—. 2014, ApJ, 783, 68

Bik, A., Lenorzer, A., Kaper, L., et al. 2003, in IAU Symposium, Vol. 212, A Massive Star Odyssey: From Main Sequence to Supernova, ed. K. van der Hucht, A. Herrero, & C. Esteban, 541

Bregman, J. D., Dinerstein, H. L., Goebel, J. H., et al. 1983, ApJ, 274, 666

Brown, A. G. A., de Geus, E. J., & de Zeeuw, P. T. 1994, A&A, 289, 101

Buenzli, E., Apai, D., Radigan, J., Reid, I. N., & Flateau, D. 2014, ApJ, 782, 77

Buenzli, E., Apai, D., Morley, C. V., et al. 2012, ApJ, 760, L31

Burgasser, A. J., Burrows, A., & Kirkpatrick, J. D. 2006a, ApJ, 639, 1095

Burgasser, A. J., Geballe, T. R., Leggett, S. K., Kirkpatrick, J. D., & Golimowski, D. A. 2006b, ApJ, 637, 1067

Burgasser, A. J., Wilson, J. C., Kirkpatrick, J. D., et al. 2000, AJ, 120, 1100

Burgasser, A. J., Kirkpatrick, J. D., Brown, M. E., et al. 2002, ApJ, 564, 421

Burgasser, A. J., Kirkpatrick, J. D., Burrows, A., et al. 2003, ApJ, 592, 1186

Burgasser, A. J., Simcoe, R. A., Bochanski, J. J., et al. 2010, ApJ, 725, 1405

Burgasser, A. J., Cushing, M. C., Kirkpatrick, J. D., et al. 2011, ApJ, 735, 116

Burningham, B., Smith, L., Cardoso, C. V., et al. 2014, MNRAS, 440, 359

Burningham, B., Pinfield, D. J., Leggett, S. K., et al. 2008, MNRAS, 391, 320

—. 2009, MNRAS, 395, 1237

Burningham, B., Pinfield, D. J., Lucas, P. W., et al. 2010, MNRAS, 406, 1885

Burningham, B., Lucas, P. W., Leggett, S. K., et al. 2011, MNRAS, 414, L90

Burningham, B., Cardoso, C. V., Smith, L., et al. 2013, MNRAS, 433, 457

Burrows, A., Burgasser, A. J., Kirkpatrick, J. D., et al. 2002, ApJ, 573, 394

Burrows, A., Heng, K., & Nampaisarn, T. 2011, ApJ, 736, 47

Burrows, A., Sudarsky, D., & Hubeny, I. 2006, ApJ, 640, 1063

Casali, M., Adamson, A., Alves de Oliveira, C., et al. 2007, A&A, 467, 777

Cenarro, A. J., Peletier, R. F., Sánchez-Blázquez, P., et al. 2007, MNRAS, 374, 664

Chabrier, G., Johansen, A., Janson, M., & Rafikov, R. 2014, Protostars and Planets VI, 619

Chiu, K., Liu, M. C., Jiang, L., et al. 2008, MNRAS, 385, L53

Cohen, M., Wheaton, W. A., & Megeath, S. T. 2003, AJ, 126, 1090

Colditz, S., Klein, R., Beckmann, S., et al. 2014, Boresight calibration of FIFI-LS: in theory, in the lab and on sky, doi:10.1117/12.2055335

Crepp, J. R., Johnson, J. A., Fischer, D. A., et al. 2012, ApJ, 751, 97

Cushing, M. C., Vacca, W. D., & Rayner, J. T. 2004, PASP, 116, 362

Cushing, M. C., Kirkpatrick, J. D., Gelino, C. R., et al. 2011, ApJ, 743, 50

Cushing, M. C., Hardegree-Ullman, K. K., Trucks, J. L., et al. 2016, ApJ, 823, 152

Dahn, C. C., Harris, H. C., Vrba, F. J., et al. 2002, AJ, 124, 1170

Depoy, D. L., Atwood, B., Byard, P. L., Frogel, J., & O'Brien, T. P. 1993, in Proc. SPIE, Vol. 1946, Infrared Detectors and Instrumentation, ed. A. M. Fowler, 667–672

Dinger, A. S., Dunham, E. W., Erickson, E. F., et al. 1992, Evaluation of Jet-Exhaust Emission Scattering for the Aft Telescope Configuration on SOFIA, Ames Research Center NASA Technical Memo 110828

Draine, B. T. 2003, ARA&A, 41, 241

Dunham, E. W., Bida, T. A., Collins, P. L., et al. 2014, in Proc. SPIE, Vol. 9147, Ground-based and Airborne Instrumentation for Astronomy V, 91470H

Dunham, E. W., Elliot, J. L., Bida, T. A., & Taylor, B. W. 2004, in Society of Photo-Optical Instrumentation Engineers (SPIE) Conference Series, Vol. 5492, Society of Photo-Optical

Instrumentation Engineers (SPIE) Conference Series, ed. A. F. M. Moorwood & M. Iye, 592–603

Dunham, E. W., Bida, T. A., Collins, P. L., et al. 2012, in Proc. SPIE, Vol. 8446, Ground-based and Airborne Instrumentation for Astronomy IV, 844618

Dupuy, T. J., & Liu, M. C. 2012, ApJS, 201, 19

Dupuy, T. J., Liu, M. C., & Ireland, M. J. 2009, ApJ, 699, 168

Eberspeaker, P. J., & Pierce, D. L. 2011, in ESA Special Publication, Vol. 700, 20th Symposium on European Rocket and Balloon Programmes and Related Research, ed. L. Ouwehand, 47–54

Faherty, J. K., Burgasser, A. J., Cruz, K. L., et al. 2009, AJ, 137, 1

Filippazzo, J. C., Rice, E. L., Faherty, J., et al. 2015, The Astrophysical Journal, 810, 158

Gelino, C. R., Kirkpatrick, J. D., Cushing, M. C., et al. 2011, AJ, 142, 57

Gray, R. O., Corbally, C. J., Garrison, R. F., McFadden, M. T., & Robinson, P. E. 2003, The Astronomical Journal, 126, 2048

Haisch, Jr., K. E., Lada, E. A., & Lada, C. J. 2000, AJ, 120, 1396

Hayashi, C., & Nakano, T. 1963, Progress of Theoretical Physics, 30, 460

He, L., Whittet, D. C. B., Kilkenny, D., & Spencer Jones, J. H. 1995, ApJS, 101, 335

Hummer, D. G., & Storey, P. J. 1987, MNRAS, 224, 801

Kirkpatrick, J. D. 2005, ARA&A, 43, 195

Kirkpatrick, J. D., Cushing, M. C., Gelino, C. R., et al. 2013, ApJ, 776, 128

—. 2011, ApJS, 197, 19

Kirkpatrick, J. D., Gelino, C. R., Cushing, M. C., et al. 2012, ApJ, 753, 156

Kirkpatrick, J. D., Schneider, A., Fajardo-Acosta, S., et al. 2014, ApJ, 783, 122

Kirkpatrick, J. D., Kellogg, K., Schneider, A. C., et al. 2016, ApJS, 224, 36

Koen, C. 2013, Monthly Notices of the Royal Astronomical Society, 428, 2824

Kuiper, G. P. 1939, ApJ, 89, 548

Kumar, S. S. 1963, ApJ, 137, 1121

Lawrence, A., Warren, S. J., Almaini, O., et al. 2007, MNRAS, 379, 1599

Leggett, S. K., Morley, C. V., Marley, M. S., & Saumon, D. 2015, The Astrophysical Journal, 799, 37

Leggett, S. K., Morley, C. V., Marley, M. S., et al. 2013, ApJ, 763, 130

Leggett, S. K., Saumon, D., Burningham, B., et al. 2010a, ApJ, 720, 252

Leggett, S. K., Burningham, B., Saumon, D., et al. 2010b, ApJ, 710, 1627

Leggett, S. K., Saumon, D., Marley, M. S., et al. 2012, ApJ, 748, 74

Leggett, S. K., Cushing, M. C., Hardegree-Ullman, K. K., et al. 2016, ApJ, 830, 141

Line, M. R., Marley, M. S., Liu, M. C., et al. 2016, ArXiv e-prints, arXiv:1612.02809

Line, M. R., Teske, J., Burningham, B., Fortney, J. J., & Marley, M. S. 2015, ApJ, 807, 183

Littlefair, S. P., Burningham, B., & Helling, C. 2017, MNRAS, 466, 4250

Liu, M. C., Dupuy, T. J., & Ireland, M. J. 2008, ApJ, 689, 436

Liu, M. C., Magnier, E. A., Deacon, N. R., et al. 2013, The Astrophysical Journal Letters, 777, L20

Logsdon, S. E., McLean, I. S., Becklin, E. E., et al. 2016, in Proc. SPIE, Vol. 9908, Ground-based and Airborne Instrumentation for Astronomy VI, 99080B

Logsdon, S. E., McLean, I. S., Becklin, E. E., et al. 2014, in Proc. SPIE, Vol. 9147, Ground-based and Airborne Instrumentation for Astronomy V, 91472Y

Loh, E. D., Biel, J. D., Davis, M. W., et al. 2012, PASP, 124, 343

Lord, S. D. 1992, A new software tool for computing Earth's atmospheric transmission of near- and far-infrared radiation, Tech. rep.

Lucas, P. W., Tinney, C. G., Burningham, B., et al. 2010, MNRAS, 408, L56

Luhman, K. L., Loutrel, N. P., McCurdy, N. S., et al. 2012, ApJ, 760, 152

Mace, G. N. 2014, PhD thesis, University of California, Los Angeles

Mace, G. N., Kirkpatrick, J. D., Cushing, M. C., et al. 2013a, ApJS, 205, 6

—. 2013b, ApJ, 777, 36

Mainzer, A., Cushing, M. C., Skrutskie, M., et al. 2011, ApJ, 726, 30

Mainzer, A. K. 2003, PhD thesis, University of California, Los Angeles

Mainzer, A. K., & McLean, I. S. 2003, ApJ, 597, 555

Mainzer, A. K., McLean, I. S., Sievers, J. L., & Young, E. T. 2004, ApJ, 604, 832

Mainzer, A. K., McLean, I. S., Aliado, T., et al. 2003, in Proc. SPIE, Vol. 4857, Airborne Telescope Systems II, ed. R. K. Melugin & H.-P. Roeser, 21–28

Marley, M. S., & Robinson, T. D. 2015, ARA&A, 53, 279

Marley, M. S., Saumon, D., & Goldblatt, C. 2010, ApJ, 723, L117

Marley, M. S., Seager, S., Saumon, D., et al. 2002, The Astrophysical Journal, 568, 335

Martin, E. C., Mace, G. N., McLean, I. S., et al. 2017, The Astrophysical Journal, 838, 73

McGovern, M. R. 2005, PhD thesis, University of California, Los Angeles, California, USA

McGovern, M. R., Kirkpatrick, J. D., McLean, I. S., et al. 2004, ApJ, 600, 1020

McLean, I. S. 2008, Electronic Imaging in Astronomy: Detectors and Instrumentation (Second Edition) (Praxis Publishing)

McLean, I. S., McGovern, M. R., Burgasser, A. J., et al. 2003, ApJ, 596, 561

McLean, I. S., Smith, E. C., Becklin, E. E., et al. 2012, in Society of Photo-Optical Instrumentation Engineers (SPIE) Conference Series, Vol. 8446, Society of Photo-Optical Instrumentation Engineers (SPIE) Conference Series

McLean, I. S., Becklin, E. E., Bendiksen, O., et al. 1998, in Proc. SPIE, Vol. 3354, Infrared Astronomical Instrumentation, ed. A. M. Fowler, 566–578

McLean, I. S., Smith, E. C., Aliado, T., et al. 2006, in Society of Photo-Optical Instrumentation Engineers (SPIE) Conference Series, Vol. 6269, Society of Photo-Optical Instrumentation Engineers (SPIE) Conference Series

Metchev, S. A., Heinze, A., Apai, D., et al. 2015, ApJ, 799, 154

Morley, C. V., Fortney, J. J., Marley, M. S., et al. 2012, ApJ, 756, 172

Morley, C. V., Marley, M. S., Fortney, J. J., & Lupu, R. 2014, ApJ, 789, L14

Murray, D. N., Burningham, B., Jones, H. R. A., et al. 2011, MNRAS, 414, 575

Nakajima, T., Oppenheimer, B. R., Kulkarni, S. R., et al. 1995, Nature, 378, 463

Neugebauer, G., Habing, H. J., van Duinen, R., et al. 1984, ApJ, 278, L1

Olkin, C. B., Young, L. A., French, R. G., et al. 2014, Icarus, 239, 15

Pfüller, E., Wiedemann, M., Wolf, J., & Krabbe, A. 2016, in Proc. SPIE, Vol. 9908, Ground-based and Airborne Instrumentation for Astronomy VI, 99082W

Pilbratt, G. L., Riedinger, J. R., Passvogel, T., et al. 2010, A&A, 518, L1

Pinfield, D. J., Jones, H. R. A., Lucas, P. W., et al. 2006, MNRAS, 368, 1281

Pinfield, D. J., Burningham, B., Lodieu, N., et al. 2012, MNRAS, 422, 1922

Pinfield, D. J., Gromadzki, M., Leggett, S. K., et al. 2014, MNRAS, 444, 1931

Radigan, J., Jayawardhana, R., Lafrenière, D., et al. 2012, ApJ, 750, 105

Radigan, J., Lafrenière, D., Jayawardhana, R., & Artigau, E. 2014, ApJ, 793, 75

Rajan, A., Patience, J., Wilson, P. A., et al. 2015, MNRAS, 448, 3775

Rayner, J. T., Toomey, D. W., Onaka, P. M., et al. 2003, PASP, 115, 362

Reylé, C., Delorme, P., Willott, C. J., et al. 2010, A&A, 522, A112

Rice, E. L. 2009, PhD thesis, University of California, Los Angeles

Riess, A. G., Press, W. H., & Kirshner, R. P. 1996, The Astrophysical Journal, 473, 88

Robinson, T. D., & Marley, M. S. 2014, ApJ, 785, 158

Roche, P. F., Lucas, P. W., Mackay, C. D., et al. 2003, in Proc. SPIE, Vol. 4841, Instrument Design and Performance for Optical/Infrared Ground-based Telescopes, ed. M. Iye & A. F. M. Moorwood, 901–912

Russell, R. W., Soifer, B. T., & Willner, S. P. 1977, ApJ, 217, L149

Saumon, D., & Marley, M. S. 2008, The Astrophysical Journal, 689, 1327

Saumon, D., Marley, M. S., Abel, M., Frommhold, L., & Freedman, R. S. 2012, ApJ, 750, 74

Schmidt, S. J., Cruz, K. L., Bongiorno, B. J., Liebert, J., & Reid, I. N. 2007, AJ, 133, 2258

Scholz, R.-D. 2010, A&A, 515, A92

Showman, A. P., & Kaspi, Y. 2013, ApJ, 776, 85

Simcoe, R. A., Burgasser, A. J., Bochanski, J. J., et al. 2010, in Proc. SPIE, Vol. 7735, Ground-based and Airborne Instrumentation for Astronomy III, 773514

Simons, D. A., & Tokunaga, A. 2002, PASP, 114, 169

Skrutskie, M. F., Cutri, R. M., Stiening, R., et al. 2006, AJ, 131, 1163

Smith, E. C. 2008, PhD thesis, University of California, Los Angeles

Smith, E. C., & McLean, I. S. 2006, in Proc. SPIE, Vol. 6269, Society of Photo-Optical Instrumentation Engineers (SPIE) Conference Series, 62691I

Smith, E. C., & McLean, I. S. 2008, in Society of Photo-Optical Instrumentation Engineers (SPIE) Conference Series, Vol. 7014, Society of Photo-Optical Instrumentation Engineers (SPIE) Conference Series

Thompson, M. A., Kirkpatrick, J. D., Mace, G. N., et al. 2013, PASP, 125, 809

Vacca, W. D., Hamilton, R. T., Savage, M., et al. 2015, ApJ, 804, 66

van Leeuwen, F. 2007, A&A, 474, 653

Vrba, F. J., Henden, A. A., Luginbuhl, C. B., et al. 2004, AJ, 127, 2948

Waddell, P., Becklin, E. E., Hamilton, R. T., Vacca, W. D., & Lachenmann, M. 2016, in Proc. SPIE, Vol. 9973, Infrared Remote Sensing and Instrumentation XXIV, 99730O

Waddell, P., & Black, D. S. 2016, in Proc. SPIE, Vol. 9912, Advances in Optical and Mechanical Technologies for Telescopes and Instrumentation II, 99122T

Wang, Q. D., Dong, H., Cotera, A., et al. 2010, MNRAS, 402, 895

Werner, M. W., Roellig, T. L., Low, F. J., et al. 2004, ApJS, 154, 1

Wilson, J. C., Eikenberry, S. S., Henderson, C. P., et al. 2003, in Proc. SPIE, Vol. 4841, Instrument Design and Performance for Optical/Infrared Ground-based Telescopes, ed. M. Iye & A. F. M. Moorwood, 451–458

Wilson, P. A., Rajan, A., & Patience, J. 2014, A&A, 566, A111

Wolf, J., Wiedemann, M., Pfüller, E., et al. 2014, in Proc. SPIE, Vol. 9145, Ground-based and Airborne Telescopes V, 91450W

Wright, E. L., Eisenhardt, P. R. M., Mainzer, A. K., et al. 2010, AJ, 140, 1868

Xu, Y., Reid, M. J., Zheng, X. W., & Menten, K. M. 2006, Science, 311, 54

York, D. G., Adelman, J., Anderson, Jr., J. E., et al. 2000, AJ, 120, 1579

Young, E. T., Herter, T. L., Güsten, R., et al. 2012a, in Proc. SPIE, Vol. 8444, Ground-based and Airborne Telescopes IV, 844410

Young, E. T., Becklin, E. E., Marcum, P. M., et al. 2012b, ApJ, 749, L17

Zhang, Z. H., Homeier, D., Pinfield, D. J., et al. 2017, MNRAS, 468, 261